WASM: Minerals, Energy and Chemical Engineering

Multi-Scale Porosity and Pore Structure Assessment of Shale

Yujie Yuan

This thesis is presented for the Degree of

Doctor of Philosophy

of

Curtin University

January 2020

Declarations

To the best of my knowledge and belief this thesis contains no material previously published by any other person except where due acknowledgment has been made.

This thesis contains no material which has been accepted for the award of any other degree or diploma in any university.

Signature: Yujie Yuan

Date: 16 January 2020

Abstract

U.S. commercial success of unconventional shale gas production spurred the growing interest in shale investigations globally. Understanding the multi-scale pore size and structure in shale is the most fundamental. Recent development in advanced techniques provides numerous insightful pore structure interpretations. However, those interpretations which are acceptable for conventional sandstones or carbonates are not precisely transferable for shales. Different measurements exhibit large discrepancies and inconsistencies when it comes to analyse shale pore structure parameters (i.e., porosity, pore size distribution (PSD), specific surface area (SSA), pore volume (PV)), which are the key petrophysical properties controlling shale gas adsorption and significantly influence the estimation of hydrocarbon storage, fluid transportation and gas production capacity. Moreover, shales develop micro/mesopore network associated with clay minerals and organic matter (OM), which demonstrate high heterogeneities in different shale formations or in different depth of the same shale formation. The compositional heterogeneity consequently leads to large variations in pore structure parameters, nevertheless, there are many uncertainties exhibited in quantifying the relationships between pore structure parameters and shale compositions.

This research is conducted to quantitatively evaluate shale pore structure by using shale samples from different formations considering the mineralogical composition and total organic carbon (TOC) content. Multi-scale pore structure characterization techniques such as advanced non-destructive Nuclear Magnetic Resonance (NMR), low-pressure N_2 gas adsorption (LP-N_2-GA), low-pressure CO_2 gas adsorption (LP-CO_2-GA), mercury injection capillary pressure (MICP) were applied in couple with X-ray diffraction (XRD) and Rock-Eval Pyrolysis. Our results show that the major pore structure characterization inconsistency between NMR and other fluid penetration methods is mainly generated by clay bound water (CBW), which can be quantified by applying NMR T_2 cutoff method under the thermal dehydration scheme. The recommended dehydration temperature of 75°C was raised to maximally remove capillary water while keeping the sensitive clay and microstructure well-preserved. Applying dehydration temperature of 75°C into NMR T_2 spectrum allows the quantification of effective porosity and CBW in shales. CBW, which demonstrates a

linear positive relationship with clay contents, is intimate with micro-/mesopore pore surface and structure geometric fractals. NMR-derived CBW fractal dimension (D_{cbw}) is linear positively correlated with the fractal dimension of micropore surface (D1) and CBW volume. NMR-derived effective pore fractal dimension (D_{eff}) is linear positively correlated with the fractal dimension of meso/macropore volume (D2) and demonstrates a good positive correlation with gas storage capacity. CBW is therefore considered to largely complicate the fractal geometry of nanopore network and potentially resist effective fluid flows in shales. The nanopore surface of higher heterogeneity (higher D1) associates with larger surficial CBW retention and would further reduce the effective pore space for fluid transportation. The meso-/macropore volumes of higher complexity (higher D2) is intimate with the larger heterogeneity in effective pores for the higher potential of hydrocarbon storage capacity in gas shales. To clarify the specific impact of clay minerals on micro-/mesopore system, and differentiate it from the impact of organic matter pores, kerogen isolation was carried out on OM-rich shale samples. Quantitative analysis reveals that the mesopores ranging between 2 nm and 17 nm are specifically controlled by clay mineral pores. Micropores less than 2 nm are predominantly contributed by organic matter, while meso-/macropores larger than 17 nm contains both clay and organic matter pores. Equations are further established to predict the specific pore volume and surface area as a function of clay and TOC contents in different shale types, providing implications for the precise formation evaluation in downhole practices.

Acknowledgments

Looking backwards, this PhD study constitutes one of the most amazing journey in my life that I had never imagined and experienced, challenging and exciting, like a roller coaster with unexpected ups and downs. I appreciate the unique experience and owe sincere gratitude to many people around who care about me, support me, help me and guide me to experience, to learn, to reflect, and to grow up not just in the knowledge world but also in the life university to obtain the philosophy of everyday life.

I would like to express my most sincere gratefulness to my supervisor Prof. Reza Rezaee. Thank you for guiding me into the mysterious scientific world by providing me with the precious research opportunities and supports since I was an undergraduate student working on final year project in Curtin University. I really appreciate the philosophies, the independence, and the trust you provided me throughout the whole journey of the knowledge exploration. I cherish the analytical and critical thinking developed under your guidance that constitute who I would like to be as an independent scientific explorer from the long-term perspectives. I also want to thank my co-supervisor Associate Prof. Ali Saeedi for the encouragements particularly in my earlier PhD stages. I extend many thanks to the support I have received from the friends and fellows in discipline of Petroleum Engineering, Western Australian School of Mines (WASM).

Special thanks to my friends from Unconventional Gas Research Group (UGRG): Dr. Hongyan Yu, Dr. Jie Zou, Dr. Nadia Testamanti, and Dr. Hongcai Wang. Thank you Hongyan for the friendship, I am grateful for your supports, encouragements and the insightful discussions on my project based on your experience. To Jie, thank you for guiding me with gas adsorption facilities, and providing the valuable suggestions and discussions for me to conquer the difficulties along the journey. I appreciate Nadia, for activating my initial curiosity and great interests in shale gas research since I was doing my undergraduate project in UGRG Team. Thank you for giving me the patient trainings on NMR facility, and supporting me with the inspiring suggestions, and discussions. To Hongcai, thank you for your valuable advices on my PhD application and the subsequent PhD research topics. Gratitude also goes to my current fellows from our UGRG Team: Dr. Pooya Hadian and Dr. Lukman Johnson for spending your time helping with XRD and Rock-Eval. I thank Bob Webb, the former technical officer in Petroleum Engineering, for his laboratory support, and the sharing of Australian

culture and insightful perceptive of Chinese Daoism philosophy. Special gratitude goes to Dr. Si-Yu Hu (CSIRO), for the inspiring spirits and moral supports that encourage me to do further exploration in such an amazing scientific world. Thank you Mr. Michael Verrall (CSIRO), for generously providing XRD facility guidance, operation assistance, and data interpretation support. I also thank the technical officer Xiao Hua in Chemical Engineering, for providing the instrument access and strong supports during the journey.

Much gratitude goes to Associate professor Mofazzal Hossain, thank you for supporting me in scholarship application, and sharing your valuable life philosophies. Thank you Dr. Christopher Lagat, for conveying your industrial experiences and always encouraging me to have a broader vision and self-confident to catch more opportunities in professional career. Thank you Dr. Sam Xie, for sharing the helpful scientific writing books and your experiences in teaching and research.

Special thanks for Associate Professor Stuart Higgins. Thank you for the wide and insightful talks regarding Subsea Engineering, career pursuing, economy, culture, music, travelling, which are inspiring and enrich my whole PhD journey. Thank you for the spiritual supports you provided that fully encourage me to achieve a better living and learning outcomes, together with the potential life possibilities. I also extend my acknowledge to the other friends for sharing the wonderful time during my PhD in no particular order: Emad Al-Khdheeawi, Dawei Pan, Eghan Arjomand, Mohsen Ghasemi, Yihuai Zhang, Cut Aja Fauziah, Ruby Lo, Zheng Law, Surudee Bunpitakgate, Nichole Sik, Jimmy Li, Jamiu Ekundayo, Moustafa Elzeftawy, Faranak Parvinpour, Junfang Zhang (CSIRO), Xiubin Qi (CSIRO), Valentina Taranovic (CSIRO), Anusuriya Devaraju (CSIRO), Xingguang Xu (CSIRO), Zhiqi Zhong, Runhua Feng, Muhammad Atif Iqbal, Partha Pratim Mandal, Hongyang Zhang, Nihemaiti Maolida, Suona Zhang, Danlei Wang, Tolu Olu-Ojo, Linping Zeng, Faaiz Al-Shajalee, Omar Al-Fatlawi, Dhifaf Sadeq, Alison Barker, Melissa Byrne, Nadia Quinn, Elizabeth Ngo, Michelle Mok, Francesca Renkema, Gemma Nugent.

Much gratitude is expressed to the groups and organizations providing financial supports, facility assistance, and tested samples. Thanks to Unconventional Gas Research Group (UGRG), the discipline of Petroleum Engineering, the discipline of Chemical Engineering in Western Australian School of Mines (WASM), the

Microscopy & Microanalysis Facility (MMF) of John De Laeter Centre in Curtin University, the Commonwealth Scientific and Industrial Research Organisation (CSIRO), and the Particle & Surface Sciences Pty. Ltd for their facility assistances. Thanks to the Finder Energy and the Department of Mines, Industry Regulation and Safety under the Government of Western Australia for granting the core samples under Approval Nos. G32825 & N00413. Much gratitude goes to GWWA Inc. Scholarship for their support to enhance the quality of my PhD project. Very much special and sincere acknowledgements to China Scholarship Council- Curtin International Postgrad Research Scholarship (CSC-CIPRS, Grant No. 201606450018) for their financial support to the whole project.

Nothing could express how deepest appreciation and gratefulness I hold to my mom and dad, for your unconditional love, your consistent support and encouragement on each of my decision. By devoting yourselves into petroleum industry, you make me realize how lucky and proud I am to be born and grew up listening to your stories about how petroleum establish our city, nourish our people and support the whole country. Thank you for bringing me in front of petroleum world and make me realize what an amazing world existed within the porous media of the rock and how much significance the rock bears for the future world. All I have and will achieve are only possible on account of your selfless love and infinite sacrifices.

Table of Contents

List of Figures

List of Tables

CHAPTER 1 Introduction

1.1 Significance and Motivation

Over the past decades, the world has announced to enter the "golden age of gas". A report by the International Energy Agency (IEA) proclaimed that "Natural gas is poised to enter a golden age, but this future hinges critically on the successful development of the world's vast unconventional gas resources".

Shale gas, as one of the most fundamental unconventional gas resources, has increasingly influenced the global oil and gas market since the United States firstly announced their successful commercial production of shale gas around 2006, followed by the ten-fold production increases between 2006 and 2010 (McGlade et al. 2013). Shale gas is still holding a promising prospect of energy supply in the following decades (**Figure 1. 1**), which undoubtedly, attracts an intensive global attention in fundamental shale gas research.

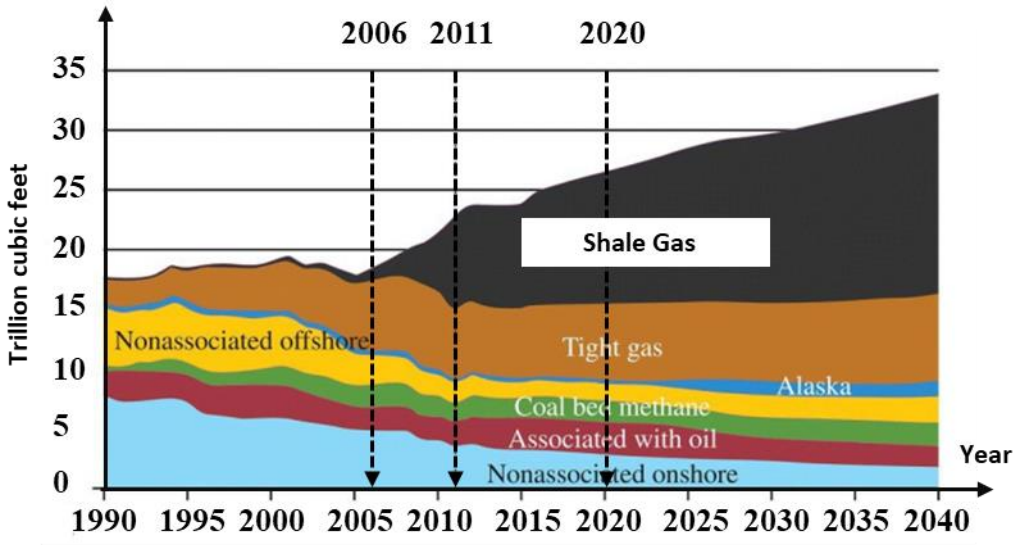

Figure 1. 1 Natural gas production (1990-2040) in the United States per U.S. Energy Information Administration 2013 (Rezaee 2015).

Different from conventional rocks (e.g., sandstone or limestone), shales are the fine-grained sedimentary rock that is formed by the consolidation of clay (less than 4 μm in diameter) and may contain variable amounts of silt-sized particles (between 4 and 62.5 μm in diameter) with tight texture (Folk 1980, Javadpour 2009, Passey et al. 2010)), the complicated pore structure (i.e., with extremely low permeability and porosity), and a wide range of pore size distribution

(i.e., pore size ranges from the micropores less than 2 nm to the micrometer pores). Commercial shale gas production essentially relies on the estimation of gas storage capacity and gas transportability in the complex pore structure, which demonstrates a tremendous variation from conventional rocks (Labani et al. 2013, Rezaee 2015). In shale reservoirs, gas is principally stored in different forms (**Figure 1. 2**): (1) free gas in pore space or fractures generated during diagenetic or tectonic processes (Jarvie et al. 2007, Caineng et al. 2016); (2) adsorbed gas on the pore surface of clay minerals or organic matter (OM), and (3) a small amount of dissolved gas. The fundamental storage mechanism of free and adsorbed gas emphasizes the significance of shale pore structure characterization. The estimation of hydrocarbon accumulation in shale plays is largely dependent on pore structure parameters such as effective porosity, pore size distribution (PSD), the pore volume and specific surface area (SSA) of micropores (pore sizes < 2 nm) and mesopores (pore sizes between 2 and 50 nm) (Rouquerol et al. 1994), and influenced by the heterogeneous pore geometry and pore surface roughness that can be quantitatively analyzed by fractal theory. Micro-/mesopores exhibit large specific surface area and considerable pore volume for adsorption capacity and fluid transportation in shale. The micro-/mesopore system, developing in clay mineral and OM, is documented to take the main control of shale gas storage (Chalmers et al. 2012, Keller et al. 2011) and significantly varies in different shale formations that are highly heterogeneous in compositions (OM and minerals) (**Figure 1. 3**) (Curtis et al. 2012).

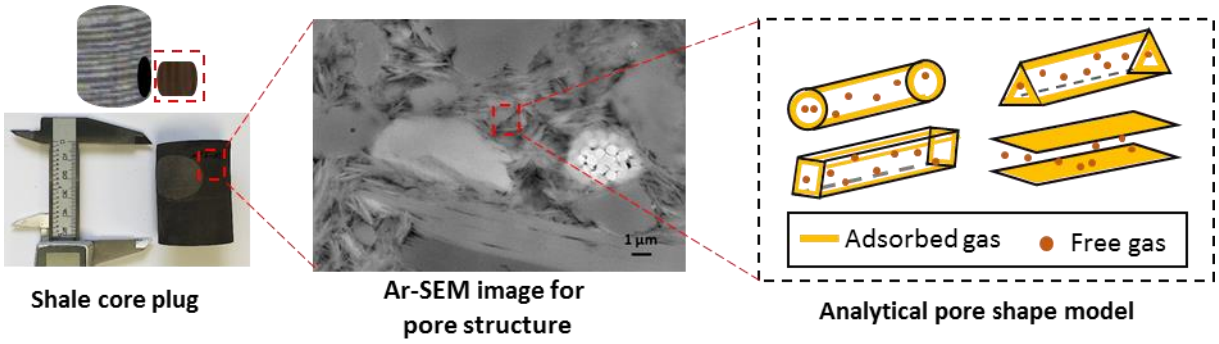

Figure 1. 2 Shale gas storage in the complex pore structure.

1.2 Research gaps and objectives

The determination of fundamental pore structure properties on conventional sandstones and carbonates are well-established. However, pore structure properties has been arguably unknown for shales due to their unconventional characteristics. As effective porosity and PSD are the most essential parameters controlling shale gas storage capacity and fluid transportation

property for the estimation of reservoir volume, the geomechanical, petrophysical, and geochemical properties for oil and gas production, it is crucial and urgent to combine various techniques and clarify their application for a comprehensive and accurate pore structure studies in shale.

Regarding the commonly applied pore structure characterization methods, big achievements have been reached in decades for the detection of small-scaled nanopores. Three method of approaches for pore structure investigations are summarized with advantages and limitations: (1) The radiation scattering approaches, such as small angle neutron scattering (SANS) and ultra-small angle scattering (USANS) techniques, are efficient and powerful to quantify porosity, pore fluids, and the continuous PSD from 0.2 nm to 10 μm in tight sandstones (Clarkson et al. 2012a) and coals (Radlinski et al. 2004, Melnichenko et al. 2009). However, the application in shale system has been debatable (Radlinski 2006). (2) The visual-oriented microscopies, i.e., transmission electron microscopy (TEM) and focused ion beam-scanning electron microscopy (FIB-SEM) are capable to provide the high-resolution image of pore structure morphologies. Nevertheless, microscopies are not available to provide the full range of PSD and not capable for quantitative determinations, thus limit the usage in shale quantitative assessment (Furmann et al. 2016). (3) Fluid penetration methods, i.e., low-pressure CO_2 gas adsorption (LP-CO_2-GA), low-pressure nitrogen gas adsorption (LP-N_2-GA), mercury intrusion capillary pressure (MICP) and nuclear magnetic resonance (NMR), enable a wide detection of PSD in shales (Ross and Bustin 2009, Rezaee et al. 2012, Yuan et al. 2018b). The associated drawback, however, is the inconsistent result in porosity and PSD between those methods (e.g., up to 50% porosity discrepancy and PSD divergences) (Saidian 2015).

Numerous research gaps and lack of understandings exist in shale pore structure investigation, which are summarized as below:

- Shale is composed of numerous clay minerals and organic matter, which develop various pore types that are mostly not interconnected, with extremely low permeability and low porosity for accurate detection.
- The so-far conducted shale studies used plentiful approaches, however, pore structure interpretations for shale vary from different methodologies. The discrepancies of those techniques are largely influenced by shale types (clay-rich shales and clay-poor shales), and the sources of technical inconsistencies have not been fully addressed.

- The impact of clay bound water (CBW), as the main sources for the porosity discrepancy between NMR and other approaches, has not yet been able to be quantified and further investigated.
- Micro-/mesopore structure parameters (i.e., pore volume, SSA) that intimately correlated with CBW, are controlled by shale heterogeneous compositions and are poorly addressed.

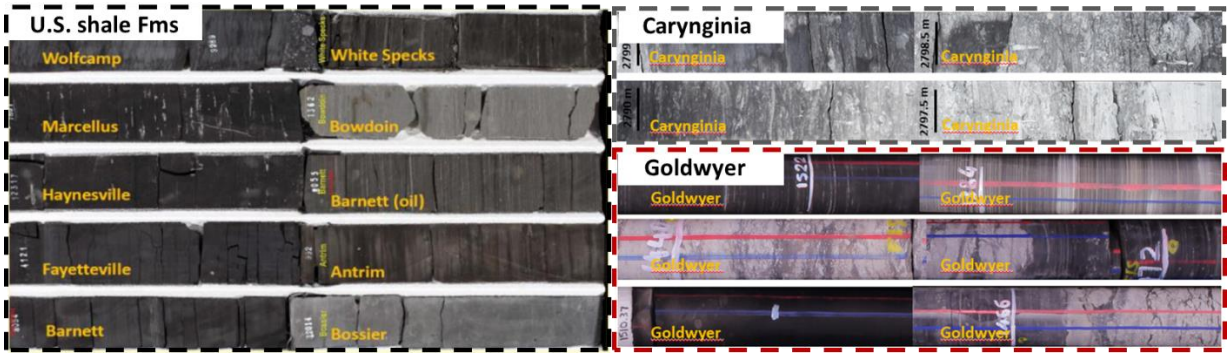

Figure 1. 3 Core photography of U.S. shale formations (left-hand side), and WA shale formations, i.e., Carynginia Fm. (Perth Basin), Goldwyer Fm. (Canning Basin) (right-hand side).

Considering the research significance, the motivations and gaps mentioned above, this PhD project aims to: (1) investigate the inconsistencies of different measurement techniques and justify their interpretations in different shale types; (2) elucidate the interrelationship between pore structure attributes (i.e., effective porosity, total porosity, clay bound water, pore size distribution, specific surface area, pore volume) and shale formations with a broad range of compositions (i.e., clay and TOC content). Specific purposes of this study include:

(1) Using NMR, low-pressure CO_2/N_2 gas adsorption, MICP, helium porosimetry, XRD and Rock-Eval to characterize shale pore structure properties and compositions;

(2) Investigating the sources of result inconsistency in pore structure characterization between different techniques in different shales (clay-rich and clay-poor shales).

(3) Elucidating the impact of clay bound water (CBW) on porosity/PSD discrepancies measured from NMR and other techniques (i.e., MICP, low-pressure gas adsorption, helium porosimetry), particularly in clay-rich shales (e.g., Permian Carynginia shales in Perth Basin, WA).

(4) Quantifying the volume of CBW in clay-rich shales by using NMR T_2 cutoff method.

(5) Investigating the fractal properties of pore surface and pore volume under the function of CBW, and correlate the attributes with storage gas capacity.

(6) Quantify the influence of shale compositions (TOC and clay content, paramagnetic minerals) on pore structure parameters such as micro-/mesopore surface area, pore volume, NMR-converted PSD.

1.3 Thesis Organization

A total of eight chapters are included to illustrate the objectives mentioned above. **Chapter 1,** as the introduction, provides a general description of the research background, gaps, objectives and the Chapters layout. **Chapter 2** demonstrates a literature review. **Chapter 3** to **Chapter 7** exhibits the results and discussions of five topics based on the published peer-reviewed journal papers under the whole project. **Chapter 8** performs as a conclusion.

A brief summary of **Chapter 3** to **Chapter 7** is presented as below.

Chapter 3 presents comparative techniques for porosity and pore structure assessment in shales. Porosity and PSD are essential petrophysical parameters controlling permeability and storage capacity in shale gas reservoirs. Various techniques to assess pore structure have been introduced, nevertheless, discrepancies and inconsistencies exist between each of them. This chapter compares the porosity and PSD in two different shale formations, i.e., the clay-rich Permian Carynginia Formation in Perth Basin, Western Australia, and the clay-poor Monterey Formation in San Joaquin Basin, USA. Porosity and PSD have been interpreted based on nuclear magnetic resonance (NMR), low-pressure N_2 gas adsorption (LP-N_2-GA), mercury intrusion capillary pressure (MICP) and helium expansion porosimetry. The results highlight NMR with the advantage of detecting the full-scaled size of pores that are not accessible by MICP, and the ineffective/closed pores occupied by clay bound water (CBW) that are not approachable by other penetration techniques (e.g., helium expansion, low-pressure gas adsorption and MICP). The NMR porosity is largely discrepant with the helium porosity and the MICP porosity in clay-rich Carynginia shales, but a high consistency is displayed in clay-poor Monterey shales, implying the impact of clay contents on the distinction of shale pore structure interpretations between different measurements. Further, the CBW, which is calculated by subtracting the measured effective porosity from NMR total porosity, presents a good linear correlation with the clay content ($R^2 = 0.76$), implying that our correlated equation is adaptable to estimate the CBW in shale formations with the dominant clay type of illite.

Considering that CBW would largely generate the inconsistent interpretations in clay-rich shales, it is significant to quantify the volume of CBW particularly in clay-rich shales, for one purpose, to evaluate the extent of effective porosity reduction induced by CBW; for another purpose, to explore CBW quantification from laboratory NMR perspectives. **Chapter 4** provided the solutions by investigating the quantitative laboratory determination of CBW in clay-rich Carynginia shales from Perth Basin, Western Australia.

It has been acknowledged that low-field nuclear magnetic resonance (LF-NMR) was extensively applied to characterize petrophysical properties (e.g., clay bound water, porosity, PSD) of reservoirs. However, limited understanding remains for unconventional shales. Defining NMR T_2 cutoff to differentiate CBW from free water is a challenge in shales since conventional approach, such as using centrifuge, is not feasible to completely remove free water in tight shales. Thermal treatment is therefore suggested for further extraction of movable pore water, however, the influence of temperature on nanoscale pore structure and clay mineralogical composition has been underestimated in previous studies and thus requires further investigation.

This chapter re-defines the critical dehydration temperature for accurate PSD interpretation in Permian Carynginia shale, Western Australia to determine T_2 cutoff for CBW. By using low-pressure N_2 gas adsorption (LP-N_2-GA) in parallel with LF-NMR, we identified a striking anomalous PSD consistency for critical temperature detection and verification. Our results show that movable pore water can be maximally removed around 80°C (75°C), while the sensitive clay, CBW and microstructure are well-preserved for accurate petrophysical evaluation. Clay mineral conversion would occur when temperatures are higher than 80°C, while temperatures lower than 75°C would induce large misinterpretations for nanopore structure. Our recommended scheme could provide a potential adaptability for the formation evaluation of Permian Carynginia shale in the downhole practices.

Considering 80°C was determined as the critical temperature for CBW (**Chapter 4**), which would affect the pore geometric heterogeneity that is intimated with gas adsorption, therefore, further quantification of pore geometric heterogeneity was conducted by using fractal theory (**Chapter 5**). Fractal dimension (D) is a critical parameter to estimate the heterogeneity of complex pore structure in shale gas reservoirs. To quantify the fractal dimension of various pore types and evaluate their implications on shale effective porosity and gas storage capacity in potential, we performed fractal analysis based on experimental results of low-field nuclear

magnetic resonance (LF-NMR) and low-pressure N_2 gas adsorption (LP-N_2-GA) in Permian Carynginia shales. By comparing the calculated fractal dimensions based on the two approaches, we analyzed the 'surface fractal dimension' for ineffective pores occupied by clay bound water (CBW) and the 'volume fractal dimension' for effective pores (D_{eff}) in shales for the first time. The NMR-based CBW fractal dimension (D_{cbw}) is linear positively correlated with the fractal dimension of micropore surface (D1) (R^2= 0.91) and CBW volume (R^2= 0.58), while negatively correlated with effective porosity (R^2= 0.58). The NMR-based effective pore fractal dimension (D_{eff}) is linear positively correlated with the fractal dimension of meso/macropore volume (D2) (R^2= 0.82) and presents a good positive correlation with gas storage capacity (R^2= 0.80). Our results imply that CBW largely complicates the fractal geometry of pore network and potentially resist effective fluid flows in shales. The pore surface of higher heterogeneity (higher D1) associates with larger surficial CBW retention of higher fractal values and would further block the effective pore space for fluid transport. The meso-/macropore volumes of higher complexity (higher D2) is intimate with the larger heterogeneity in effective pores for the higher potential of hydrocarbon storage capacity in gas shales.

Micro-/mesopore pore volume and surface area, which are intimately correlated with CBW, are highly influenced by shale compositions. **Chapter 6** correlated the micro/mesopore structure attributes with shale compositions from a wide range of clay and TOC contents.

Pore structure properties such as pore volume, surface area, and pore size distribution (PSD) are the key petrophysical parameters in shales that control storage capacity, hydraulic conductivity, and gas adsorption in potential. The nature of pore volume, surface area and PSD are largely dependent on shale composition, which is highly heterogeneous in different formations. However, the quantitative effects of the clay content and total organic carbon (TOC) content on micropore and mesopore structural properties have not been fully explored yet. Here, we quantified the impact of clay and TOC contents on micro-/mesopore volume, surface area, and PSD using three shale formations with various compositional variations. The results indicate that clay and TOC contents synchronically influence the shale micro/mesopore structure properties, but they function in different pore size ranges. The micropores are predominantly contributed by organic matter pores. For the first time, we discover the mesopores ranging between 2 nm and 17 nm are primarily controlled by clay mineral pores, and the pores larger than 17 nm contains both clay and organic matter pores. We further develop four new equations to predict micropore volume, mesopore volume, micropore surface area, and mesopore surface area as a function of clay and TOC contents based on the data

collected from the three different shale types. The statistical analysis shows that our developed correlations are capable of predicting the pore structure properties in our investigated formations with acceptable accuracy. The newly established equations provide insightful implications for the precise formation evaluation in downhole practices.

Apart from TOC and clay contents, factors such as paramagnetic minerals also generate large contributions to shale pore structure interpretation, particularly for NMR technique. **Chapter 7** discussed how paramagnetic minerals would influence NMR-PSD interpretation in shales.

Pore size distribution (PSD) is a fundamental petrophysical parameter that can be converted from Nuclear magnetic resonance (NMR) transverse relaxation time (T_2) spectrum via surface relaxivity (SR). Technically, SR is utilized as a constant value in the entire formation, whereas the laboratory calculated SRs revealed that they are likely to vary with mineralogy and can be influenced by Fe-bearing paramagnetic minerals, which could further affect NMR-converted pore structure properties. This study was performed on Permian Carynginia shale samples to compare the NMR-converted PSD with that measured by mercury injection capillary pressure (MICP). The surface relaxivity was calculated from the logarithmic mean T_2 value ($T_{2,lm}$) based on NMR measurement and the surface to volume ratio (SVR) based on low-pressure nitrogen gas adsorption (LP-N_2-GA). The results show that Fe-bearing paramagnetic mineral contents are linear positively correlated with SR values, which were calculated to range between 0.08 and 0.32 μm/s in our tested samples. The paramagnetic mineral of higher content expedites the NMR T_2 surface relaxation rate, leading to the divergent shifts in NMR-converted PSD curves.

1.4 Publications Outline

This thesis is arranged based on the five peer-reviewed journal publications listed below, which accordingly correspond to separate chapters. Also, one published conference paper content is involved in the thesis.

Chapter 3

Yuan, Y., and Rezaee, R., 2019, Comparative Porosity and Pore Structure Assessment in Shales: Measurement Techniques, Influencing Factors and Implications for Reservoir Characterization: Energies, v. 12, no. 11, p. 2094.

Chapter 4

Yuan, Y., Rezaee, R., Verrall, M., Hu, S.-Y., Zou, J., and Testmanti, N., 2018, Pore characterization and clay bound water assessment in shale with a combination of NMR and low-pressure nitrogen gas adsorption: International Journal of Coal Geology, v. 194, p. 11-21.

Chapter 5

Yuan, Y., Rezaee, R., 2019, Fractal analysis of the pore structure for clay bound water and potential gas storage in shales based on NMR and N_2 gas adsorption: Journal of Petroleum Science and Engineering, v. 177, p. 756-765.

Chapter 6

Yuan, Y., Rezaee, R., Al-Khdheeawi, E., Hu, S.-Y., Verrall, M., Zou, J., and Kouqi, L., 2019, Impact of Composition on Pore Structure Properties in Shale: Implications for Micro-/Mesopore Volume and Surface Area Prediction: Energy & Fuels, v. 33, 9619-9628

Chapter 7

Yuan, Y., Rezaee, R., 2019, Impact of paramagnetic minerals on NMR-converted pore size distributions in Permian Carynginia shales: Energy & Fuels, v. 33, no. 4, p. 2880-2887.

CHAPTER 2 Literature review: matrix, pore and fluid in shales

"Shale" has been used as terminology to describe a laminated fine-grained argillaceous rock. Different from conventional reservoir, which is relatively easy to characterize and develop; and have a good reservoir quality (e.g., larger porosity and permeability generated by pore space between larger grains such as quartz and feldspar with the particle size ranging between 62.5 μm and 2000 μm in diameter), unconventional shales require more advanced technique on purpose to obtain the high-price commercial products and the potential large reserves (**Figure 2. 1**) fundamentally based on the comprehensive understandings and accurate evaluations of the pore system.

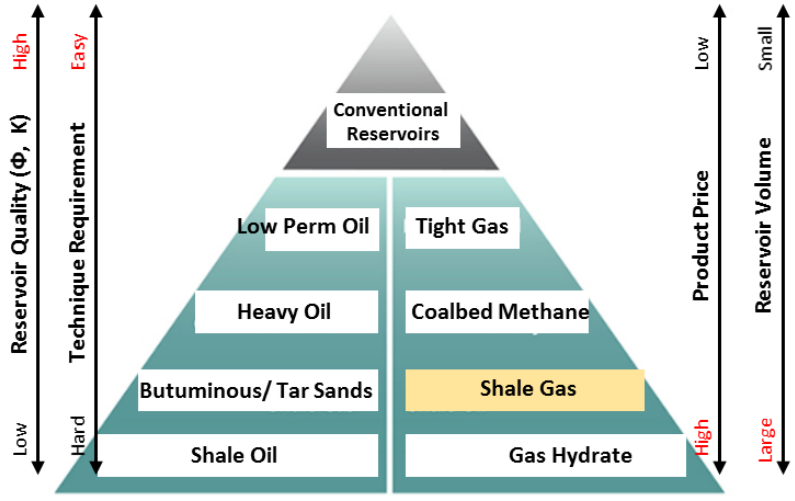

Figure 2. 1 The conventional and unconventional oil and gas resource pyramid (modified from Holditch (2003)).

2.1 Pore system in shale

2.1.1 Pore classification

Pore system of sedimentary rocks is consisted of interconnect (effective) and isolated (ineffective) pore space. Reservoir pores, which are defined as "the small interstice or open space allowing the passage or adsorption of liquid or gas" (Stokes and Varnes 1955), generally contain formation water, hydrocarbon (oil, gas, condensate), air or other fluids. In shale gas systems, the pore spaces together with natural fractures constitute the space for shale gas storage and flow pathway. Regarding pore size terminology, International Union of Pure and Applied Chemistry (IUPAC) established a pore category system by subdividing the pores into three categories: micropores (< 2 nm), mesopores (2–50 nm), and macropores (> 50 nm)

(Rouquerol et al. 1994). This pore classification is significant for the formation evaluation of unconventional shale gas and coalbed methane. Documents revealed that micropores and mesopores are essentially presented in unconventional reservoirs for gas production due to their contribution to pore volume and storage site (pore surface area) for methane adsorption (Chalmers et al. 2012, Ross and Bustin 2008, Chalmers and Bustin 2007). Additionally, methane transmission mechanisms (i.e., diffusion and advection) are also intimated with micropore and mesopore systems.

Another widely acknowledged pore category was established based on shale matrix components (i.e., minerals and organic matter): the interparticle mineral pores, intraparticle mineral pores, and organic matter pores (OM pores) (Loucks et al. 2012). Interparticle mineral pores are developed between mineral particles and crystals, whereas, intraparticle mineral pores grow within mineral particles (mostly within clay minerals). OM pores are those intraparticle pores resided within OM. It was documented that the effective pore network in shale is more likely to be formed by interparticle mineral pores and intraparticle OM pores due to their possibility of interconnectivity, however, the intraparticle mineral pores may possibly fall into ineffective pores.

2.1.2 Porosity and Pore size

Porosity, as the most essential petrophysical property to evaluate hydrocarbon storage capacity, is conventionally defined as the ratio of the volume of the pore or void to the bulk volume of the rock (Katz 1959). Total porosity describes the whole pore space, both interconnected pores and dead-end pores, while effective porosity is particularly referred to as the interconnected pores. Generally, porosity is determined by two techniques, i.e., logs and core measurements, which may demonstrate different porosity interpretation results. Logs collect information at reservoir conditions and obtain porosity value using relevant models (Hook 2003). By contrast, core analysis conducted in the laboratory provides direct pore structure information. Essentially, the laboratory core analysis involves the procedure of pore fluid extraction and the subsequent test on cleaned samples. It should be noted that the term "porosity" may be referred differently in different contexts. The term "porosity", from a core analyst perspective, represent the pore space that is able to be accessed in particular techniques (e.g., fluid penetration approach, radiation approach). The "porosity" used in the following content is referred to as the porosity obtained from the laboratory.

When considering the porosity determination in shale, it has always been a challenge for working fluids to fully access the pore structure due to the fine-grained tight texture and complicated pore structure. Currently, there is no technique that is able to individually access the wide range of pore size distribution in shales, meanwhile, a synoptical combination of various approaches could not properly work due to the inconsistencies and discrepancies (Mastalerz et al. 2013).

2.2 Matrix and pore-fluid system in shale

2.2.1 Shale Matrix

The common volumetric model used for shales is composed of the matrix components and the pore space containing various fluid types (**Figure 2. 2**). As shown in the schematic, the matrix component consists of the dry-clay minerals, non-clay minerals and organic matter. Pore space in shales is mainly filled with water (i.e., clay-bound water, capillary water, movable water) and hydrocarbon (i.e., dry gas, condensate, or the oil with various viscosity), while in this research the major focus

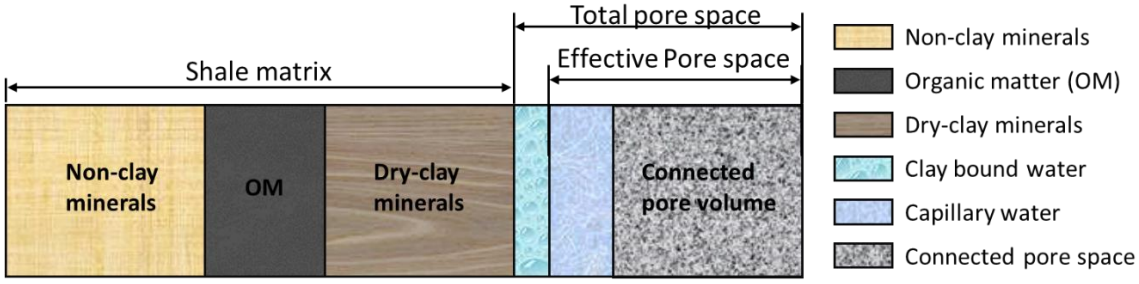

Figure 2. 2 Schematic of petrophysical shale matrix and pore space model (modified after Eslinger and Pevear, 1988)

2.2.2 Clay Mineralogy and Clay-Bound Water (CBW)

Clay minerals account for more than 30 wt.% in most shales and are recognized as the major cause of complex nanopore structures. Shale petrophysical properties intimated with fundamental pore structure are largely dependent on clay contents and types. The common clay minerals in shale system are illite, mixed-layer illite-smectite, kaolinite, and chlorite (**Figure 2. 3**), which are originally generated by the weathering and decomposition of igneous rocks. Clay minerals exhibit small sizes in grains, therefore, holding a large amount of capillary-held water (CHW), which is presented in small pores or pore throat under the function of capillary

pressure, and would block pore space and decrease the effective free and adsorption gas capacity. Clay minerals (e.g., smectite) develop enormous specific surface area (e.g., up to 800 m^2/g) with a large sum of negatively charged aluminosilicate layers with ions on pore surfaces, waiting to combine with the cations from the surrounding formation water. The intensive interaction between clay surfaces and water molecules results in the generation of clay-bound water (CBW). CBW is defined as the water electrochemically bound on clay surface that would largely reduce effective porosity and influence the gas adsorption behavior (**Figure 2. 4**). The volume of CBW constitutes the non-displaceable (immoveable) pore fraction that is consistent with ineffective porosity in reservoirs (Topór et al. 2016, Kuila 2013). Since shales are characterized by abundant clay contents, the effective porosity, which fundamentally intimated with hydrocarbon accumulation and production, would be largely reduced owing to the impact of CBW (Clavier et al. 1984). From petrophysicist perspectives, the volume of CBW is the difference between effective and total porosity (**Figure 2. 2**) (Coates et al. 1999, Prammer et al. 1996, Rezaee 2015). Conventional rocks such as sandstones demonstrate little difference between effective and total porosity, indicating small CBW presence, whereas, unconventional shale formations, particularly the clay-rich shales, exhibit larger porosity gaps. CBW essentially influence well log interpretations, therefore, accurate porosity measurement and CBW quantification is a significant topic required to be clarified.

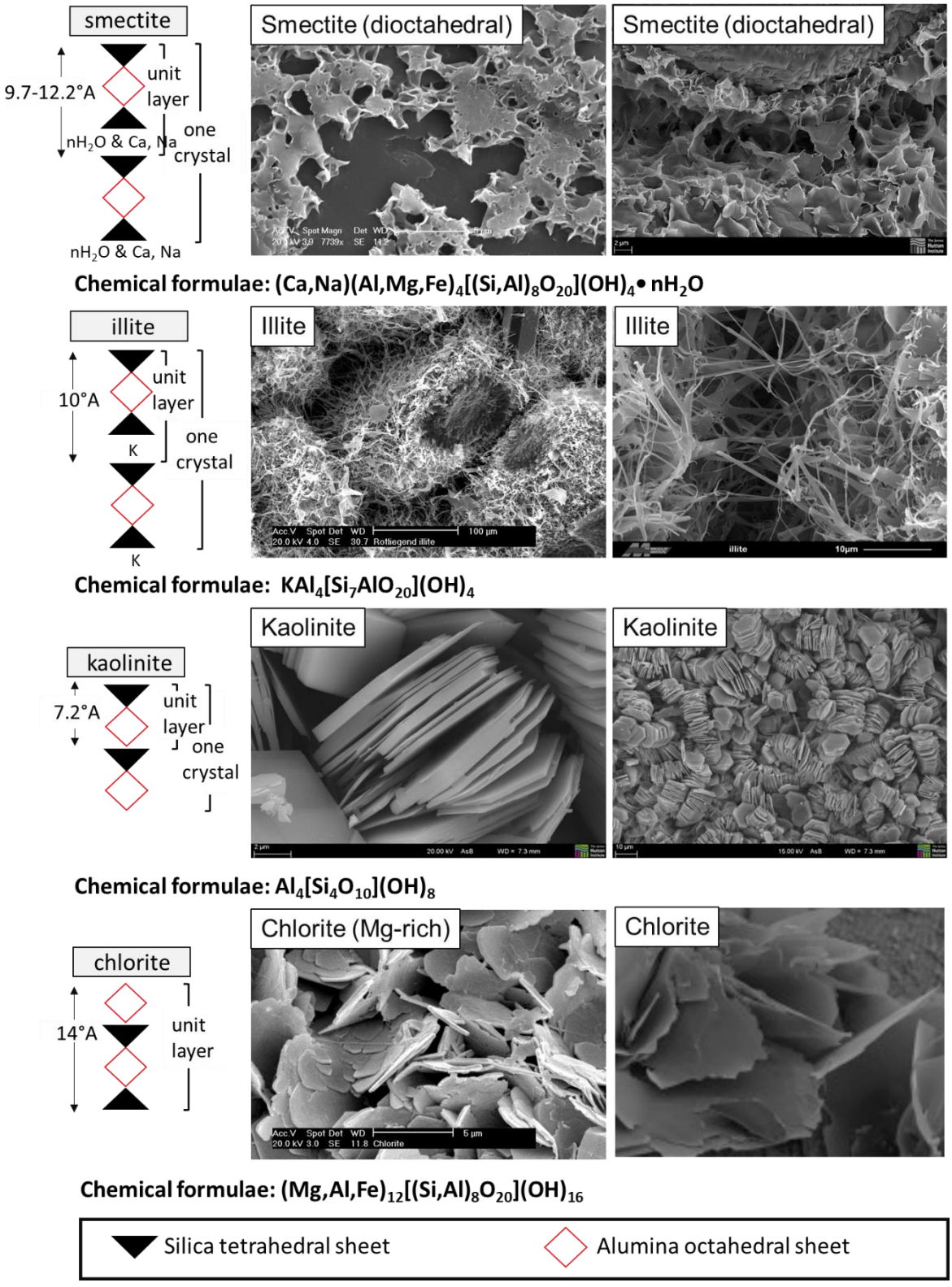

Figure 2. 3 The crystal structure and SEM images of four typical clay minerals (smectite, illite, kaolinite, chlorite) in shales. *Images reproduced from the 'Images of Clay Archive' of the Mineralogical Society of Great Britain & Ireland and The Clay Minerals Society (https://www.minersoc.org/images-of-clay.html)*

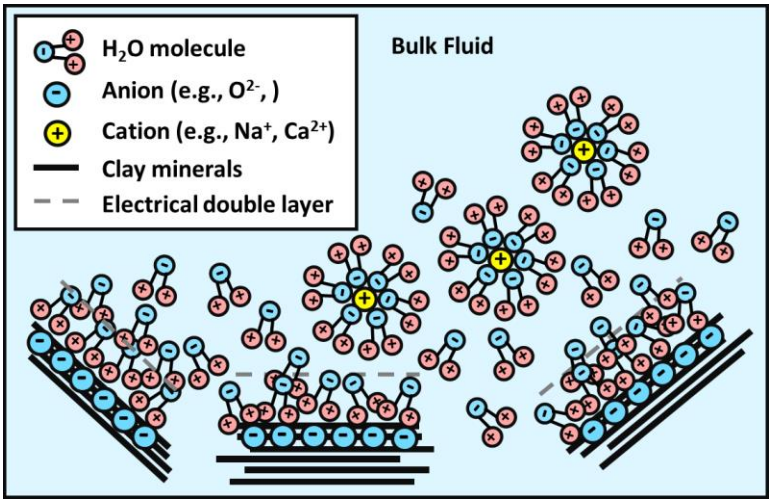

Figure 2. 4 Schematic of water adsorbed on the surface of clay minerals.

To quantify the volume of pore fluids in conventional rocks (e.g., sandstones or limestones), a fixed value of NMR T_2 relaxation time ($T_{2\text{-cutoff}}$) is generally used to differentiate various pore fluids within water-saturated core plugs. As shown in **Figure 2. 5**, the NMR T_2 spectrum is obtained from the core plugs under two conditions: (1) fully saturated and (2) partially saturated after high-rotation by a centrifuge. $T_{2\text{-cutoff}}$ divides the T_2 distribution into two sections: (1) The smaller pore section containing bound volume irreducible (BVI). BVI is the irreducible/immobile bound water that is not able to be removed by centrifuge in the lab, and could not be displaced by hydrocarbons during reservoir filling. (2) The larger pore size section with free flow index (FFI). FFI is the movable water that is able to be removed after applying the high-rotation centrifuge on the saturated plugs.

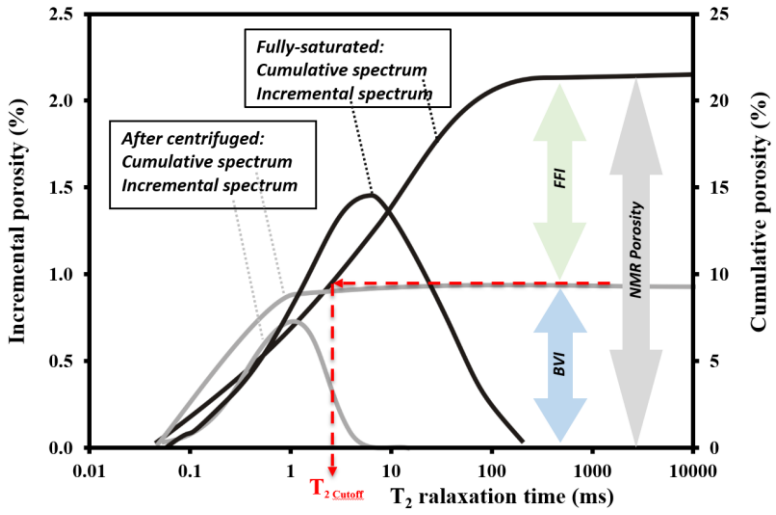

Figure 2. 5 NMR T_2 spectrum for conventional sandstones and the establishment of NMR $T_{2\text{-cutoff}}$ to differentiate pore fluids, i.e., free fluid index (FFI) and bound volume irreducible (BVI).

The use of centrifugal force to remove free water, however, could not work for shales to differentiate fluids due to a very high capillary force associated with their tight texture and complex pore structure. A tiny difference is presented between the NMR T_2 spectrum before and after centrifuge (**Figure 2. 6a**). Too much high rotation would destroy shale plugs due to their mechanical properties (**Figure 2. 6b**). CBW quantification and fluid differentiation in shale core analysis have been a challenging topic for decades. The problem was solved in this project by establishing a novel procedure (**Figure 2. 7**) that would be detailed in CHAPTER 4.

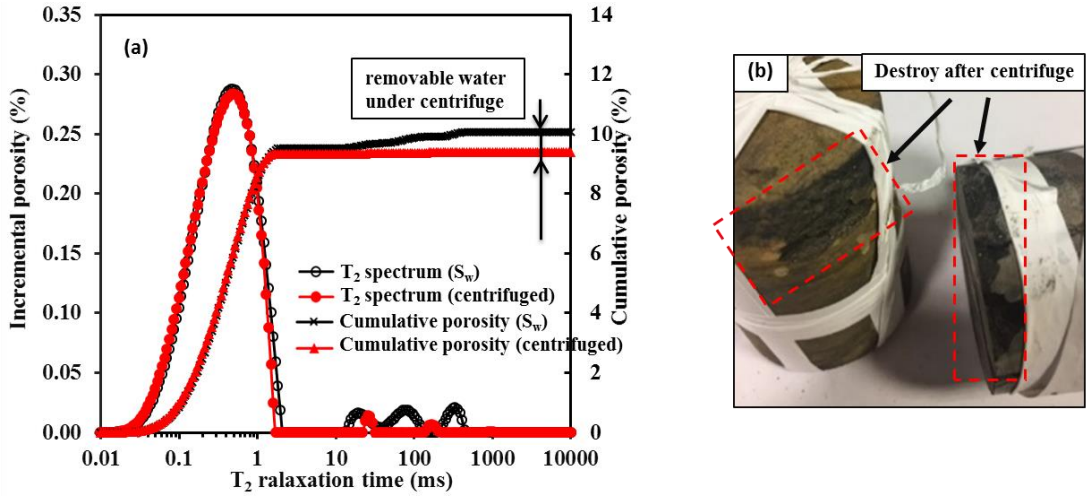

Figure 2. 6 (a) T_2 spectrum obtained under two conditions: fully saturated (S_w, black) and partially saturated after centrifuge (centrifuged, red); (b) destroyed samples after centrifuging at high rotation.

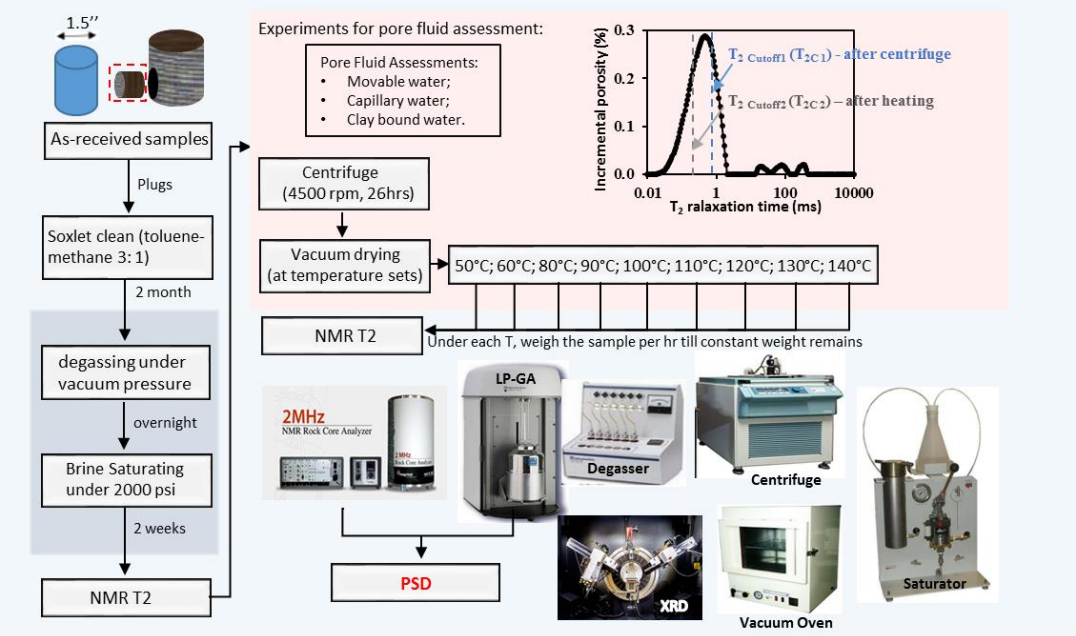

Figure 2. 7 Workflow to determine $T_{2\text{-cutoff}}$ for CBW quantification in shale by introducing vacuum heating after centrifuge.

CHAPTER 3 Comparative porosity and pore structure assessment in shales: measurement techniques, influencing factors and implications for reservoir characterization

This chapter is a published peer-reviewed journal paper:

Yuan, Y., and Rezaee, R., 2019, Comparative Porosity and Pore Structure Assessment in Shales: Measurement Techniques, Influencing Factors and Implications for Reservoir Characterization: Energies, v. 12, no. 11, p. 2094.

3.1. Introduction

The increasing demand of unconventional energy resources raises the significance of shale reservoir investigation (Curtis 2002, Clarkson et al. 2013). Shales are defined as the laminated fine-grained argillaceous sedimentary rocks, which are essentially constituted by minerals involving silt-sized particles (4-62.5 μm) and clays (<4 μm) in couple with organic matter (OM) (Chalmers et al. 2012, Rezaee 2015, Folk 1980, Javadpour 2009). The porosity and pore size distribution (PSD), performing as the most fundamental pore structure parameters to estimate gas storage capacity and fluid transporting behavior in shale complex pore structures (Labani et al. 2013, Rezaee 2015, Topór et al. 2016, Jia et al. 2018), are significantly associated with clay minerals and the promising OM that significantly varies between different shale formations (Sondergeld et al. 2010a, Mastalerz et al. 2013, Furmann et al. 2016, Loucks et al. 2009, Curtis et al. 2012). The clay mineral or OM develops the micropore (i.e., pores smaller than 2 nm per International Union of Pure and Applied Chemistry (IUPAC) classification (Rouquerol et al. 1994)) and mesopore (i.e., pores ranging from 2 nm to 50 nm per IUPAC classification (Rouquerol et al. 1994)) system, complicating shale pore structures and resulting in the extremely low permeability, low porosity and the large distinction of PSD in shales.

To date, three types of laboratory techniques are applied for pore characterization or quantification. Microscopy techniques, e.g., transmission electron microscopy (TEM) and scanning electron microscopy (SEM), perform as the helpful petrographic-imaging approaches for porosity estimation (Sigal 2015), however, provide objective results and are not adaptable to cover the full range of PSD in shales (Furmann et al. 2016). Radiation Scatterings, such as small angle neutron scattering (SANS) and ultra-small angle scattering (USANS) techniques, are capable to quantify the continuous PSD in tight sandstones (Clarkson et al. 2012a) and coals (Radlinski et al. 2004, Melnichenko et al. 2009). However, the applications in shale

systems are still under debate due to the limitation of neutron sources (Clarkson et al. 2013, Radlinski 2006, Bahadur et al. 2015, Bahadur et al. 2014). Fluid penetration methods, i.e., low-pressure (<18.4 psi) CO_2 gas adsorption (LP-CO_2-GA), low-pressure N_2 gas adsorption (LP-N_2-GA), mercury intrusion capillary pressure (MICP) and nuclear magnetic resonance (NMR), enable a wide range of pore structure detection and have been universally utilized in shale research studies (Knapp et al. 2018, Kuila 2013, Rezaee et al. 2012, Al Hinai et al. 2014, Yuan et al. 2018c, Ross and Bustin 2009, Saidian et al. 2014, Josh et al. 2012, Wang and Guo 2019). However, MICP displays destructive disadvantages and is not approachable to the pore throat sizes smaller than 3.6 nm (Sondergeld et al. 2010b, Chalmers et al. 2012, Mastalerz et al. 2013, Nelson 2009), merely inter-communicated pores are available for detection (Caineng et al. 2016). Helium expansion is attainable to the connected pore space corresponding to effective porosity, while the acquisition of PSD is not available (Labani et al. 2013). LP-CO_2-GA coupled with LP-N_2-GA is approachable to the pore sizes ranging from 0.35 nm to 200 nm (Barrett et al. 1951). However, only interconnected pores are accessible (Caineng et al. 2016), and the results are sensitive to measurement procedures and highly dependent on the sample pre-treatment such as the dewatering/ outgassing temperatures and the size of the smashed shale fragments (Holmes et al. 2017, Figini-Albisetti et al. 2010, Wang and Ju 2015). NMR, which is acknowledged as a non-destructive technique, is adaptable for measuring the total porosity and PSD in shales (Coates et al. 1999, Rezaee 2015, Straley et al. 1997, Schön 2015, Yuan et al. 2018c).

Unlike the conventional rocks displaying consistent results in porosity and PSD among different fluid-penetration measurements (Hossain et al. 2011), shales, however, tend to reveal significant discrepancies. For example, MICP porosity in Barnett shales exhibits ~25-50 % lower when compared to helium porosity values (Sigal 2013). Similar porosity inconsistencies up to 50 % have also been found in previous studies (Saidian et al. 2016, Katsube et al. 1992, Sondergeld et al. 2010b). To fully understand the variations of shale pore structure interpretation between different measurements, the comprehensive techniques are highly required to be combined and compared in parallel.

This paper discusses the discrepant results of different measurements for the two shales in typical composition (i.e., the Carynginia shales of Perth Basin in Western Australia and the Monterey shales of San Joaquin Basin in the U.S). Porosity is compared based on MICP, NMR and helium expansion. PSD is interpreted based on MICP, NMR, and low-pressure gas

adsorption. The influencing factors are discussed for result discrepancies. Implications are provided for shale gas reservoir characterization.

3.2. Materials and Methods

3.2.1. Shale samples

Shale samples from two formations were analyzed and compared between different measuring techniques. Carynginia samples, by the name of "AC1-AC8", were collected from Arrowsmith well in Perth Basin, Western Australia. Monterey shales, by the name of "M1-B-M10-B" and "M1-M6", came from well-1B and well-1, respectively, in San Joaquin Basin, the USA. Geological settings of Carynginia and Monterey shale formation were displayed in other studies (Yuan et al. 2018c, Rivera 2014).

Table 3. 1 shows the mineralogical composition in Carynginia and Monterey shales. Carynginia shales are characterized by abundant clay minerals, constituting 31.1-50.8 wt % of the total mineral contents (e.g., the average value of Carynginia clay content is 36.6 wt %). The quartz contents occupy 35.6- 53.2 wt % (e.g., quartz averages in 45.17 wt %), while the minorities are shown in K-feldspar, plagioclase and other minerals. Monterey shales present a low-clay content (e.g., the mean value of the clay content is around 9.0 wt %) but a relatively high proportion in quartz content. The clay type in both of Carynginia and Monterey shales have been identified as illite (Rivera and Prasad 2014, Yuan et al. 2018c).

Table 3. 1 XRD mineralogical composition for shales from Carynginia and Monterey formation. Some data were collected from other studies.

Name	Formation	Depth (m)	Total Clay (wt %)	Quartz (wt %)	K-Feldspar (wt %)	Plagioclase (wt %)	Other Minerals (wt %)
AC1	Carynginia	2780.2	50.8	35.6	2.6	5.0	6.0
AC2	Carynginia	2781.7	43.2	40.3	3.6	7.6	5.3
AC3	Carynginia	2789.9	32.3	47.6	5.4	9.4	5.3
AC4	Carynginia	2794.4	31.1	53.0	3.3	8.1	4.5
AC5	Carynginia	2806.4	40.7	41.3	3.6	7.6	6.8
AC8	Carynginia	2825.3	32.3	53.2	1.4	10.6	2.5
M1-B[1]	Monterey	1633.7	7.3	83.6	1.6	0.7	6.8
M2-B[1]	Monterey	1658.1	4.9	55.2	0.0	0.5	39.4
M3-B[1]	Monterey	2409.7	11.1	59.2	4.1	1.8	23.8
M4-B[1]	Monterey	2539.9	6.8	77.5	2.2	1.3	12.2
M5-B[1]	Monterey	2602.7	N/A	N/A	N/A	N/A	N/A
M6-B[1]	Monterey	2631.0	24.2	50.4	3.3	5.2	16.9
M7-B[1]	Monterey	2723.4	8.4	77.0	2.5	1.8	10.3
M8-B[1]	Monterey	2772.8	8.5	71.0	1.4	3.3	15.8

M9-B[1]	Monterey	2802.0	14.7	72.6	2.2	3.6	6.9
M10-B[1]	Monterey	2879.4	5.6	10.6	0.0	0.0	83.8
M1[1]	Monterey	1669.5	N/A	N/A	N/A	N/A	N/A
M2[1]	Monterey	2200.9	10.0	69.0	4.0	6.0	11.0
M3[1]	Monterey	2203.2	N/A	N/A	N/A	N/A	N/A
M4[1]	Monterey	2362.4	N/A	N/A	N/A	N/A	N/A
M5[1]	Monterey	2362.7	N/A	N/A	N/A	N/A	N/A
M6[1]	Monterey	2485.3	7.0	68.0	5.0	6.0	14.0

Note: [1] (Rivera and Prasad 2014)

3.2.2. Nuclear Magnetic Resonance (NMR)

Prior to NMR experiments, Carynginia shale plugs of 1.5' diameter were cleaned with toluene/methanol mixture and fully saturated with 30000 ppm brine that is matched with the average formation salinity. The low-field NMR measurements were performed on saturated samples by using 2 MHz Magritek Rock Core Analyzer, which was set under 30 ^{o}C with a P54 probe and conducted under the constant magnetic resonance frequency. NMR T_2 spectrum was acquired by using the experimental parameters, i.e., 100 µs inter-echo spacing (TE), 10000 ms inter-experiment delay, 10000 number of echoes and the minimum 200 signal to noise ratio (SNR), coupled with the Carr-Purcell-Meilboom-Gill sequence (Carr and Purcell 1954, Kenyon et al. 1995, Meiboom and Gill 1958).

Applying NMR T_2 spectrum to study shales pore structure is fundamentally established on the transverse relaxation dominated by surface relaxation mechanism (Coates et al. 1999):

$$\frac{1}{T_2} = \rho_2\left(\frac{S}{V}\right) \quad \text{.....(3.1)}$$

where T_2 is the transverse relaxation time; ρ_2 is surface relaxivity, which is considered as a constant value representing the strength of surface relaxation; $\frac{S}{V}$ is the surface volume ratio that is closely intimated with pore sizes. Pore size distribution could be interpreted via T_2 spectrum, with smaller pore sizes corresponding to shorter relaxation times.

3.2.3. Low-pressure gas adsorption (LP-GA)

Low-pressure N_2 gas adsorption (LP-N_2-GA) was applied to measure the pore size distribution (PSD) and the pore volume. Prior to the measurements, shale samples were crushed into fragments of 60 mesh sizes and degassed over 8 h for pore surface cleaning. LP-N_2-GA was performed on Micromeritics® TriStar 3020 instrument at the bathing temperature of 77.4

K. N_2 was penetrated into the degassed samples under the constant temperature for the acquisition of adsorption isotherm. PSD is obtained by using the Barrett, Joyner and Halenda (BJH) theory based on N_2 adsorption isotherm (Barrett et al. 1951). The interpretations were carried out on the embedded TriStar II 3020 standard software.

3.2.4. Mercury Injection Capillary Pressure (MICP)

MICP measurements were performed on Micromeritics Autopore IV 9500 V1.09 porosimeter on chip samples weighing around 10 g. Prior to the test, shale chips were evacuated under the pressure of 70 µmHg for 10 minutes. The non-wetting mercury, as the working probe for pore access, follows the parameters: Hg density of 13.53 g/mL; adv. and rec. contact angle of 130^o ; Hg surface tension of 485 dynes/cm. The mercury filling pressure was performed of 0.51 psia under 10 seconds for equilibration, followed by injection under high pressure, ranging from 0.1 MPa (14.5 psi) to a maximum 413.7 MPa (60,000 psi), which corresponds to the pore throat size from 3.6 nm to 1100 µm.

The pore throat size distribution of tested samples is obtained using Washburn equation assuming cylindrical pores (Equation 2) (Washburn 1921):

$$r_i = \frac{-2\sigma \cos\theta}{P_c} \text{.....(3.2)}$$

where r_i is the pore throat radius calculated under mercury pressure of P_c (psi), µm; σ is the mercury surface tension (485 dynes/cm applied in the test); θ is mercury contact angle (130^o applied in the test) ; p_c is the injection pressure ranging from 14.5 psi to the maximum 60,000 psi.

3.3. Results

3.3.1. Porosity obtained from NMR, MICP and Helium porosimetry

The porosity values obtained from three measuring techniques (i.e., MICP, Helium, and NMR) are shown for two different shale formations (i.e., Carynginia and Monterey) (**Table 3. 2**). An obvious porosity distinction is displayed in NMR between the clay-rich samples (i.e., Carynginia) and the clay-poor samples (i.e., Monterey). An overall higher NMR porosity are exhibited in Carynginia compared to Monterey. In addition, the porosity discrepancies are apparently exhibited between NMR and the other two measurements in Carynginia samples.

Carynginia presents the highest porosity value in NMR, which is more than two times as MICP porosity, and about three times as helium porosity (i.e., the porosity measured by NMR, helium, and MICP ranges in 8.02-12.87 %, 3.03- 3.78 %, and 1.93-4.15 %, respectively). However, the Monterey exhibits a high porosity consistency in NMR, helium and MICP (**Figure 3. 1**). The porosity measured from MICP and helium demonstrates high consistencies in both Carynginia and Monterey. As shown in **Figure 3. 2**, the cross-plot of helium porosity versus MICP porosity generates a very good positive linear relationship, with the correlation coefficient (R^2) of 0.93.

Table 3. 2 The porosity values obtained from MICP, Helium and NMR techniques for the studied samples in Carynginia and Monterey. Some data are collected from other studies (Yuan et al. 2018c, Rivera and Prasad 2014, Al Hinai et al. 2014).

Name	Formation	Depth (m)	MICP Φ, %	Helium Φ, %	NMR Φ, %
AC1	Carynginia	2780.2	3.78	2.78	10.06
AC2	Carynginia	2781.7	3.05	4.15	10.04
AC3	Carynginia	2789.9	3.17	1.93	11.05
AC4	Carynginia	2794.4	3.54	3.11	10.66
AC5	Carynginia	2806.4	3.56	3.22	12.87
AC8	Carynginia	2825.3	3.03	2.92	8.02
M1-B	Monterey	1633.7	N/A	11.0	11.0
M2-B	Monterey	1658.1	N/A	13.0	14.0
M3-B	Monterey	2409.7	N/A	6.0	6.0
M4-B	Monterey	2539.9	N/A	2.0	1.0
M5-B	Monterey	2602.7	3.4	2.0	2.0
M6-B	Monterey	2631.0	2.8	2.0	3.0
M7-B	Monterey	2723.4	1.1	1.0	2.0
M8-B	Monterey	2772.8	N/A	1.0	3.0
M9-B	Monterey	2802.0	0.7	2.0	4.0
M10-B	Monterey	2879.4	N/A	1.0	2.0
M1	Monterey	1669.5	4.7	4.0	7.0
M2	Monterey	2200.9	N/A	5.0	6.0
M3	Monterey	2203.2	3.8	6.0	6.0
M4	Monterey	2362.4	8.4	5.0	8.0
M5	Monterey	2362.7	21.9	20.0	16.0

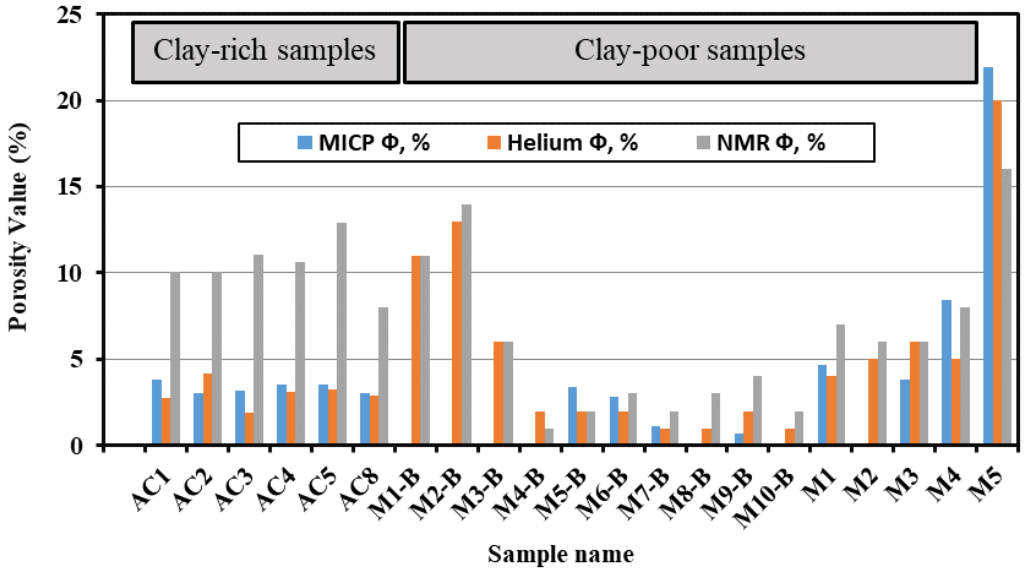

Figure 3. 1 The porosity values obtained from mercury intrusion capillary pressure (MICP), Helium, and nuclear magnetic resonance (NMR) for two different shale formations.

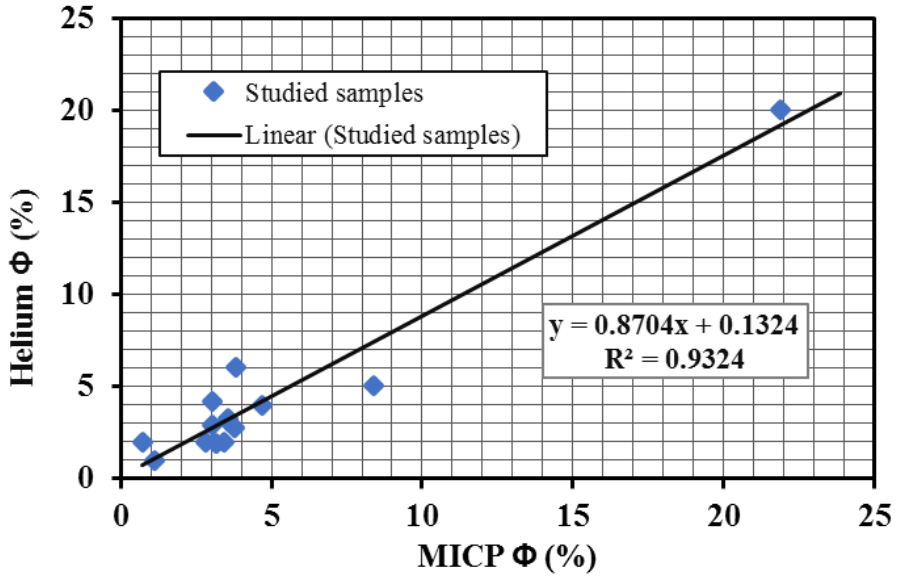

Figure 3. 2 The cross-plot of Helium porosity (%) versus MICP porosity (%) for the studied samples.

3.3.2. Pore size distribution obtained from NMR

Figure 3. 3 presents the NMR T_2 spectrum in Carynginia shales, with the majority of pores identified in small pore sizes. The peak values of T_2 curves correspond to the T_2 relaxation time around 0.3-1 ms. The samples of higher clay contents, e.g., AC1 and AC2 (i.e., 50.8 % and 43.2 %), exhibit larger amplitude and narrower spectrum with the peak value locating in

smaller pore sizes. The samples of relatively lower clay contents, e.g., AC8 and AC4 (i.e., 32.3 % and 31.1 %), display smaller amplitude and wider distributions, presenting a general larger pore sizes. A uniform pore size distribution is commonly indicated in Carynginia shales.

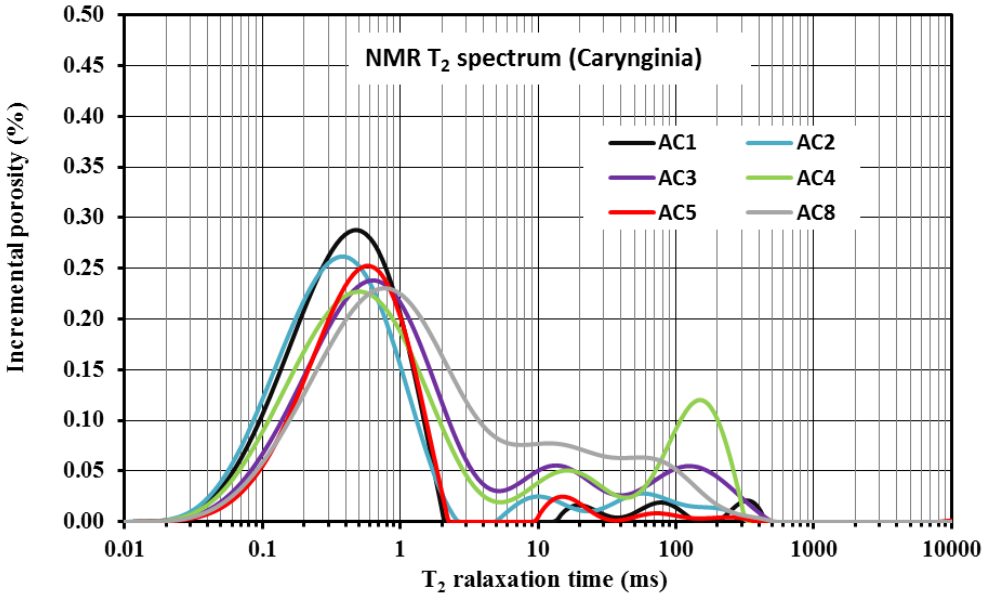

Figure 3. 3 NMR T_2 spectrum for Carynginia shales (i.e., AC1-AC8).

NMR T_2 spectra of Monterey shales, i.e., M1-M6 and M1-B-M10-B, are displayed in **Figure 3. 4** and **Error! Reference source not found.**, respectively. Significant variations are demonstrated in Monterey shales compared to Carynginia shales. As shown in **Error! R eference source not found.**, Monterey shales from Well 1 (except for M5) exhibit the major pores in larger pore size ranges. The peak locations of the spectrum correspond to T_2 relaxation time ~ 1-100 ms, coupled with an overall wider spectrum range, indicating a general uneven pore size distributions. The peak values (except for M5) correspond to the incremental porosity between 0.1 % and 0.13 %, displaying overall lower values than that in Carynginia shales. M5 shows the trimodal spectrum associated with three typical pore types. The spectrum peak of M5 occurs at T_2 relaxation time in 300-500 ms, representing the majority of larger pores or fractures.

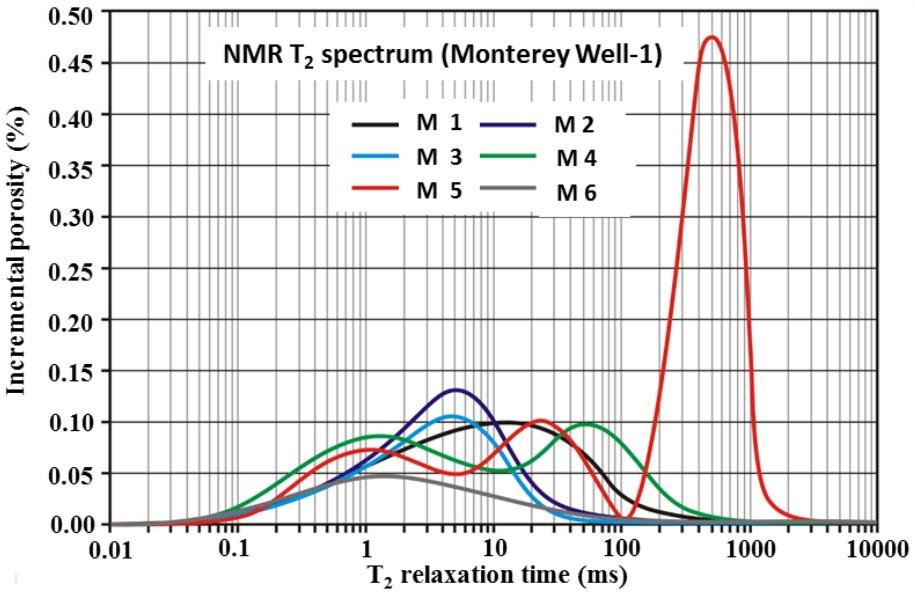

Figure 3. 4 NMR T_2 spectrum for Monterey shales (i.e., M1-M6) collected from Well 1. Modified from Rivera (2014).

Error! Reference source not found. shows the T_2 spectrum of Monterey shales from Well 1 B with multiple modal types. M4-B, M10-B, M7-B, M9-B exhibit a majority of small pore sizes, corresponding to the T_2 relaxation times of ~ 0.3-1 ms. M1-B and M2-B with semi-modal distributions present the PSD peaks at larger T_2 relaxation time (i.e., 14 ms and 40 ms respectively) and higher incremental porosity (i.e., 0.27 % and 0.36 % respectively). M3-B exhibits trimodal spectrum with the main pore size locates at ~ 20ms. When compared to T_2 spectrum in clay-rich Carynginia, the pore sizes in Monterey are rather unevenly distributed and universally locating in larger pore sizes. Moreover, unlike Carynginia, no obvious correlations are observed between the clay contents and the NMR PSD amplitudes in Monterey shales.

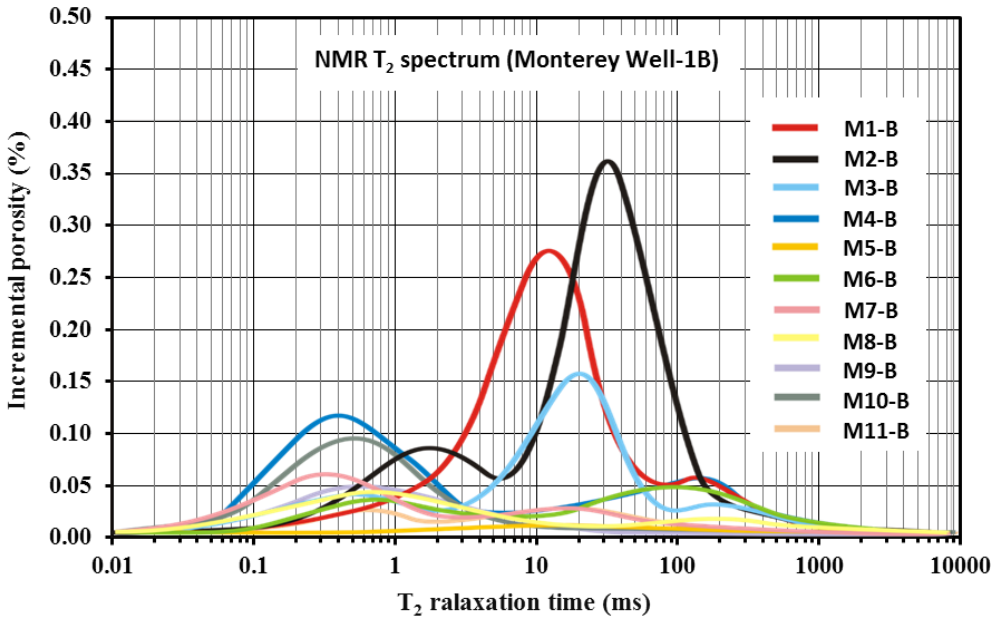

Figure 3. 5 NMR T_2 spectrum for Monterey shales (i.e., M1-B-M6-B) collected from Well 1B. Modified from Rivera (2014).

3.3.3. Pore size distribution obtained from gas adsorption

Figure 3. 6 displays Caryngina PSD obtained from LP-N_2-GA experiments. As can be seen, the PSD peak in Carynginia appears around 20 nm, implying the pore majority locating in fine mesopore sizes that dominantly controls the total pore volume. Monterey shales, by contrast, present a different scenario (**Figure 3. 7**), showing PSD peak at ~50-100 nm with the pore majority in fine macropore ranges, which is intimately related to the high quartz content.

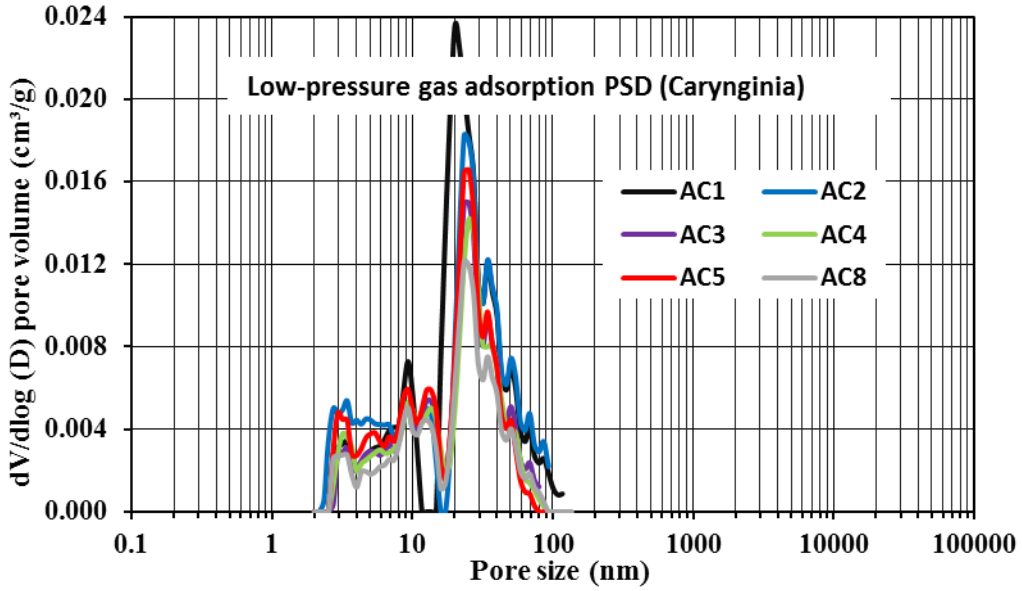

Figure 3. 6 Carynginia pore size distribution (PSD) derived from low-pressure N_2 gas adsorption based on BJH theory.

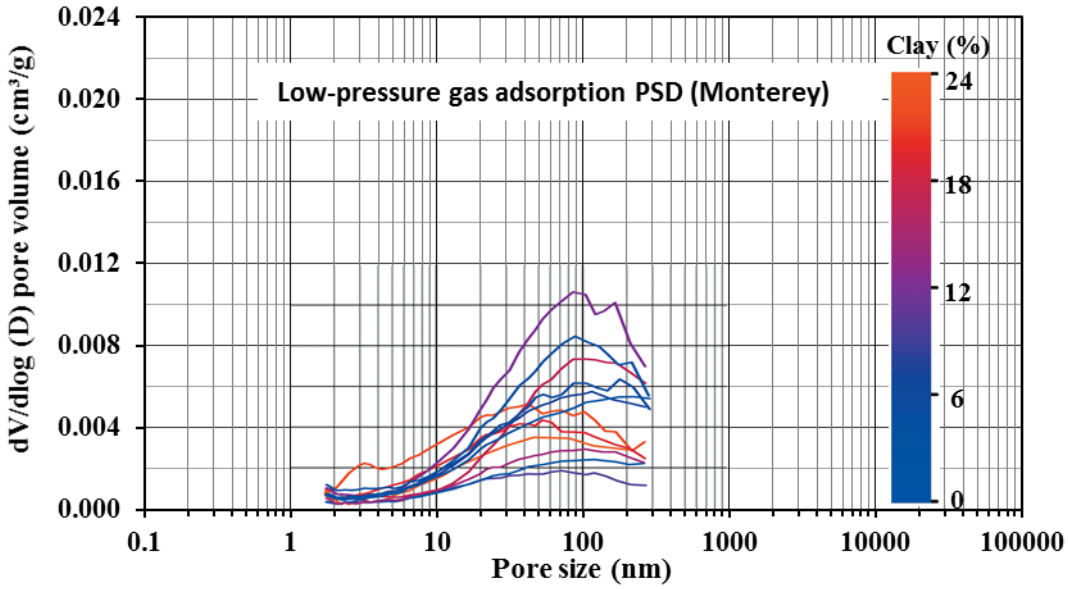

Figure 3. 7 Monterey pore size distribution (PSD) derived from low-pressure N_2 gas adsorption. Modified from Saidian et al. (2016).

3.3.4. Pore throat size distribution obtained from MICP

Carynginia and Monterey pore throat size distributions (PTDs) measured by MICP are plotted in **Figure 3. 8** and **Figure 3. 9**. The peaks of MICP- derived PTD in Carynginia are commonly located in pore sizes ~ 4-5 nm, which are smaller compared to that interpreted by LP-N_2-GA. A wider range of the detectable large pores (i.e., pore sizes larger than 100 nm) is revealed by MICP technique compared to LP-N_2-GA. Consistent with the NMR and LP-N_2-GA interpretations for Carynginia samples, larger PTD amplitude is shown in the samples of higher clay (e.g., AC1, AC2), while the lowest PTD amplitude is found in samples of the lowest clay samples (i.e., AC8). The Monterey PTD, however, presents a weak interrelationship between the clay content and the amplitude of curve (**Figure 3. 9**), which agrees with the behaviours of Monterey PSD (e.g., **Figure 3. 4**, **Figure 3. 5**, **Figure 3. 7**) that is most likely under the large influences of low-clay contents (Saidian et al. 2016).

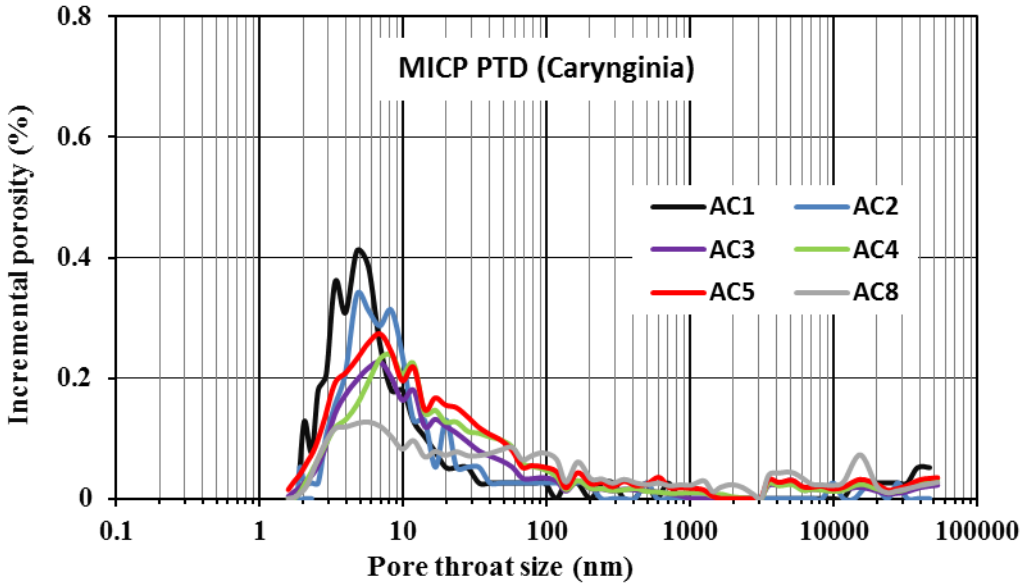

Figure 3. 8 MICP pore throat size distribution (PTD) for Permian Carynginia shales.

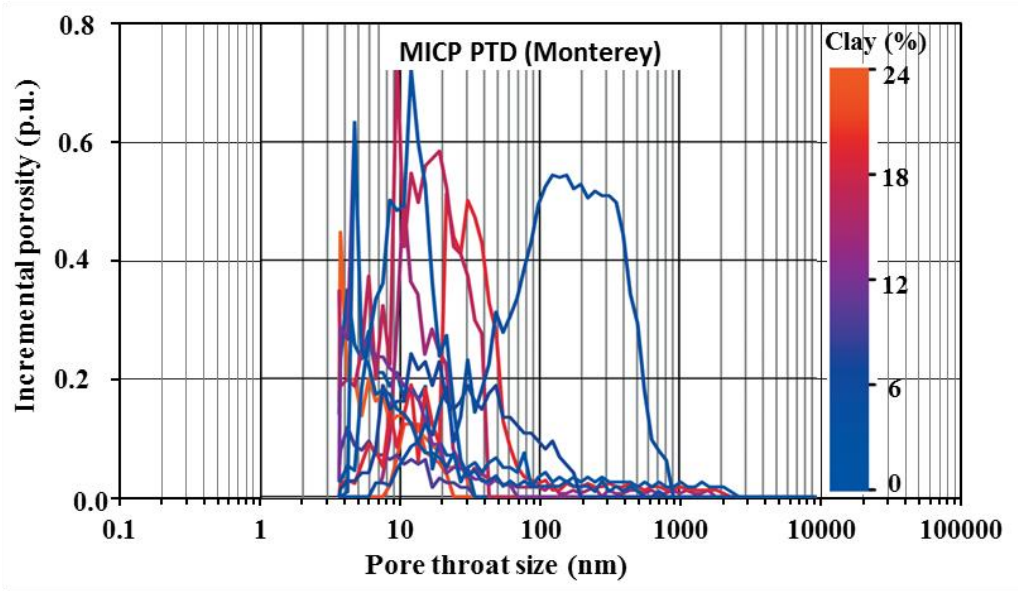

Figure 3. 9 MICP pore throat size distribution (PTD) for Monterey shales. Modified from Saidian et al. (2016).

3.4. Discussion

Carynginia samples are characterized by abundant clay contents, while Monterey shales are clay-poor (**Table 3. 1**). NMR technique, which is highlighted by non-destructive measurement of total porosity, involves the detection of effective porosity and clay bound water (CBW), which is tightly bound on the surface area of clay minerals and universally quantified by cutting

the effective porosity off total porosity (Prammer et al. 1996, Coates et al. 1998). Other penetration approaches, e.g., helium, MICP, and low-pressure gas adsorption, nevertheless, are merely approachable to the inter-connected pores, missing out the closed-pores or the ineffective porosity occupied by CBW. Under extreme circumstances, for shales containing very high clay contents and thus high CBW, the most of pore spaces could be nearly fully-occupied by the volume of CBW (Clavier et al. 1984, Topór et al. 2016) that would influence the petrophysical properties in shales (Yuan et al. 2018c, Yuan and Rezaee 2019c, Tan et al. 2015, Yuan et al. 2018a). As helium porosimetry is able to obtain effective porosity by covering a wider pore size range (i.e., 0.1 nm- 100 μm) than MICP (i.e., 3.6 nm -100 μm) (**Figure 3. 10**) (Caineng et al. 2016), the CBW is calculated by subtracting the helium porosity (i.e., effective effective) from NMR porosity (i.e, total porosity). **Figure 3. 11** cross-plots the calculated CBW versus the clay content in both Carynginia and Monterey shales. The CBW, which accounts for the porosity discrepancy between NMR and helium measurement, displays higher values in clay-rich Caryngnia shales, but lower values are found in Monterey shales. The correlation presents a good linear relationship (R^2 = 0.76), indicating that the correlation equation (Equation 3) is adaptable for the estimation of CBW in the shale, whose clay type is dominantly contributed by illite:

$$CBW\ (\%) = 0.19\ \times V_{sh}\ (\%) - 0.7 \ldots\ldots\ldots\ldots (3.3)$$

where CBW is the volume of clay bound water (%), V_{sh} (%) is the clay contents (%). Moreover, the equation is most likely to fit into the formation with the brine salinity of 20000-30000 ppm that matches with our studied formations.

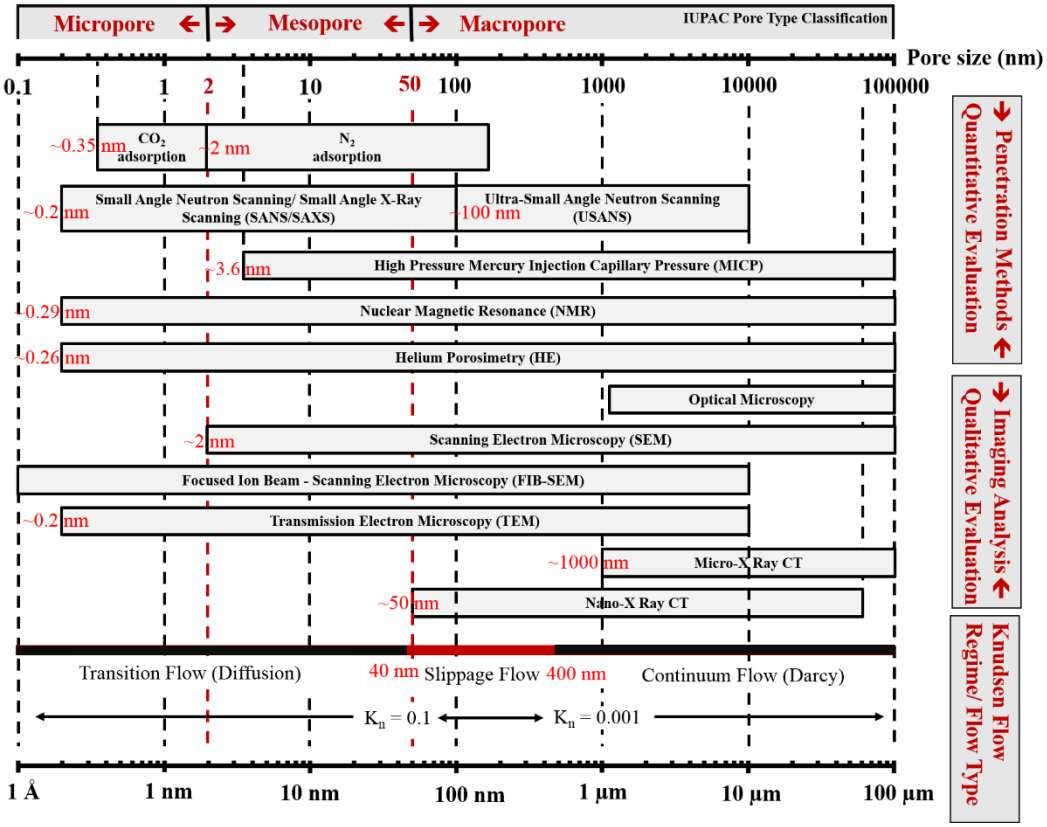

Figure 3. 10 The multi-scaled methods for pore characterization in shales modified from other studies (Bustin et al. 2008, Caineng et al. 2016, Sondergeld et al. 2010b, Busch et al. 2016).

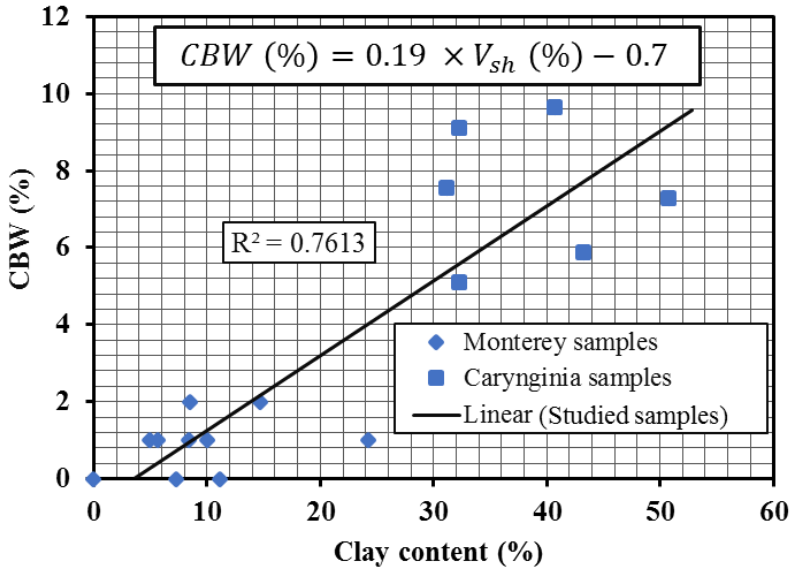

Figure 3. 11 The cross-plot of clay bound water (CBW) (%) versus clay content (%) for studied shale samples.

Apart from the influencing factors associated with clays, the compatibility of the penetrated working fluid molecules with shale nanopore structure also causes the interpretation inconsistencies. Unlike NMR using H_2O as working fluid to access pore body, the working molecule involved in MICP is merely attainable to the limited pore throat size. The mineral-controlled geometrical pore shapes, which are highly intimated with the mineral compositions and assemblages, pose a large impact on the porosity discrepancies between NMR and MICP in Carynginia shales (Yuan and Rezaee 2019d). To summarize, the possible reasons for the higher NMR porosity over MICP are: (1) the volume of clay bound water; (2) the porosity contributed by pores smaller than 3.6 nm; (3) the different mechanisms involved in NMR pore body detection versus MICP pore throat detection (e.g., MICP assumes the pores are cylindrical in shape with a smooth surface, but the real pores are complicated with rough surfaces bound with water layers) (Caineng et al. 2016); (4) the pore shape combination that intimately related to shale compositions. When the comparisons are carried out between helium and MICP, theoretically, for shales containing high proportion of micropores, helium porosity is supposed to be higher than MICP due to its wider detection of pore size range (Bustin et al. 2008). However, the higher MICP porosity values are observed in some of the studied samples in both Carynginia and Monterey (e.g., AC1, AC3, M5-B, M4) (Error! Reference source not found.). A s the samples from both formations show a small proportion of micropores, the possible reasons could be explained by the increased mercury uptake induced by the high pressure application (i.e., 60,000 psi) in MICP measurement (Suuberg et al. 1995). Similar phenomenon have also been found in coals (Yao and Liu 2012), which possess similar characteristics as shales (Mastalerz et al. 2012, Mastalerz et al. 2018).

3.5. Conclusions

The discrepancies in porosity or pore size distribution between MICP, NMR, and LP-GA porosimetry are largely controlled by shale compositions, particularly, the clay minerals. The clay-rich shales generate NMR porosity significantly higher than MICP and helium porosity, while the clay-poor shales exhibit a high porosity consistency between NMR, MICP and helium porosimetry.

The higher porosity values unveiled by NMR over MICP/ helium technique are fundamentally attributed to CBW, meanwhile, the clay mineral compositions and assemblages, coupled with pore geometry also contribute to the discrepancies. The MICP and helium both detects intercommunicated pores and display consistent porosity for shales deficient in pores smaller than 3.6 nm. The shales of deficient micropores may possibly show higher helium

porosity over MICP porosity, which essentially result from the high pressure application involved in MICP technique.

CHAPTER 4 Pore characterization and the assessment of clay bound water impact on effective porosity

This chapter is a published peer-reviewed journal paper in *International Journal of Coal Geology*:

Yuan, Y., Rezaee, R., Verrall, M., Hu, S.-Y., Zou, J., and Testmanti, N., 2018, Pore characterization and clay bound water assessment in shale with a combination of NMR and low-pressure nitrogen gas adsorption: International Journal of Coal Geology, v. 194, p. 11-21.

4.1. Introduction

Gas shale is a promising resource for hydrocarbon production in recent decades (Ross and Bustin 2008, Jarvie et al. 2007, Bowker 2007). The commercial success of shale gas production in the United States remarkably shaped the global energy-supply market (Curtis 2002), raising great interests in fundamental investigations on shale petrophysical properties, such as permeability, effective porosity and irreducible bound water, which can be used to estimate hydrocarbon storage capacity (Furmann et al. 2016, Labani et al. 2013, Rezaee 2015). Clay-bound water (CBW), defined by Schlumberger as the electrochemically bound water within clay lattice or near pore surface within electrical double layer, is residing in nanometer-scaled pore structures. CBW is the most key petrophysical parameter and commonly used to calibrate log porosity for shale formation evaluation (Coates et al. 1999).

Low-field nuclear magnetic resonance (LF-NMR) has been widely used for pore structure characterization and CBW investigation (Prammer et al. 1996, Tinni et al. 2017, Coates et al. 1999, Saidian and Prasad 2015). Commonly, NMR technique is used in conventional reservoirs to quantify the bulk volume of moveable fluids and the irreducible bound fluids (i.e., CBW and capillary bound water) in pore spaces (Dunn et al. 2002). The essential NMR data for pore fluid characterization is referred to as transverse relaxation (T_2) distribution, on which the threshold T_2 value (T_2 cutoff) is established to differentiate fluid types for petrophysical analysis (Coates et al. 1999). Typically, the value of 33 ms was utilized for sandstones to separate irreducible bound volume from movable volume (Straley et al. 1997), while larger values were suggested for carbonate due to the weaker surface relaxivity. For example, 92 ms had been raised for Glorieta and Cleat-fork carbonates in West Texas (Chang et al. 1994), while 100 ms were

documented by Straley et al. (1997). In particular, the T_2 cutoff between CBW and capillary bound water was identified as 3 ms in sandstone (Prammer et al. 1996), while T_2 cutoff for CBW quantification in shale has not yet been systematically established. Traditionally, lab determination of T_2 cutoff is performed on core plugs in two conditions, i.e., S_w=100% (brine saturated condition) and S_{ir}=irreducible (residual brine condition after centrifuging). However, the conventional approach using centrifuge for fluid partition in sandstone, carbonate and coal (Straley et al. 1997, Kenyon 1992, Freedman 2006, Yao and Liu 2012, Xiao et al. 2018, Zhang et al. 2018) is not applicable for shales in Permian Carynginia formation, due to the fragile texture and the complex pore structure. The rotational centrifuge speed over 4500 rpm, which has achieved to the maximum capillary pressure of 315 psi (2.17 MPa), would destroy shale samples. Meanwhile, little water has been extracted by centrifuging at the maximum 4500 rpm.

Recent research by Testamanti and Rezaee (2017) developed the traditional centrifuging method by oven-heating the samples to differentiate pore water, which provides an efficient approach to further extract movable pore water in Permian Carynginia shale. However, during the experiments, we found an abnormal rise in NMR pore size distribution (PSD) from 80°C to 90°C, which has been ignored in previous study. This newly-observed abnormal phenomenon we are discussing in this study indicates a remarkable petrophysical variation during heating, which is significant for CBW quantification and and would result in completely different conclusions, therefore, should be fully addressed in gas shale formation evaluation. As nanopore structure in shale, together with CBW of smectite, is reported to be sensitive towards temperature (Handwerger et al. 2011), the anomalous behaviour exactly needs to be re-examined. Furthermore, as mineral conversion, which was documented to largely affect pore structure, has been suggested to occur between 58°C and 92°C (Freed and Peacor 1989), the temperature around 80°C is likely to be a critical implication for CBW determination in shale formation. Above all, the novelty of PSD anomaly above 80°C, which has been detected by NMR, requires re-examination by another method and the cause of the anomaly needs to be fully understood to better characterize pore structure and CBW in Permian Carynginia shales.

To characterize tight shale pore structure in small scales, fluid penetration approaches have typically been documented in literature (Clarkson et al. 2013, Liu et al. 2017). Nevertheless, molecular size of working fluids would influence the pore size accessibility due to the widespread pore size range and the extremely tight texture in shale (Mastalerz et al. 2013). Understandings of kinetic diameter (D) of working fluids are thus essential for accurate petrophysical property characterization in shale (Sondergeld et al. 2010b). The common used

high-pressure mercury intrusion, for example, is not only destructive to samples (Yao and Liu 2012), but unable to access either pore throats below 3.6 nm or pore bodies in shales (Mastalerz et al. 2013, Nelson 2009). Whereas by contrast, water molecules, which are used in LF-NMR, present the advantage of small molecular size (D=0.278 nm, Bondi (1964)) to access nanopores, thus has been widely used for measuring total porosity and PSD (Coates et al. 1999). Meanwhile, nitrogen molecules, with similar Van der Walls diameter (D=0.310 nm) as water molecules, are able to enter the smaller pore size of 2nm (Sondergeld et al. 2010b). The low-pressure (<18.4 psi) nitrogen gas adsorption (LP-N_2-GA) approach, which uses nitrogen as the fluid probe, is another useful approach to characterize small-scaled PSD in shale (Clarkson et al. 2012b). Meanwhile, shale samples for LP-N_2-GA test are vacuum dewatered under the pre-set heating temperature, which is comparable to the heating pre-treatment in NMR measurement. Further, more pore structure properties (i.e., pore volume, specific surface area) are provided by LP-N_2-GA to analyze the impact of temperature on pore properties.

The purpose of this paper is to find the critical temperature to discriminate CBW from movable pore water in Permian Carynginia shale. LP-N_2-GA test combined with NMR experiment is performed and compared to further investigate the extraction behavior of pore water in complex pore networks during thermal dehydration.

4.2. Materials and methods

4.2.1. Geological setting

Geographically, Perth Basin (**Figure 4. 1**), with an elongated trending in North-South direction, is located in western coast of Australia (Departments of Mines and Petroleum 2015). Covering a total area around 172,300 km^2, Perth Basin contains the components of onshore sedimentary and offshore continental shelf, from Yigarn Craton in the east to the Indian Ocean continental crust to the west. As shown in **Figure 4. 1**, tectonically, Perth basin is controlled by the onshore Darling Fault and Dandaragan Trough in the east, the Beagle Ridge area in the middle, and the offshore Abrohols Sub-basin and Vlaming Sub-basin in the west (Thomas 2014). Some very quick estimation shows that Perth Basin holds approximately 33 Tcf (926 Gm^3) recoverable shale gas (U.S. Energy Information Administration 2015) and up to 155 Tcf (4389 Gm^3) risked shale gas-in-place. However, although Perth Basin has sediments that were deposited from Ordovician age to the recent, geochemically, the stratigraphic interval of hydrocarbon interest is mainly located between Lower Permian and Middle Triassic age (Thomas and Barber 2004).

Our study area, Carynginia Formation, is geologically located in onshore Northern Perth Basin as a stratigraphical unit of early Permian age. Initial well testing results identified Carynginia Formation as one of the top three prospective formations in the Northern Perth Basin for further evaluation (Bahar M. 2011).

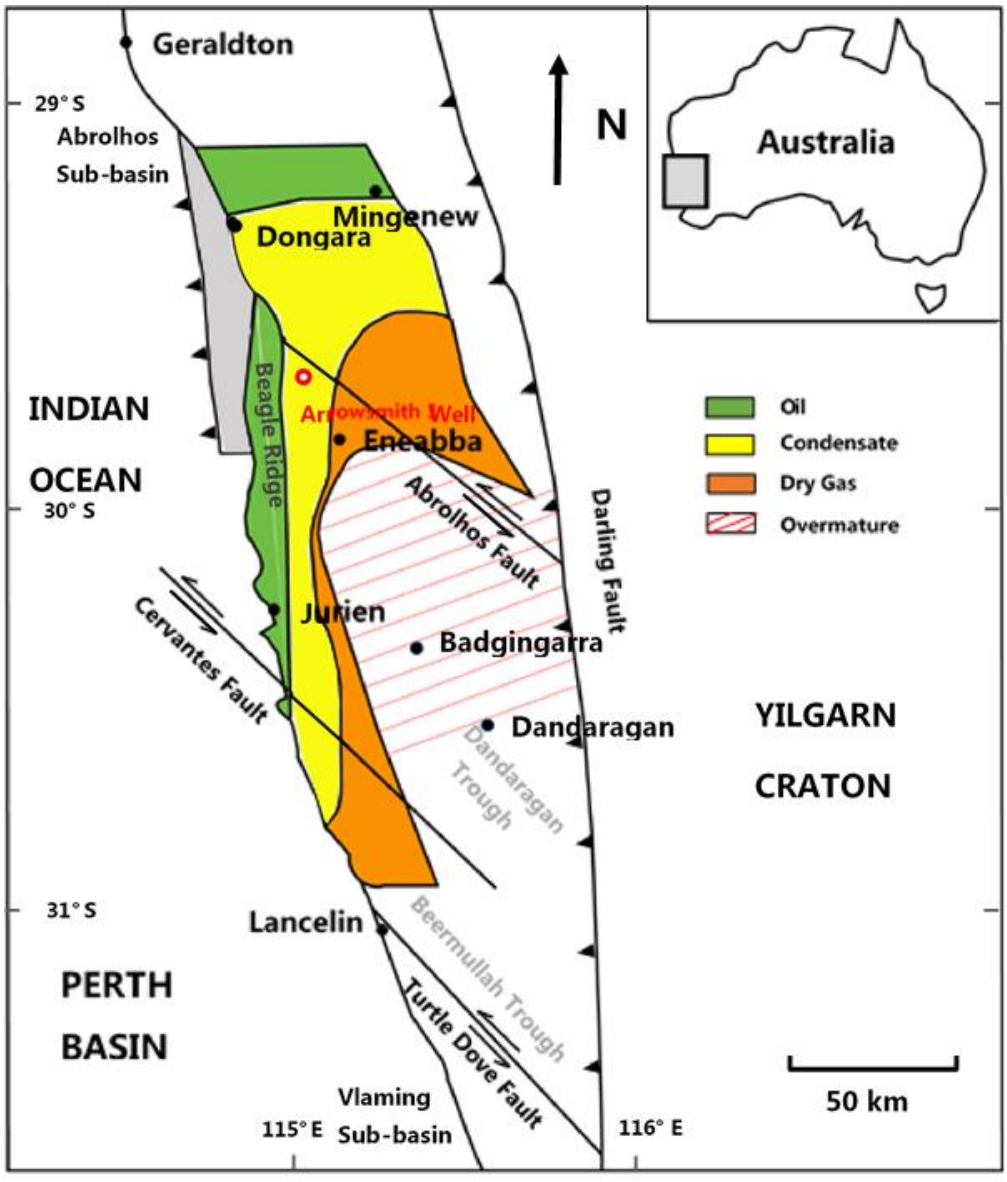

Figure 4. 1 Geological map of the Carynginia Formation in Perth Basin, Western Australia *(modified from Western Australia's Petroleum and Geothermal Explorer's Guide, 2014 Edition)*

4.2.2. Samples

In this study, a total of seven shale samples were collected from Permian Carynginia Formation via Northwest Energy's Arrowsmith well. The location of Arrowsmith well is shown in **Figure 4. 1**. Our tested samples were selected in various depth (**Table 4. 1**), taking into considerations of the variation in clay mineral content for CBW investigation. Each sample was trimmed into several pieces for different measurements. X-ray diffraction (XRD) were performed for mineralogical characterization. **Table 4. 1** presents the dominant content of quartz and clays (i.e., illite/ muscovite, chlorite, kaolinite and smectite). Among all the clay minerals, the mixed illite and illite/muscovite predominantly contribute to 76.15-82.32 wt.% of the total clay, while chlorite, kaolinite and minor smectite account for 9.97-17.07 wt.%, 1.79-11.41 wt.% and 1.77-6.02 wt.%, respectively.

Table 4. 1 XRD mineralogical composition (wt. %) of Carynginia Permian shale, Perth Basin, WA.

Name	Depth (m)	Quartz (wt. %)	Smectite (wt. %)	Mixed illite/smectite (wt. %)	Illite/ muscovite (wt. %)	Chlorite (wt. %)	Kaolinite (wt. %)	Other minerals (wt. %)
AC1	2780.2	35.6	0.9	25.8	13.1	5.8	5.2	13.6
AC2	2781.7	40.3	0.8	22.9	10.0	4.9	4.6	16.5
AC4	2794.4	53.0	1.6	11.7	13.9	3.1	0.8	13.8
AC5	2806.4	41.3	0.9	14.9	18.9	5.2	0.8	15.2
AC7	2816.7	49.2	1.7	12.4	14.3	4.8	0.9	16.7
AC8	2825.3	53.2	1.2	19.0	7.7	2.7	1.8	14.4
AC9	2831.3	44.5	1.9	9.7	16.0	4.3	1.2	15.9

4.2.3. Low-field NMR Measurement

LF-NMR was performed on 2MHz Magritek Rock Core Analyzer with shale core plugs. All the seven plug samples with a diameter of 1.5" were cleaned with toluene and saturated with KCl brine water under 2000psi until constant weight has been reached. NMR T_2 spectrum were measured using Carr, Purcell, Meilboom and Gill pluse sequence (Kenyon et al. 1995, Carr and Purcell 1954, Meiboom and Gill 1958), with 100 μs inter-echo spacing (TE), 10000 ms inter-experiment delay, and 10000 number of echoes and the minimum 200 signal to noise ratio (SNR). The initial 1st round NMR measurements were performed on the fully saturated core plugs, followed by centrifuging at 4500 rpm under 315 psi for 26h. Core plugs were then subjected to the 2nd round NMR test, followed by vacuum oven dehydration under the pre-set heating temperatures. Core plugs were weighted every 1 hour until no further reduction could be observed, followed by cooling down in a sealed vessel to room temperature for the 3rd

running of T_2 experiments under separate temperatures. The heating scheme followed the temperature ranges from 50°C to 120°C.

LF-NMR primarily functions by activating and responding to hydrogen proton in pore fluid of reservoir rock. Similar to microscopic magnets orienting in magnetic fields, hydrogen proton will respond align with the external magnetic field. The T_2 relaxation time is identified once magnetic field withdraws, T_2 distribution can be obtained and converted into pore size distribution for interpretation of complex pore structures (Freedman 2006, Freedman and Heaton 2004, Kenyon et al. 1995, Yu et al. 2017). Theoretically, three independent relaxation mechanisms of fluids are included in reservoir rocks: bulk relaxation, diffusion relaxation and surface relaxation, while bulk and diffusion relaxation are negligible for the homogeneous magnetic field with short TE. T_2 relaxation could be simplified as **Eq. (4.1)** (Coates et al. 1999, Yao et al. 2010).

$$\frac{1}{T_{2\,\text{surface}}} = \rho\left(\frac{S}{V}\right)_{pore} \quad \ldots\ldots\ldots\ldots (4.1)$$

where $T_{2\,\text{surface}}$ is the relaxation time of the residing fluids resulting from surface relaxation; ρ is the T_2 surface relaxivity; $\frac{S}{V}$ is the ratio of surface area to pore volume. A proportional relationship is revealed between T_2 relaxation time and pore size distribution from **Eq. (4.1)**, which indicates that the shorter T_2 relaxation time is consistent with smaller pores, while longer T_2 relaxation time corresponds to larger pores. As core plugs were cleaned with toluene, it is reasonable to consider that LF-NMR response is from the remaining water stored in complex pore structures (Handwerger et al. 2011).

4.2.4. Low-pressure N_2 gas adsorption measurement

Prior to loading samples for LP-N_2-GA test, shale samples were crushed and sieved into 60-mesh-size (<250 μm) fragments, which is larger than shale grain size (62.5μm) to preserve the entire shale microstructures (Rezaee 2015). The smashed samples with increased exposing surface area make it possible to speed up extraction, drying and gas equilibrium, particularly for shale of nano-permeability and low porosity properties (Luffel and Guidry 1992), while no further porosity could be generated due to the nanometer-sized pore scales in shale (Spears et al. 2011).

Initial normalization was performed on samples as per equilibrium moisture standards (Krooss et al. 2002), followed by vacuum dewatering and outgassing for more than 8h. Since 40°C has been suggested in LP-N_2-GA for shales as an initial temperature, above which the

boiling point of water near experimental vacuum conditions is achieved to evaporate free water in macropores or micro-fractures (Heller and Zoback 2014, Wang and Ju 2015, Zolfaghari and Dehghanpour 2015), we conducted various dewatering temperatures ranging from 40°C to 120°C. LP-N_2-GA measurement was performed on Micromeritics® TriStar instrument, which is employed to collect and quantify the adsorbed gas volume as the relative pressure (P/P_0) keeps increasing. Note that P represents the gas vapor, P_0 represents the saturation pressure of the adsorbent. PSD and specific surface area (SSA) were eventually interpreted by converting isotherm adsorption branch using density functional theory (DFT) molecular model (Seaton and Walton 1989, Lastoskie et al. 1993) and Brunauer-Emmett-Teller (BET) model (Barrett et al. 1951), respectively.

4.3. Results and discussion

4.3.1. Characterization of pore structure and water extraction behaviour

4.3.1.1 Analysis of NMR

NMR T_2 spectrum in AC1, AC2 and AC5 are presented at various temperatures in **Figure 4. 2**. As similar trends have shown in all of the seven samples, AC1, AC2, and AC5 were selected as examples for presenting and discussing in this study. As indicated in **Figure 4. 2**, typical unimodal T_2 distributions are found with peak value around 0.5ms, while the predominant T_2 distribution ranges from 0.1ms to 1ms, indicating the major distribution of small pores in Permian Carynginia shale. In contrary to the wide spectrum range below 5ms, isolated small peaks are observed above 5ms, suggesting the development of disconnected pores or micro-fractures in larger pore scales.

To clearly characterize PSD, NMR spectrum was transformed via surface relaxivity (ρ). The surface relaxivity was calculated by correlating NMR T_2 spectrum with the PSD obtained from LP-N_2-GA. As pore surface area (S) and pore volume (V) can be measured by LP-N_2-GA, surface relaxivity for shale samples in Permian Carynginia formation was determined in the ange of 0.05-1.26 μm/s based on **Eq. (4.1)**. Additionally, $T_{2\,surface}$ could be expressed as **Eq. (4.2)** (Yao et al. 2010, Saidian and Prasad 2015):

$$\frac{1}{T_{2\,\text{surface}}} = \rho\left(\frac{C_s}{r_i}\right) \quad \ldots\ldots\ldots\ldots \quad (4.2)$$

where C_s is a constant, which is equal to 1, 2, 3, respectively for plane, cylindrical and spherical pores; r_i is the pore size. As pore shape of the tested samples was identified as plane based on LP-N_2-GA (Labani et al. 2013), the value of 1 is selected. By employing the calculated surface

relaxivities into **Eq. (4.2)**, PSDs (**Figure 4. 3**) were correspondingly transformed from T_2 distributions. As illustrated in **Figure 4. 3** the peak value of fully saturated curve is identified around 26.2 nm, 24.8 nm and 25.9 nm for AC1, AC2 and AC5 respectively, which demonstrates that the major pore size ranges at approximately 25nm. Under the heating scheme, as temperature rise, pore water was increasingly removed from pore structure, leaving fewer hydrogen protons residing in small pores, which is indicated by the continuous shrinkage of T_2 spectra in **Figure 4. 2**. A strikingly low cumulative porosity is presented at 80°C (i.e., 2.62% for AC1; 2.60% for AC2; 1.64% for AC5), compared to the highest cumulative porosity at initial condition (i.e., 10.06% for AC1; 10.04% for AC2; 8.02% for AC5). An anomalously converse increase of detected porosity is observed at 90°C, showing the cumulative porosity of 3.25%, 2.77% and 2.23% for AC1, AC2, AC5, respectively (**Figure 4. 2a,c,e**). A stable region between 90-120°C was followed, with no big differences presenting in cumulative porosity (**Figure 4. 2b,d,f**).

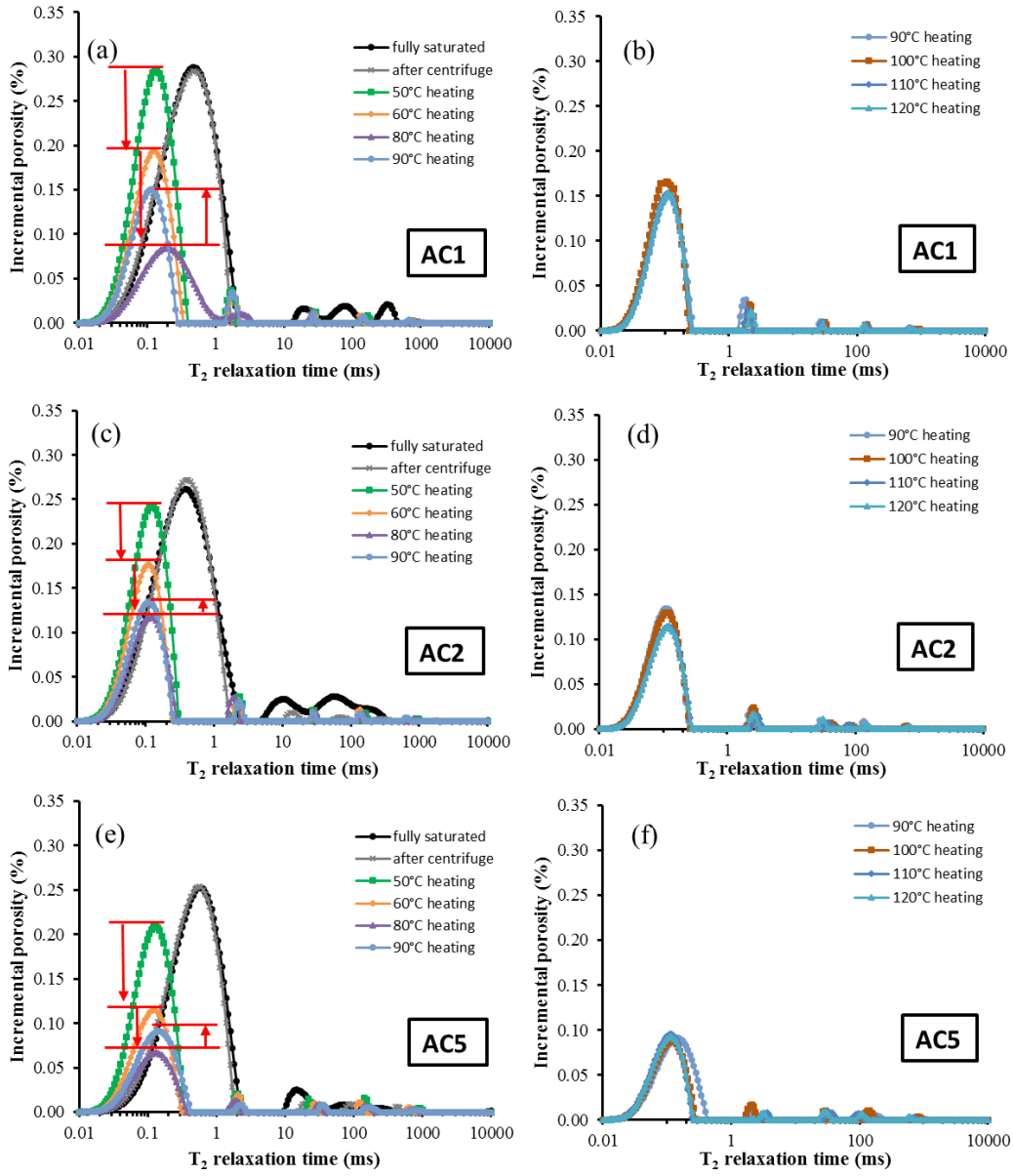

Figure 4. 2 NMR T_2 distribution of Permian Carynginia shales after saturating, centrifuging and dehydration heating procedures. Some data were previously published by Testamanti and Rezaee (2017).

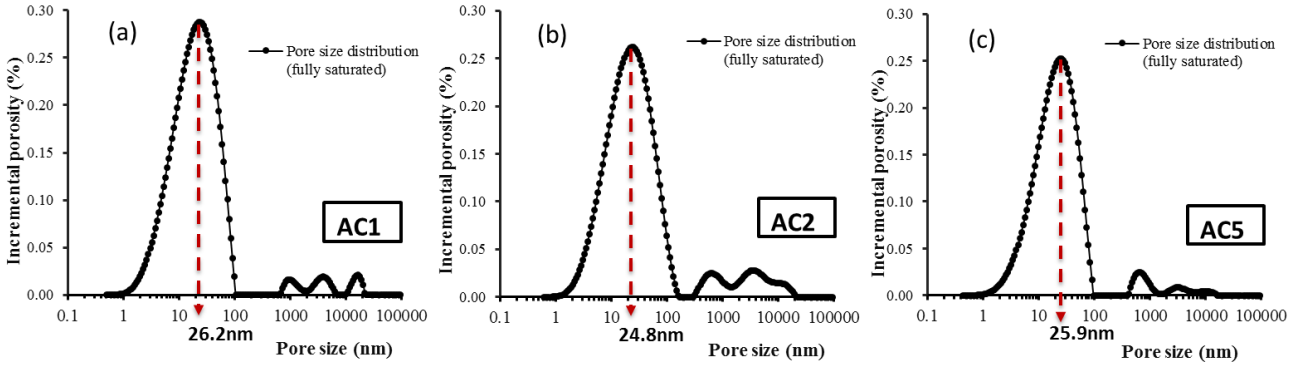

Figure 4. 3 Pore size distribution of Permian Carynginia shales that are converted from NMR T_2 distribution at fully saturation (S_w=100%).

4.3.1.2 Analysis of low-pressure N_2 gas adsorption

Figure 4. 4 presents the pore volume (V_p) distribution upon progressive thermal dehydration based on LP-N_2-GA. Peak curves (meaning the maximal water extraction) are discovered around 80°C dewatering temperature, followed by the converse reductions at higher temperatures. **Figure 4. 4** presents an overlapping PSD trend: (1) the continuous PSD increment (40°C-80°C); (2) an anomalous PSD reduction (80°C-90°C); (3) the relative stabilization period (90°C-120°C). The trend observed in LP-N_2-GA (**Figure 4. 4**), is highly consistent with NMR results in **Figure 4. 2**. The anomaly occurred above 80°C, which is detected by both methods, suggesting that the anomaly in NMR is not caused in an accident. Instead, temperature around 80°C may indicate critical implications. Therefore, more temperatures close to 80°C were specifically added for further investigation.

As found in **Figure 4. 4**, obvious pore volume escalation occurs across 40°C to 75°C, indicating that more and more pore surface area, which is initially occupied by water molecular, is thermally released to spare more surface area for N_2 adsorption. Notably, the maximum PSD interpreted by N_2 adsorption is presented at 80°C (**Figure 4. 4**), indicating the maximum water extraction occurs around 80°C. Great similarities of pore structure parameters, i.e., PSD curve (**Figure 4. 4**), SSA (**Figure 4. 5**) and pore volume (**Figure 4. 6**), are shown between 75°C and 80°C, presenting peak values close to each other.

Moreover, a clear boundary of 17nm is identified (**Figure 4. 4**), separating pores in 2-17nm (finer mesopore) and 17-100nm (coarse pore) range. The resemblant bimodal PSDs represent the predominant peak in 17-100nm for our samples with abundant mixed illite/smectite and

illite/muscovite. This is in a good agreement with the study of Kuila and Prasad (2013), which suggested that the dominant pore diameter of illite/smectite was located in 10-100nm. Therefore, the thermally removed water could be separately quantified in 2-17nm and 17-100nm pore range, by comparing the pore volume at individual temperatures with the peak value.

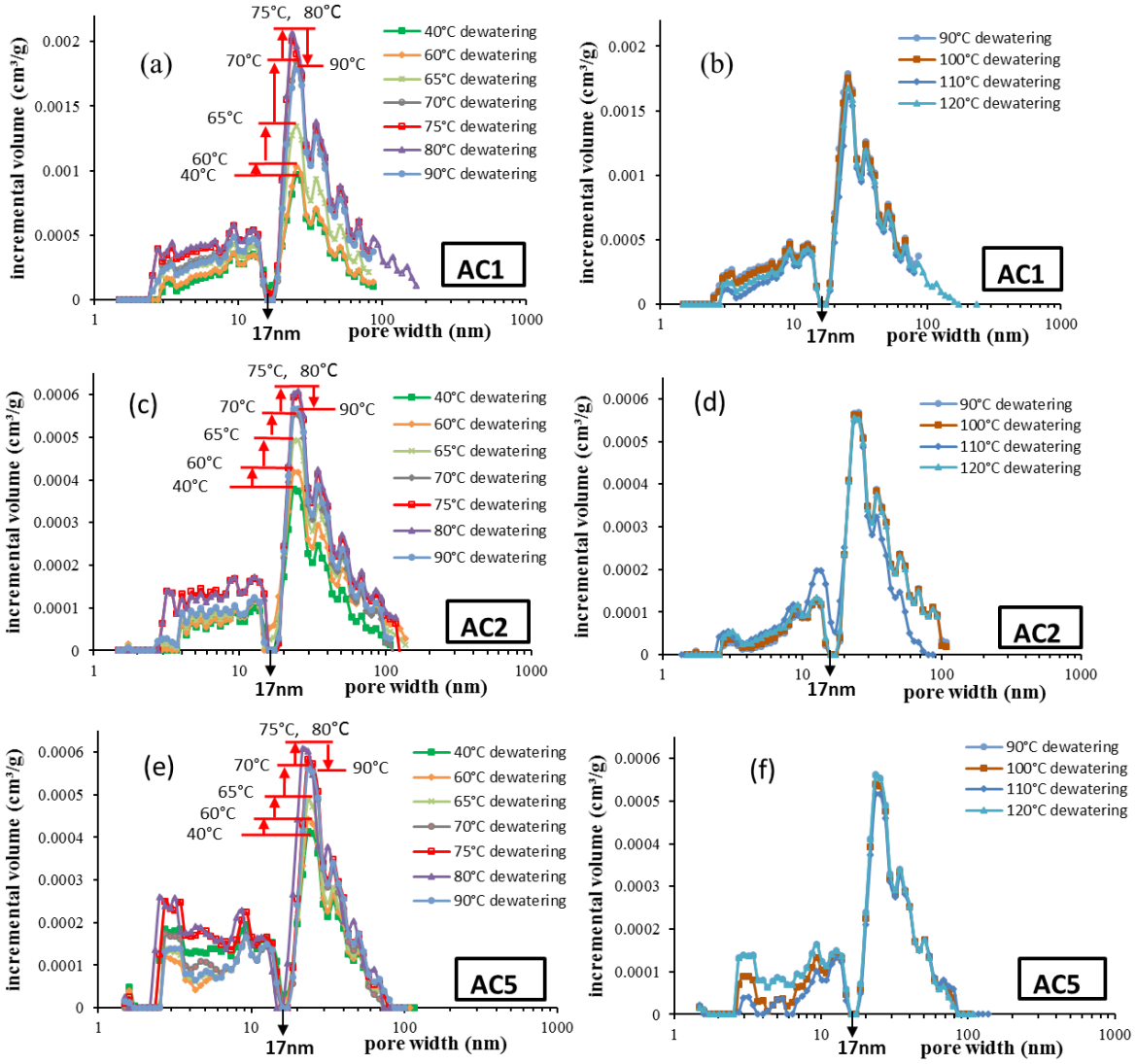

Figure 4. 4 PSD of samples from low-pressure N_2 gas adsorption, showing incremental pore volume changes upon thermal dehydration procedures.

Table 4. 2 demonstrates the variations of V_p and SSA at various temperatures. The peak value of $V_{p(2\text{-}17nm)}$ ranges from 0.003 to 0.01cm³/g, accounting for 32%-44 vol.% of the total pore volume in 2-100nm pore range. Particularly, the average 20.8 vol.% of $V_{p(2\text{-}17nm)}$ is accessible for competitive water adsorption, which could be extracted by thermal heating.

While in contrast, the peak value of $V_{p(17\text{-}100nm)}$ ranges from 0.005 to 0.022cm³/g, constituting 56-69 vol.% total pore volume, with up to 29.3 vol.% of $V_{p(17\text{-}100nm)}$ available for the residence of thermal-movable competitive water.

To evaluate the volume of thermal-removable water in different pore size range (i.e. 2-17nm and 17-100nm), we calculated the $\%\Delta V_p$, which refers to the ratio of the pore volume change to the maximum pore volume. In **Table 4. 2**, the largest value of $\%\Delta V_{p(17\text{-}100nm)}$ is presented in AC1 (i.e., 38.4 vol.% upon 40-80°C; 36.4 vol.% upon 60-80°C). Comparably, $\%\Delta V_{p(17\text{-}100nm)}$ of AC2 and AC5 is found to be lower (i.e., AC2 shows 25.7 vol.% upon 40-80°C; 13.3 vol.% upon 60-80°C, while AC5 provides 23.9 vol.% upon 40-80°C; 11.9 vol.% upon 60-80°C), indicating that the pore water hosted in the major 17-100nm pore range is easier to be removed in AC1.

Conversely, water extraction in 2-17nm shows a different scenario. AC1 presents the lowest $\%\Delta V_{p\ (2\text{-}17nm)}$ (16.9 vol.% upon 40-80°C; 15.9 vol.% upon 60-80°C), compared with AC2 (23.3 vol.% upon 40-80°C; 23.3 vol.% upon 60-80°C) and AC5 (22.3 vol.% upon 40-80°C; 22.1vol.% upon 60-80°C). This indicates a significant variation of pore water behaviour in different pore range, which is due to the interaction between water and the joint impact of mineral and organic matter related pore systems (Furmann et al. 2016, Loucks et al. 2009, Chalmers et al. 2012, Yu et al. 2018). This part is further discussing in another manuscript.

Table 4. 2 Pore structure parameters of Permian Carynginia shale samples conducted with LP-N_2-GA test. Note that SSA refers to the specific surface area interpreted from BET model; $V_{p\ (2\text{-}17nm)}$ and $V_{p\ (17\text{-}100nm)}$ refers to the pore volumes ranging in pore size of 2-17nm and 17-100nm respectively based on DFT model; $V_{p\ (2\text{-}100nm)} = V_{p\ (2\text{-}17nm)} + V_{p\ (17\text{-}100nm)}$; $\%\Delta V_{p\ (2\text{-}17nm)}$ is the ratio of the pore volume change in 2-17nm to the maximum pore volume; while $\%\Delta V_{p\ (17\text{-}100nm)}$ is the ratio of the pore volume change in 17-100nm to the maximum pore volume.

Sample	AC1	AC2	AC5	$\%\Delta V_{p(2\text{-}17nm)}$			$\%\Delta V_{p(17\text{-}100nm)}$		
				AC1	AC2	AC5	AC1	AC2	AC5
40°C dewatering and outgassing									
SSA (m²/g)	8.213	1.793	6.184						
$V_{p(2\text{-}17nm)}$ (cm³/g)	0.005	0.001	0.003	16.9	23.3	22.3	38.4	25.7	23.9
$V_{p(17\text{-}100nm)}$ (cm³/g)	0.009	0.004	0.004						
$V_{p(2\text{-}100nm)}$ (cm³/g)	0.014	0.005	0.007						
60°C dewatering and outgassing									
SSA (m²/g)	8.487	1.804	6.359						
$V_{p(2\text{-}17nm)}$ (cm³/g)	0.005	0.001	0.002	15.9	23.3	22.1	36.4	13.3	11.9
$V_{p(17\text{-}100nm)}$ (cm³/g)	0.010	0.005	0.004						
$V_{p(2\text{-}100nm)}$ (cm³/g)	0.015	0.006	0.006						
70°C dewatering and outgassing									
SSA (m²/g)	8.856	2.056	6.625						

$V_{p(2\text{-}17nm)}$ (cm^3/g)	0.007	0.002	0.004						
$V_{p(17\text{-}100nm)}$ (cm^3/g)	0.016	0.005	0.004	7.82	9.99	8.72	17.60	10.43	8.23
$V_{p(2\text{-}100nm)}$ (cm^3/g)	0.023	0.007	0.009						
75°C dewatering and outgassing									
SSA (m^2/g)	9.312	2.612	6.820						
$V_{p(2\text{-}17nm)}$ (cm^3/g)	0.010	0.003	0.004						
$V_{p(17\text{-}100nm)}$ (cm^3/g)	0.020	0.006	0.005	1.62	4.24	4.09	5.20	2.57	3.81
$V_{p(2\text{-}100nm)}$ (cm^3/g)	0.030	0.009	0.009						
80°C dewatering and outgassing									
SSA (m^2/g)	9.325	2.582	6.810						
$V_{p(2\text{-}17nm)}$ (cm^3/g)	0.010	0.003	0.004						
$V_{p(17\text{-}100nm)}$ (cm^3/g)	0.022	0.006	0.005	---	---	---	---	---	---
$V_{p(2\text{-}100nm)}$ (cm^3/g)	0.032	0.009	0.009						
90°C dewatering and outgassing									
SSA (m^2/g)	8.224	1.612	4.866						
$V_{p(2\text{-}17nm)}$ (cm^3/g)	0.007	0.001	0.002	11.2	19.5	20.1	8.8	1.8	1.1
$V_{p(17\text{-}100nm)}$ (cm^3/g)	0.018	0.006	0.005						
$V_{p(2\text{-}100nm)}$ (cm^3/g)	0.025	0.007	0.007						
100°C dewatering and outgassing									
SSA (m^2/g)	8.230	1.770	4.787						
$V_{p(2\text{-}17nm)}$ (cm^3/g)	0.007	0.001	0.002	10.6	18.0	30.1	13.0	2.4	2.0
$V_{p(17\text{-}100nm)}$ (cm^3/g)	0.017	0.006	0.004						
$V_{p(2\text{-}100nm)}$ (cm^3/g)	0.024	0.007	0.006						
110°C dewatering and outgassing									
SSA (m^2/g)	8.230	1.770	4.787						
$V_{p(2\text{-}17nm)}$ (cm^3/g)	0.007	0.002	0.001	9.9	10.3	35.5	14.6	15.1	2.9
$V_{p(17\text{-}100nm)}$ (cm^3/g)	0.017	0.005	0.006						
$V_{p(2\text{-}100nm)}$ (cm^3/g)	0.023	0.007	0.007						
120°C dewatering and outgassing									
SSA (m^2/g)	7.974	1.775	4.852						
$V_{p(2\text{-}17nm)}$ (cm^3/g)	0.005	0.002	0.002	14.2	15.1	20.1	15.2	3.6	1.1
$V_{p(17\text{-}100nm)}$ (cm^3/g)	0.017	0.005	0.005						
$V_{p(2\text{-}100nm)}$ (cm^3/g)	0.022	0.007	0.007						

4.3.2. Clay mineral conversion

In LP-N_2-GA, the first significant observation is the peculiarly sharp drop of SSA and pore volume after 75°C (or 80°C) peak. As depicted in **Figure 4. 5**, SSA of shale samples (i.e., AC1, AC2, AC5) drops from peak value (i.e., 9.33 m^2/g, 2.58 m^2/g and 6.81 m^2/g) at around 80°C to a relatively low average value (i.e., 8.16 m^2/g 1.74 m^2/g, 4.83 m^2/g) between 90-120°C**Table 4. 2**. Likewise, an abnormal sharp drop of pore volume is obviously shown from 80°C to 90°C (**Figure 4. 6**), while no evident inflection is perceived between 90°C and 120°C. As clay mineral components, such as smectite and illite, have been suggested to significantly contribute

to shale pore structure parameters (i.e., PSD, SSA and pore volume) (Kuila and Prasad 2013), the striking drop of SSA and pore volume may be caused by mineral phase change. Further, considering that clay minerals in shale dominantly contribute to effective adsorption site that is largely dependent on SSA (Ross and Bustin 2009), a conversion between clay minerals is assumed and tested. Previous studies documented that SSA of smectite is identified to be overwhelmingly larger (i.e., 346 m^2/g) compared to illite (i.e., 83m^2/g) (Macht et al. 2011), or other clays in shale (Ross and Bustin 2009, Kuila and Prasad 2013, Macht et al. 2011). Also, inter-crystal pore space was found to be larger in smectite (Geatches et al. 2014, Geatches and Wilcox 2014). Therefore, clay conversion between smectite to illite conversion (S-I conversion) is likely to occur, which can be used to explain the peculiar reduction of SSA and pore volume in LP-N_2-GA test.

Additionally, the comparison of pore volume change from 80°C to 90°C in 2-17nm (finer mesopore) and 17-100nm (coarser pore) range can confirm the S-I conversion. As shown in **Table 4. 2**, $\%\Delta V_p$ from 80°C to 90°C in fine mesopore range (2-17nm) presents to be larger than that in coarse pore range (17-100nm), i.e., $\%\Delta V_{p\,(2\text{-}17nm)}$ is calculated to be 11.2%, 19.5% and 20.1% for AC1, AC2, AC5, while $\%\Delta V_{p\,(17\text{-}100nm)}$ reveals the obviously smaller values of 8.8%, 1.8% and 1.1%, indicating that the pore volume reduction from 80°C to 90°C mainly occurred in fine mesopores. Literatures suggested that the PSD peak in smectite locates around 3nm fine mesopore range while illite has a larger value (Kuila and Prasad 2013). This demonstrates that S-I transformation would substantially reduce pore volume in fine mesopore range, which could fit into the larger pore volume reduction in 2-17nm (finer pore range) observed in our study.

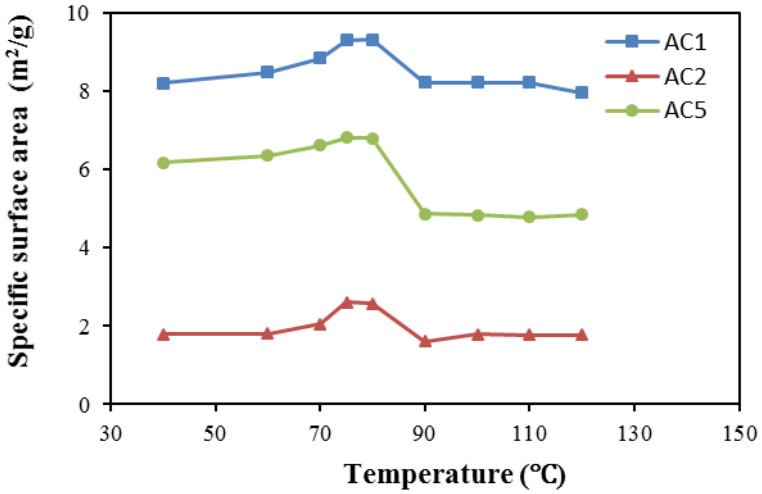

Figure 4. 5 The variation of specific surface area (SSA, m^2/g) calculated from Brunauer-Emmett-Teller (BET) method by using low-pressure N_2 gas adsorption isotherm with thermal treatment.

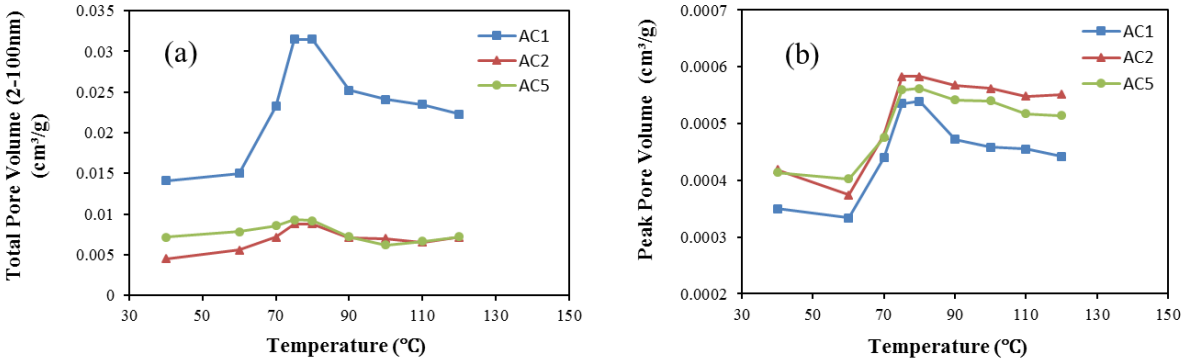

Figure 4. 6 The variation of (a) total pore volume $V_{p(17\text{-}100nm)}$, cm^3/g and (b) peak pore volume V_{peak}, cm^3/g calculated from density functional theory (DFT) by using low-pressure N_2 gas adsorption isotherm with thermal treatment.

The overlapped XRD patterns also provide further support for S-I conversion. As shown in **Figure 4. 7**, A newly-generated peak, which represents illite, occurred on the shoulder of the heated curves in AC2 and AC5. AC1 presents an intensified illite peak in the same position of heated curve compared to the untreated natural curve, indicating an increasing illite percentage in our test samples. Moreover, illite/smectite bump in heated curve presents to be flatter after 90°C heated, demonstrating a potential reduction of smectite proportion, which is induced by thermal heating.

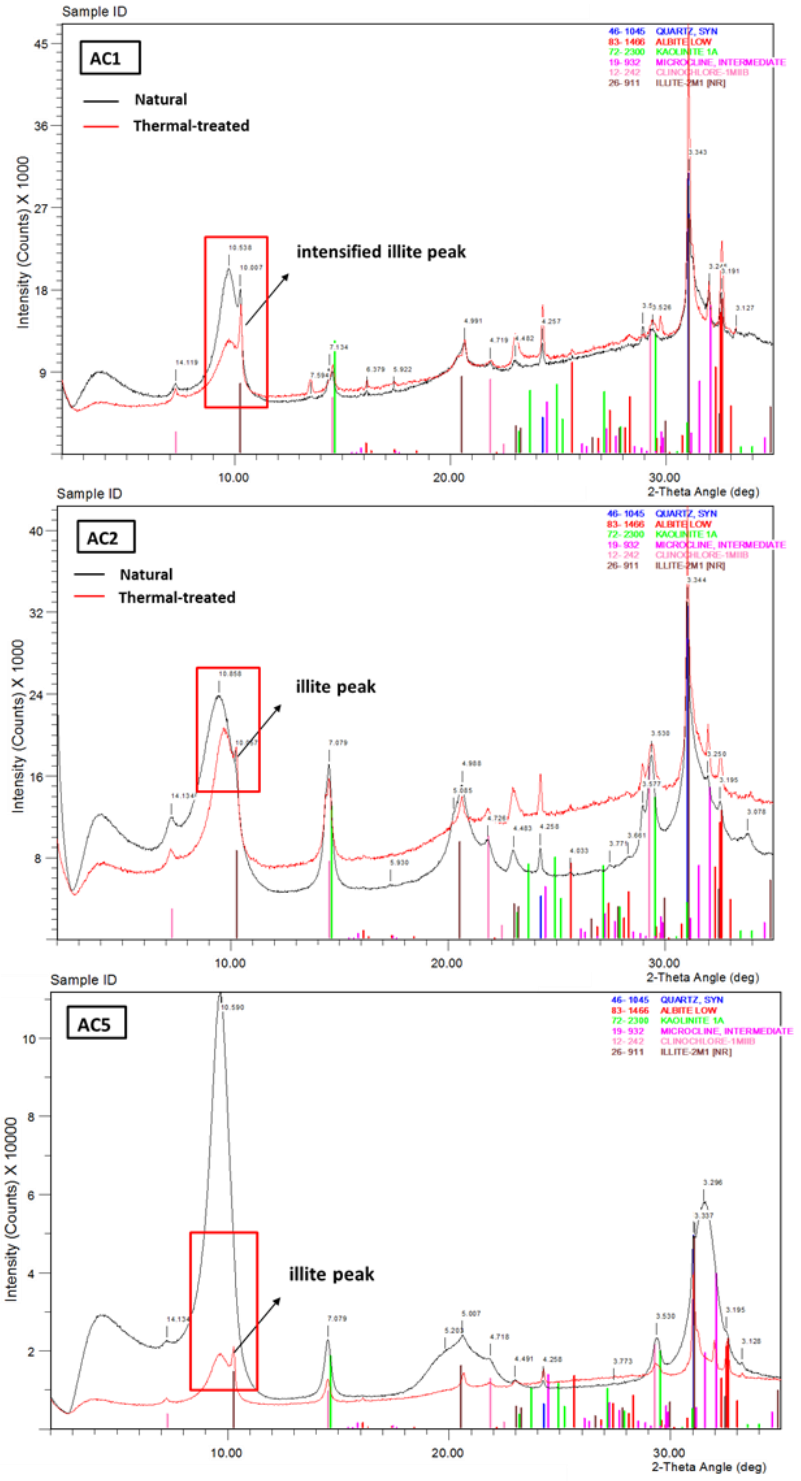

Figure 4. 7 The combined XRD patterns of natural (black line) and 90°C heated (red line) of AC1, AC2, AC5. Note that the different scales of the black and red curve is due to the various amount of sample fractions prepared for the test.

The second critical aspect of LP-N_2-GA results is that no evident change in pore properties, i.e., PSD (**Figure 4. 4**b,d,f), SSA (**Figure 4. 5**) and pore volume (**Figure 4. 6**) could be found between 90°C and 120°C. These consistent phenomena between pore structure parameters indicate that no further S-I conversion was yielding in this specific temperature region. Hence,

it is reasonable to infer that the release of CBW from smectite occurred between 80-90°C, above which no obvious S-I conversion continued. Similar completed temperature of S-I transformation was reported by Hower et al. (1976), demonstrating that S/I proportion remained unchangeable (~20/80) after reaching 95°C, while Freed and Peacor (1989) documented the completion temperature located between 88-142°C.

All above, to accurately interpret pore structure in gas shale, pore surface of clay minerals should be maximally cleaned, while keeping sensitive clay (i.e., smectite) well-protected. Obviously, both 75°C and 80°C indicate the maximal water extraction, however, when it comes to the temperature-sensitivity of shale components, the lower temperature the better. Therefore, the highest dewatering temperature of 75°C is recommended for gas shale pore interpretation to protect CBW, together with the complex pore structure. Further, CBW quantification and the determination of T_2 cutoff for CBW is applicable in unconventional shales, by applying the crucial temperature in NMR technique.

4.3.3. The determination of NMR T_2 cut-off for CBW

In **Figure 4. 2**a,c,e, merely slight difference in T_2 distributions is shown between S_w curve and the 'S_{ir}' curve after centrifuging at 4500 rpm, which indicates that only a small amount of free water was expelled from large pores/fractures (>100nm) in our shales, while no obvious water expulsion is observed in smaller pores (<100nm). Centrifuging at 4500 rpm with 315 psi is found poorly applied to differentiate pore water in shales from Permian Carynginia formation, Perth Basin. Comparably, the S_{ir} curve after heating demonstrates a stepwise shrinkage in pore size less than 100nm. No further reduction occurs after 80°C even temperature increases higher, identifying the residual water as the irreducible volume of CBW that can be calculated from T_2 cutoff.

Our updated T_2 cutoff for CBW in Permian Carynginia shale is calculated based on **Figure 4. 8**. Two cumulative T_2 spectrum respectively correspond to S_w and S_{ir} conditions, with the maximum value representing total porosity and irreducible porosity. Instead of applying the commonly used S_{ir} after centrifuge (Coates et al. 1999), S_{ir} at 80°C is employed for CBW calculation. Note that NMR test was stepwise conducted on thermal-treated samples after fully saturation, the heating process was irreversible, which indicates that 75°C is not available to be performed on the same heated core plugs. As almost no differences in petrophysical properties (i.e., PSD in **Figure 4. 4**; SSA in **Figure 4. 5**; pore volume in **Figure 4. 6**) are

presented between 75°C and 80°C, 80°C is reasonably to be used in NMR T_2 spectrum to maximally extract movable pore water. T_2 cutoff for CBW is then obtained by horizontally projecting the peak of cumulative S_{ir} curve to cumulative S_w curve, followed by projecting down at the intersection for T_2 value. The calculated T_2 cutoff is 0.205ms, 0.177ms and 0.210ms for AC1, AC2 and AC5 respectively, while a range of 0.17-0.26ms is provided by all the tested samples in Perth Basin (**Table 4. 3**). Previous NMR study on Middle Bakken and Three Forks Formation shales of high clay content demonstrated T_2 cutoff between 1.34 and 1.40ms (Saidian and Prasad 2015), while Barnett gas shale was suggested around 3ms (Sondergeld et al. 2010a) due to different mineralogical composition and geochemical characteristics, which would be further investigated in another paper. CBW in Permian Carynginia shale of Perth Basin is quantified to constitute 1.7-3.0% of the bulk volume, while the effective porosity, which is calculated by subtracting the volume of CBW from NMR total porosity (Rylander et al. 2013, Prammer et al. 1996, Easley et al. 2007), is quantified between 6.28-11.23% (**Table 4. 3**)

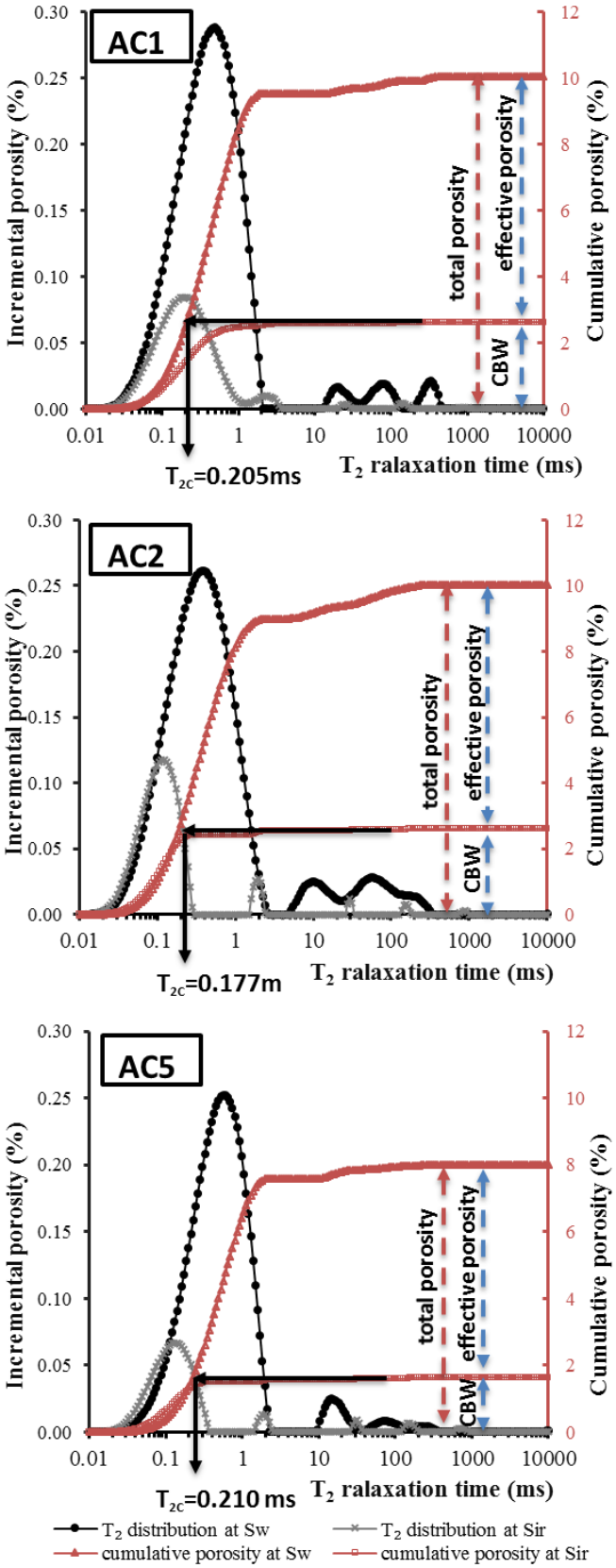

Figure 4. 8 NMR distribution at fully saturation (S_w=100%) and at irreducible water condition after heat treatment (S_{ir}) for the determination of T_2 cutoff (T_{2c}).

What's worth mentioning, although PSD range and the variation trend in various heating temperatures indicate a good agreement between NMR and LP-N_2-GA, the difference on distribution modal could still be discovered, which is due to the application of different working fluids with various kinetic molecular diameter. The accessible porosity and PSD interpretation by fluid invasion approach are documented as a function of molecular size, temperature and pressure (Clarkson et al. 2013). Additionally, the variation of tested sample scale, such as core plug used in NMR versus fragments used in LP-N_2-GA, would also account for PSD distinction (Sondergeld et al. 2010b).

Table 4. 3 Petrophysical properties of the test samples based on NMR analysis.

Sample	NMR total porosity, %	T_2 cutoff for CBW, ms	CBW, %	Effective porosity,%
AC1	10.06	0.205	2.62	7.44
AC2	10.04	0.177	2.60	7.44
AC4	10.66	0.170	2.54	8.12
AC5	12.87	0.210	1.64	11.23
AC7	9.89	0.255	3.02	6.87
AC8	8.02	0.217	2.73	5.29
AC9	9.26	0.195	2.95	6.31

4.4. Conclusions

CBW evaluation is highly related to pore characterization in shale. The combination of LP-N_2-GA and NMR test under thermal dehydration schemes determines a temperature around 80°C (75°C), in which the removable pore water can be maximally extracted from complicated pore structure. Dewatering temperatures below 75°C would result in misinterpretation of nanopore structure due to the insufficient removal of pore water. Heating temperatures above 80°C would induce smectite to illite conversion and the loss of CBW. This study re-defines the critical cutoff temperature in NMR, which enable the quantification of CBW and effective porosity. Also, it is able to determine the NMR T_2 cutoff for CBW, providing implications for petrophysical practice in shale.

CHAPTER 5 Fractal analysis of the pore structure for clay bound water and potential gas storage in shales based on NMR and N_2 gas adsorption

This chapter is a published paper in *Journal of Petroleum Science and Engineering*:

Yuan, Y., and Rezaee, R., 2019, Fractal analysis of the pore structure for clay bound water and potential gas storage in shales based on NMR and N_2 gas adsorption: Journal of Petroleum Science and Engineering. (Yuan and Rezaee 2019b)

5.1. Introduction

Global energy shortage has led to great interests in worldwide shale investigations (Rezaee 2015, Loucks and Ruppel 2007). Unlike sandstones or carbonates, the porous media in unconventional shales present to be significantly more complex and heterogeneous (Bustin et al. 2008). It is the petrophysical properties (i.e., pore morphology, pore size distribution, pore volume complexity and pore surface roughness), instead of only porosity, that significantly controls and influences hydrocarbon accumulation and transmission rates (Shao et al. 2017, Loucks et al. 2009, Loucks et al. 2012, Rezaee 2015, Yu et al. 2018, Liu and Ostadhassan 2017). As a source rock, gas storage in shales is constituted by free gas and a large proportion of adsorbed gas (Jarvie et al. 2007), which intimately associated with the heterogeneity of pore volume and pore surface (Zhou and Kang 2016). The low permeability and effective porosity, coupled with the existing volume of clay bound water (CBW) which is irreducibly adsorbed and bound on clay surface that would largely reduce effective porosity, are crucial for producibility estimation and largely influenced by geometric complexity of pore surface and pore volume (Coates et al. 1999, Yuan et al. 2018b, Tan et al. 2015, Rezaee et al. 2012).

To characterize the complicated nano-scaled pore structure in shales, various techniques have been applied including microscopic observations (Chalmers et al. 2012, Mastalerz et al. 2013) and fluid penetration approaches (Clarkson et al. 2013, Labani et al. 2013, Rezaee et al. 2012). Advantages and drawbacks concurrently exist in each technique. The microscopic imaging methods, i.e., transmission electron microscopy (TEM) and focused ion beam-scanning electron microscopy (FIB-SEM), are capable to obtain the connectivity and geometric images of pore system (Chalmers et al. 2012, Milliken et al. 2013), but the images obtained from spot techniques appear to be objective and unavailable to be upscaled into larger rock volumes (Furmann et al. 2016, Loucks et al. 2009). Fluid invasion approaches, i.e., mercury

injection capillary pressure (MICP), nuclear magnetic resonance (NMR) and low-pressure gas adsorption (LP-GA) are able to cover a wide range of pore size distribution and quantify the pore structure parameters (Chalmers et al. 2012, Rezaee 2015, Mastalerz et al. 2013), while the critical heterogeneity of pore volume and pore surface is not available to be directly quantified. More recently, it has been revealed that invasion approaches such as NMR and LP-GA, are adaptable for pore heterogeneous quantification by mathematically processed under fractal analysis (Stallmach et al. 2002, Avnir et al. 1984, Zhang and Weller 2014).

The fractal theory was initially introduced in material science to describe the fragmented irregular and geometrically disordered objects, which is referred as 'fractals' (Avnir and Jaroniec 1989, Mahamud and Novo 2008, Mandelbrot et al. 1984). Unlike the classical Euclidean geometry categorizing the ordered objects into 'points, lines, surfaces and cubes' that correspond to the integral topological dimension of '0, 1, 2, 3', respectively, fractal objects, however, display the non-integral values in fractal dimension under the detection of various resolution scales in 'length, surface area and volume' (Yu and Cheng 2002). Microscopically, rock surface displays a property of 'self-similar regularity' at molecular scales; and exhibits a similar structure regularity over 3-4 orders of the magnitude resolution scales in length between 1nm-100 μm (Avnir et al. 1984, Katz and Thompson 1985, Yu and Li 2001). The self-similarity is represented by fractal dimension (D), an index to characterize the fractal patterns with a constant value over scale ranges (Pfeifer 1984, Mandelbrot 1983, Mandelbrot et al. 1984); and has been applied as a quantitative parameter in shale studies (Yang et al. 2014, Bu et al. 2015, Liu et al. 2018a, Liu et al. 2018b). Shale pore structures (i.e., pore surface and pore volume) were identified in fractal and heterogeneous geometries for gas adsorption by using the laboratory LP-GA adsorption isotherm in couple with Frenkel-Halsey-Hill (FHH) model (Jaroniec 1995, Tatlıer and Erdem-Şenatalar 1999). Also, fractal analysis conducted on NMR technique, which is identified as a non-destructive approach to quantify the wide range of pore network and is beneficial to differentiate pore types containing various fluids (Coates et al. 1999, Straley et al. 1997, Rezaee et al. 2012, Yuan et al. 2018b, Zhou et al. 2016), has been proved to be applicable in rock petrophysical analysis. Previously, the NMR-based fractal analysis was primarily performed on conventional porous media (Stallmach et al. 2002), coals (Zhou et al. 2016, Ouyang et al. 2016) and tight sandstones (Shao et al. 2017), while limited investigations were conducted on pore fractal in shales pore (Ross and Bustin 2009) and abundant with clays as the site for adsorption (Jarvie et al. 2007), understanding the fractal heterogeneity of different pore type, particularly the effective pores and ineffective pores

occupied by CBW is significant for the potential shale gas storage estimation (Topór et al. 2016, Prammer et al. 1996, Saidian and Prasad 2015, Tan et al. 2015). However, as laboratory CBW identification and quantification is challenging in shales (Passey et al. 2010), the impact of effective and ineffective pore structure heterogeneity on petrophysical properties remains poorly understood.

Recently, the authors have successfully differentiated CBW from effective porosity (Yuan et al. 2018b). To fully address the fractal complexity of effective pores and the ineffective pores for CBW, this study extends our previous work (Yuan et al. 2018b) by conducting fractal analysis on the experimental NMR T_2 spectrum and LP-N_2-GA isotherms of the tested samples. Conclusions are utilized to understand how the fractal heterogeneity correlates with CBW, effective porosity and the potential gas storage capacity in shale gas reservoirs.

5.2. Methodology

5.2.1 Samples and experiments

A total of seven shale samples in various depth were collected from Arrowsmith well in Permian Carynginia formation of Perth Basin, Western Australia. Geological details of the tested samples were documented in the author's previous research work (Yuan et al. 2018b).

Shale plugs with a diameter of 1.5" were cleaned with toluene and fully saturated with brine water under 2000psi until constant weight has been reached. NMR tests were conducted on 2MHz Magritek Core Analyzer instrument to obtain T_2 spectrum for fractal analysis. Carr, Purcell, Meilboom and Gill pulse sequence (Carr and Purcell 1954, Kenyon et al. 1995, Meiboom and Gill 1958) were used with the setting parameters as follows: 100 μs inter-echo spacing (TE), 10000 ms inter-experiment delay, 10000 number of echoes and the minimum 200 signal to noise ratio (SNR). Theoretically, NMR relaxation mechanism is associated with surface relaxation, diffusion relaxation and bulk relaxation, while the bulk and diffusion relaxation are negligible for the application of uniform electromagnetic field with short TE on bine-saturated samples. The T_2 relaxation could be simplified as **Eq. (5.1)** (Coates et al. 1999):

$$\frac{1}{T_2} = \rho \left(\frac{S}{V}\right) \text{ …… (5.1)}$$

where ρ is the surface relaxivity, μs/m; $\frac{S}{V}$ is the specific surface area (the ratio of surface area to pore volume), μs^{-1}. To differentiate different fluids, initial NMR experiments were

performed on fully saturated core plugs, followed by centrifuging on VINCI Refrigerated Centrifuge apparatus at 4500 rpm under 315 psi. Heating pre-treatment on saturated samples was subsequently conducted using vacuum oven under temperatures from 50°C to 120°C to continuously extract pore water. By detecting the remaining hydrogen proton in pore structure, transverse relaxation (T_2) spectrum were obtained for characterization.

Low-pressure N_2 gas adsorption (LP-N_2-GA) was employed to obtain adsorption isotherm for fractal analysis. Prior to the measurement, shale samples were crushed and sieved into 60-meshed-size and vacuum degassed over 8h for pore surface cleaning. Measurements were conducted on Micromeritics® TriStar 3020 instrument at the bathing temperature of 77.4K. Detailed experiment setups and procedures have been included in our previous work (Yuan et al. 2018b).

5.2.2. Fractal theory based on NMR and LP-N_2-GA

5.2.2.1 Fractal dimension from NMR

NMR fractal dimension was calculated based on NMR T_2 spectrum. As per fractal theory (Mandelbrot et al. 1984, Avnir et al. 1984), a power law relationship is deduced between N(r) ~ radius (r), which is asymptotically described as Eq.(5.2) and derived into Eq.(5.3):

$$N(r) = \int_r^{r_{max}} f(r)dr = \frac{C}{r^D} \quad \text{.....(5.2)}$$

$$f(r) = \frac{d\,N_{(r)}}{dr} = \frac{-D \cdot C}{r^{D+1}} \quad \text{..... (5.3)}$$

where N_r is the total number of pores of radii > r ; r is the radius of the equivalent capillary bundles; $f(r)$ is pore radius density function; C is a fractal factor and D is the fractal dimension. Cumulative pore volume with pore sizes smaller than r (V_r) is integral as Eq.(5.4) and total pore volume with full size of pores (V_t) was obtained in Eq.(5.5) (Coates et al. 1999, Shao et al. 2017):

$$V_r = \int_{r_{min}}^{r} f(r)cr^3dr = \frac{-D \cdot C^2}{3-D}(r^{3-D} - {r_{min}}^{3-D}) \quad \text{..... (5.4)}$$

$$V_t = \frac{-D \cdot C^2}{3-D}({r_{max}}^{3-D} - {r_{min}}^{3-D}) \quad \text{..... (5.5)}$$

The ratio of the cumulative pore volume with pore size smaller than r to the total pore volume (V):

$$V = \frac{V_r}{V_t} = \frac{r^{3-D} - {r_{min}}^{3-D}}{{r_{max}}^{3-D} - {r_{min}}^{3-D}} \quad \ldots\ldots\ldots\ldots \quad (5.6)$$

In gas shale of nanometer-scaled pore radius, assuming $r_{min} \ll r$, Eq.(5.6) is thus simplified into:

$$V = (\frac{r}{r_{max}})^{3-D} \quad \ldots\ldots\ldots\ldots \quad (5.7)$$

Given that NMR theory suggest a proportional relationship between T_2 and pore size, Eq.(5.7) was converted into Eq.(8) and subsequently logarithmetized as Eq.(5.9):

$$V = (\frac{T_2}{T_{2\,max}})^{3-D} \quad \ldots\ldots\ldots\ldots \quad (5.8)$$

$$\log(V) = (3 - D)\log(T_2) + (\mathrm{D} - 3)\log(T_{2max}) \quad \ldots\ldots\ldots\ldots \quad (5.9)$$

As shown in Eq.(5.9), the fractal dimension (D) can be determined based on the slope of the double logarithmic plot. D is calculated from different segments in T_2 spectrum by applying T_2-cutoff value, which differentiates different fluid-bearing pore types in shales. As gas shale is characterized by tight texture, the conventional fluid differentiation approach, i.e., centrifuging, poorly works on the determination of $T_{2\text{-cutoff}}$. Centrifuge rotation higher than 4500 rpm (315 psi) would destroy some of the Permian Carynginia shale samples, while centrifuge ≤ 4500 rpm extracted little water (Yuan et al. 2018b). Take AC1 as an example, as shown in **Figure 4. 1**, no apparent differences in incremental porosity occurred after centrifuge. By performing heating pre-treatment on samples from 50-120°C prior to NMR tests, $T_{2\text{-cutoff}}$ values were available to be obtained for pore type separation under each temperature. The fractal analysis was subsequently carried out based on the determined T_2 critical value for the heterogeneity analysis of different pore types, as discussed in section 5.3.2.

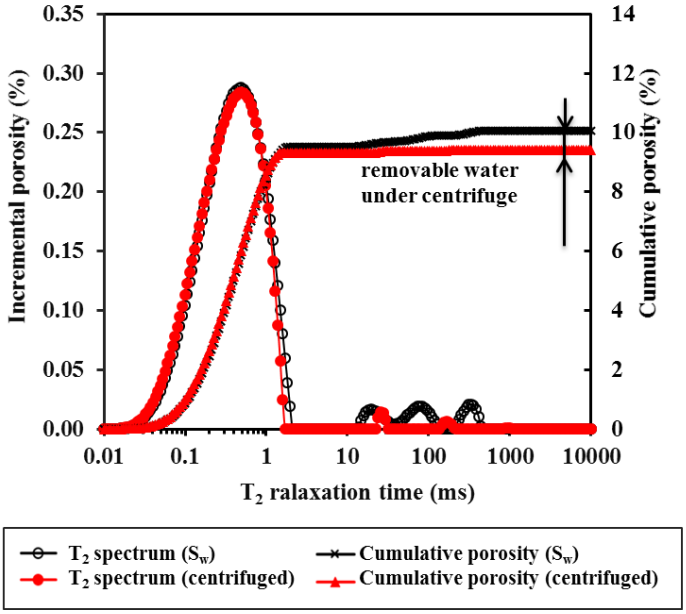

Figure 5. 1 NMR T_2 distribution of AC1 under fully saturated and centrifuged conditions. Note that other Permian Carynginia shale samples perform similar behaviours as AC1, with no apparent differences observed in incremental porosity curves after centrifuge.

5.2.2.2 Fractal dimension from LP-N_2-GA

The fractal analysis on low-pressure N_2 gas adsorption isotherm is derived from FHH model (Avnir and Jaroniec 1989). Fractal dimension (D) is calculated based on the relationship between the amount of adsorption and relative pressure as below:

$$\frac{V}{V_0} = \frac{N}{N_m} = K\left[\ln(\frac{P_0}{P})\right]^{D-3} \quad \ldots\ldots\ldots\ldots (5.10)$$

$$lnV = (D-3)\, ln\left[\ln(\frac{P_0}{P})\right] + C \quad \ldots\ldots\ldots\ldots (5.11)$$

$$A = (D-3) \quad \ldots\ldots\ldots\ldots (5.12)$$

where V is the amount of adsorbed gas under equilibrium pressure P, V_0 is the volume of monolayer coverage, $\frac{N}{N_m}$ is the layer number of adsorption, K is a constant, P_0 is the saturation pressure, D is the fractal dimension, C is a constant value and A is the slop the double logarithmic relationship between V and $\ln(\frac{P_0}{P})$. Fractal dimension (D) could be directly determined from the slop of the regressive relations.

5.3. Results and discussions

5.3.1. Fractal analysis based on NMR T_2 spectrum

Figure 5. 2 shows the changes of NMR responses and fractal properties (i.e., pore surface roughness, pore volume complexity) against temperature. AC1, AC2, AC5 and AC8 at 50°C are presented as examples for discussions (**Figure 5. 2**). Under each given temperature, region 1 and region 2 were differentiated by using the T_2 critical value as a cut-off boundary (T_{2c}), which is obtained by horizontally projecting the peak of NMR cumulative porosity curve under heating treatment to the cumulative fully-saturated (S_w) curve and projecting down at the intersection point to x-axis for the T_2 critical value (Yuan et al. 2018a). Region 1 and region 2 separately represents the immobile water and the removable water under the given temperature. By conducting linear regressions in both regions, good fitnesses were obtained with the correlation coefficients higher than 0.78 (**Figure 4. 2**b, d, f, h). The calculated D in region 1 (D_{imm}) and region 2 (D_{mov}) represents the fractal pore geometries associated with the immobile water and removable water, respectively. **Table 5. 1** summarizes the calculated fractal dimensions. As can be seen under each given temperature, D_{mov} is found always higher than D_{imm}. As immobile water in shales tends to sit on smaller pore surfaces, while movable water locates in relatively larger pore volumes, we assume D_{imm} is intimately associated with surface fractal dimension of smaller pores, which are essentially developed in fine clay minerals; by contrast, D_{mov} is associated with larger interpartical pores that mostly develop between granular quartz particles or clays as capillary pores; it is reasonable for the heterogeneous pore space, which is formed by quartz and clay combinations, displaying higher D_{mov} values over D_{imm} that exhibits less heterogeneity of clay pores.

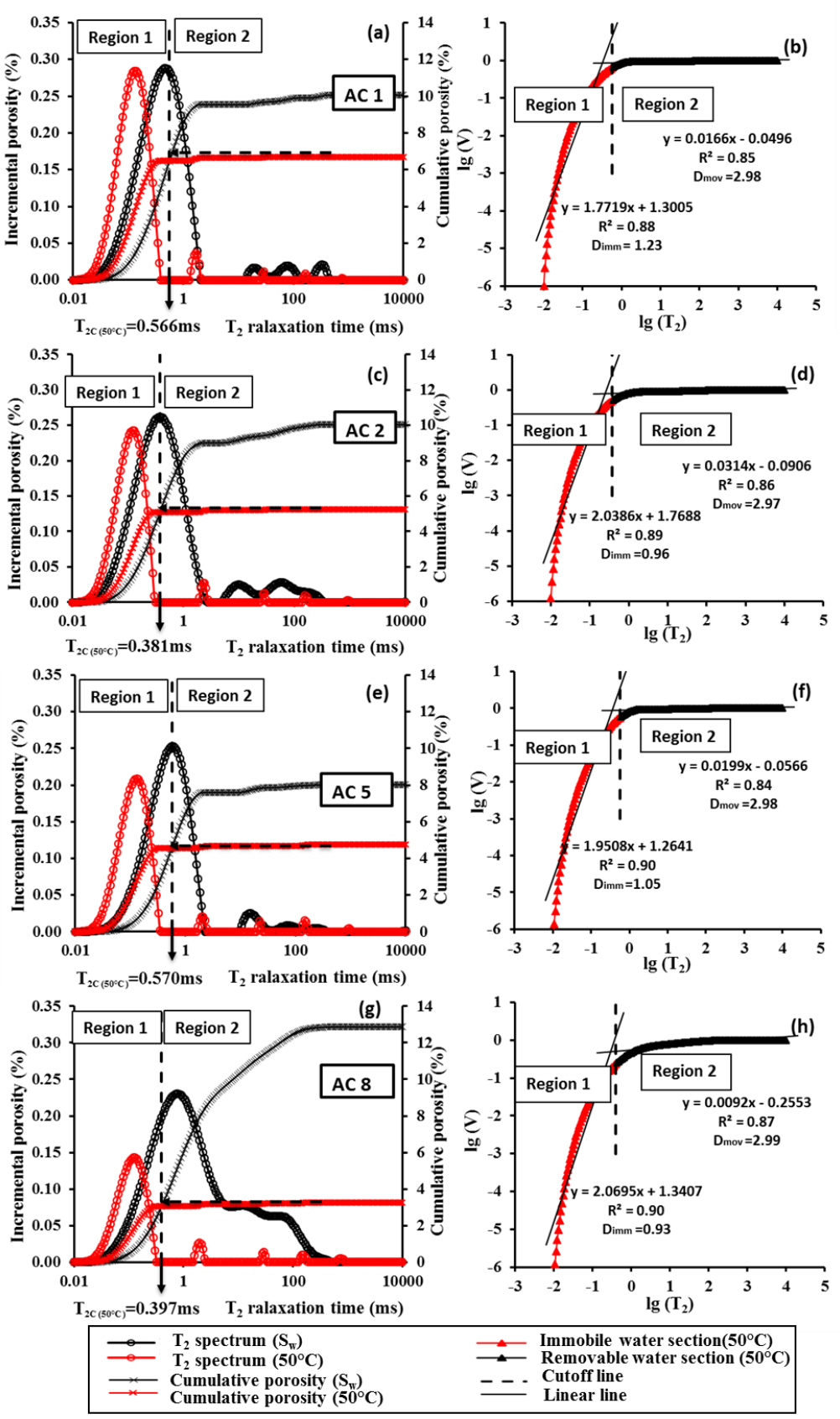

Figure 5. 2 Fractal analysis on Permian Carynginia shales, i.e., AC1, AC2, AC5, AC8, based on NMR T_2 spectrum under 50°C pre-heated treatment. Note that the dashed vertical lines perform as a boundary

cutoff between the immobile water (Region 1) and the removable water (Region 2) under the given temperature.

Table 5. 1 The fractal dimensions of AC1, AC2, AC5, AC8 calculated from NMR measurements under different pre-heated temperatures.

Sample	T (°C)	Region 1			T_{2c}	Region 2		
		K1	D_{imm}	R_1^2		K2	D_{mov}	R_2^2
AC1	50	1.77	1.23	0.88	0.566	0.02	2.98	0.85
	60	2.19	0.81	0.90	0.323	0.03	2.97	0.84
	80	2.64	0.36	0.91	0.205	0.09	2.91	0.85
	90	2.50	0.50	0.91	0.237	0.05	2.95	0.84
	100	2.44	0.56	0.91	0.260	0.04	2.96	0.84
	110	2.50	0.50	0.91	0.235	0.04	2.96	0.84
	120	2.50	0.50	0.91	0.234	0.04	2.96	0.84
AC2	50	2.04	0.96	0.89	0.381	0.03	2.97	0.86
	60	2.19	0.81	0.90	0.241	0.03	2.97	0.84
	80	2.76	0.24	0.92	0.177	0.06	2.94	0.85
	90	2.69	0.31	0.91	0.190	0.06	2.94	0.85
	100	2.69	0.31	0.91	0.186	0.06	2.94	0.85
	110	2.69	0.31	0.91	0.178	0.06	2.94	0.85
	120	2.69	0.31	0.91	0.190	0.06	2.94	0.85
AC5	50	1.95	1.05	0.90	0.570	0.02	2.98	0.84
	60	2.19	0.81	0.90	0.301	0.03	2.97	0.84
	80	2.78	0.22	0.93	0.210	0.07	2.93	0.84
	90	2.53	0.47	0.92	0.272	0.05	2.95	0.84

	100	2.56	0.44	0.92	0.239	0.05	2.95	0.84
	110	2.53	0.47	0.92	0.272	0.05	2.95	0.84
	120	2.55	0.45	0.92	0.239	0.05	2.95	0.84
	50	2.07	0.93	0.90	0.397	0.01	2.99	0.87
	60	2.41	0.59	0.91	0.262	0.02	2.98	0.86
	80	2.60	0.40	0.91	0.217	0.12	2.88	0.86
AC8	90	2.41	0.59	0.91	0.268	0.02	2.98	0.86
	100	2.41	0.59	0.91	0.263	0.02	2.98	0.86
	110	2.41	0.59	0.91	0.269	0.02	2.98	0.86
	120	2.36	0.64	0.91	0.232	0.02	2.98	0.86

To schematically describe the behaviour of water molecules on hydrophilic clay surfaces during thermodynamic processes, a proposed model is illustrated in **Table 5. 3**a-e. **Figure 4. 3**a displays the initial condition of fully-saturated pores with CBW and capillary water. The capillary water, which is physically confined in small capillary pores as a form of water bridge, is dominantly controlled by capillary force (Li et al. 2016, Gregg et al. 1967, Chalmers et al. 2012). Clay bound water, which is electrochemically bound on clay surface, tends to remain stable against low temperatures (Easley et al. 2007, Handwerger et al. 2011). As temperature increases, capillary water bridge gradually reduces, with its interfacial menisci withdraw towards the interior (**Figure 5. 3**b) until the capillary water completely separates (**Figure 5. 3**c). Caused by the continuously rising temperatures, capillary water gradually evaporates, resulting in a consistent reduction in water film thickness (**Figure 5. 3**d). As found in the author's previous work, the maximal extraction of the removable pore water occurs around 80°C, while the clay minerals, CBW and the nanopore structure in Permian Carynginia shales remain well-preserved (Yuan et al., 2018b). The residual irreducible water under 80°C, which is immobile even temperatures went higher to some extent, is attributed to the electrostatic CBW, exhibiting the minimal water film thickness as shown in **Figure 5. 3**e.

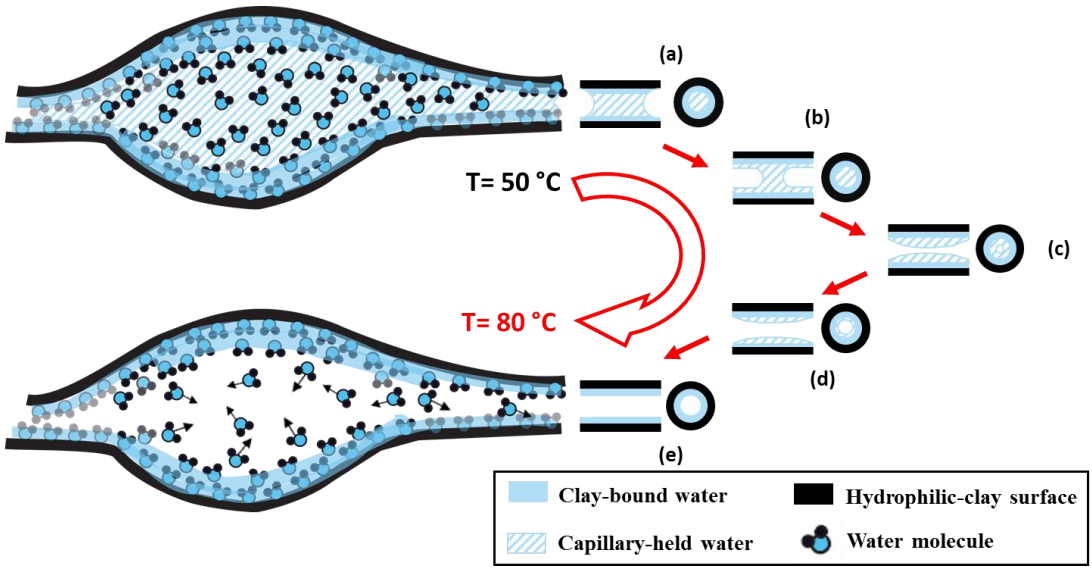

Figure 5. 3 Schematic for thermal extraction of pore water on the surface of hydrophilic clay minerals.

Figure 5. 4 displays the variations of D_{imm} and D_{mov} against temperatures under heating scheme. Both D_{imm} and D_{mov} curves present an overall sunk around 80°C. High D_{imm} values are shown at initial temperatures and decreases until the heating temperature reaches to 80°C. Similarly, in **Figure 5. 4**b, an initially high value of D_{mov} is followed by a consistent reduction to the minimum at around 80°C. The anomalous rise of D_{imm} and D_{mov} occurred above 80°C, followed by a stable region in 90-120°C with no apparent change (**Figure 5. 4**), which is consistent with the authors' previous discovery in the changes of specific surface area and pore volume against temperatures (Yuan et al. 2018b). As the temperature around 80°C was identified as the cutoff temperature that maximally separates immobile CBW from the removable water that is hosted in effective pores, further fractal analysis was performed under 80°C. The value of D_{imm} and D_{mov} under 80°C are specifically noted as D_{cbw} and D_{eff}, respectively (**Figure 5. 5**a-h). D_{cbw} represents the fractal dimension of CBW pore surface. D_{eff} represents the fractal dimension of effective pore volume, holding removable fluids that could be maximally extracted under 80°C (Yuan et al. 2018c). **Table 5. 2** summarized the calculated value of D_{cbw} and D_{eff} for the total of our seven samples. D_{cbw} is calculated in 0.22-0.47, while D_{eff} varies from 2.87-2.95. Further discussions for the sunk phenomenon around 80°C (**Figure 5. 4**) are conducted in section 5.3.3.

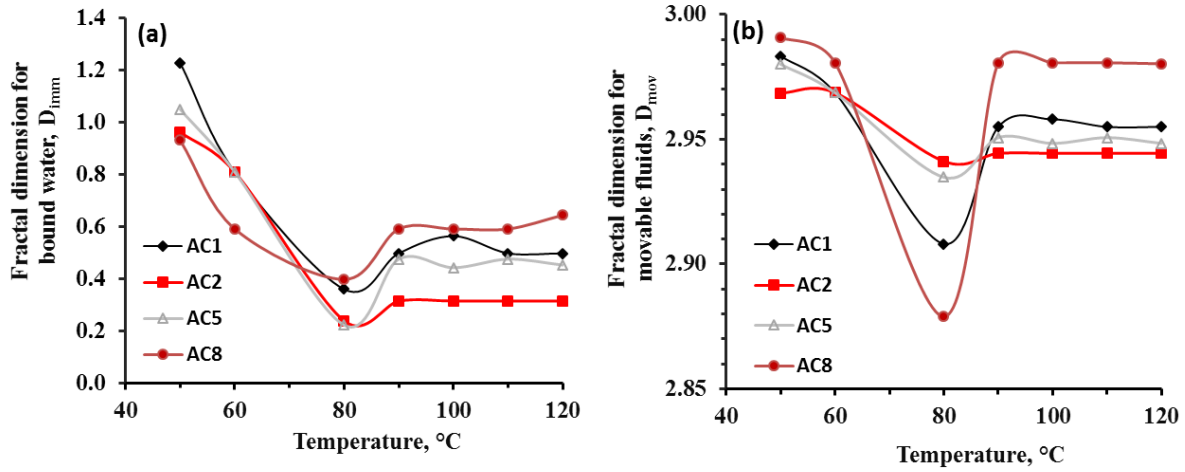

Figure 5. 4 Relationship for (a) fractal dimensions of immobile water (D_{imm}) and (b) fractal dimensions of removable water (D_{mov}) against temperatures in Permian Carynginia shales.

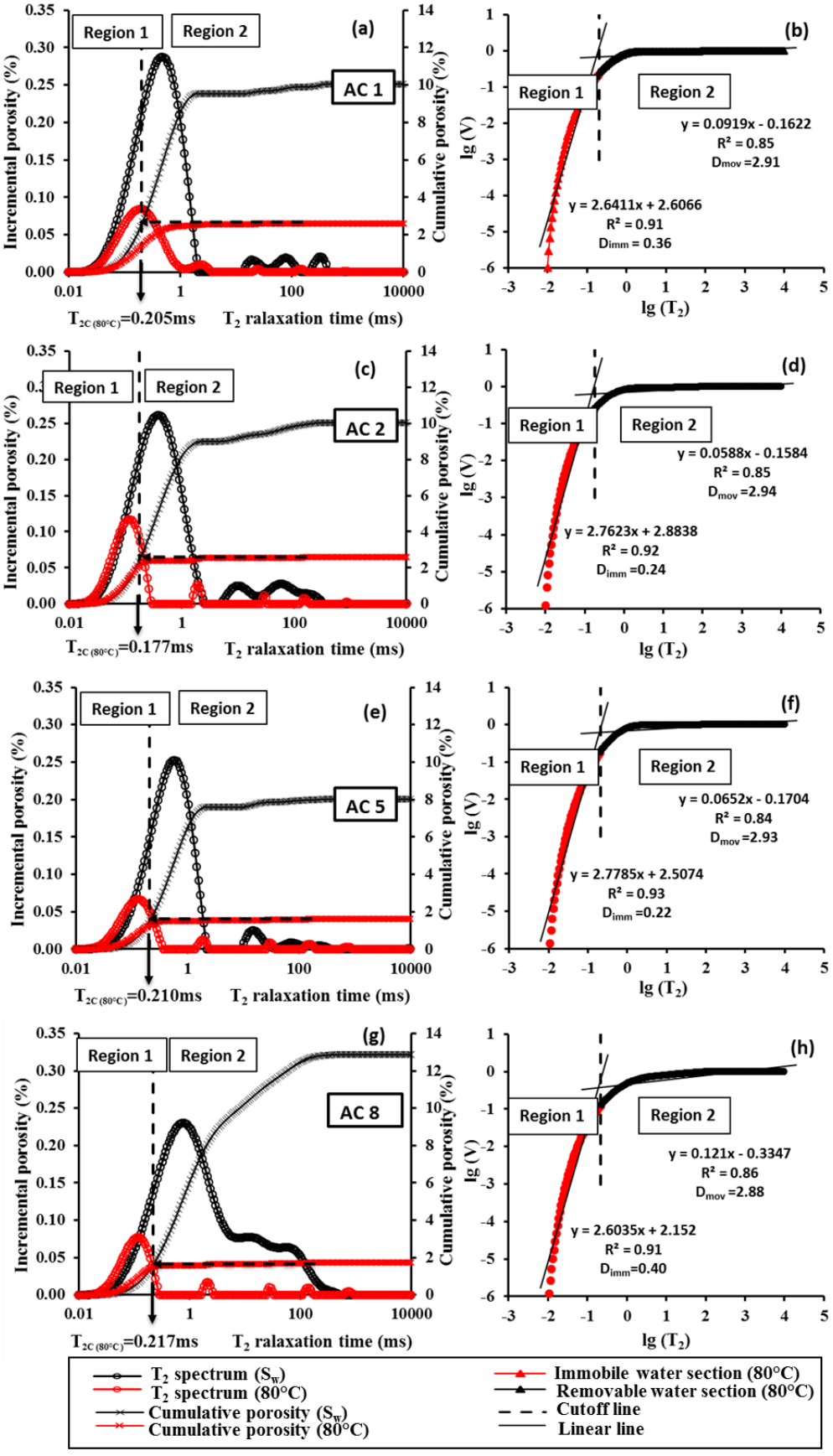

Figure 5. 5 Fractal analysis of Permian Carynginia shale samples, i.e., AC1, AC2, AC5, AC8, which were calculated based on NMR T_2 spectrum under 80°C pre-heated conditions.

Table 5. 2 The calculated fractal dimensions, i.e., D_{cbw} and D_{eff}, in Permian Carynginia shales under 80°C pre-heated treatment.

Name	Formation	Depth (m)	Region 1			T_2-cutoff	Region 2		
			K1	D_{cbw}	R_1^2		K2	D_{eff}	R_2^2
AC1	Carynginia	2780.20	2.64	0.36	0.91	0.205	0.09	2.91	0.85
AC2	Carynginia	2781.70	2.76	0.24	0.91	0.177	0.06	2.94	0.85
AC4	Carynginia	2794.40	2.70	0.30	0.90	0.170	0.11	2.89	0.82
AC5	Carynginia	2806.40	2.78	0.22	0.93	0.210	0.07	2.93	0.84
AC7	Carynginia	2816.70	2.62	0.38	0.93	0.255	0.04	2.96	0.82
AC8	Carynginia	2825.30	2.60	0.40	0.91	0.217	0.12	2.98	0.63
AC9	Carynginia	2831.30	2.53	0.47	0.94	0.195	0.01	2.95	0.84

5.3.2 Fractal analysis based on N_2 gas adsorption isotherm

The main mechanism of gas adsorption on pore surface involves the process of micropore filling and capillary condensation (Sahouli et al. 1997), corresponding to region 1 and region2, respectively (**Figure 5. 6**a, c, e, g). Taking AC1, AC2, AC5, AC8 as examples, as shown in **Figure 5. 6**, region 1 is consistent with mono-multilayer adsorption on smaller pores that is dominantly controlled by van der Waals attractive force (Khalili et al. 2000), while region 2 is predominated by capillary condensation in larger meso-/macropores (Yao et al. 2008, Bu et al. 2015). By fitting the adsorption isotherm data onto $\ln(\ln(P_0/P))$ - lnV coordinates, good linear relationships are observed in both regions (**Figure 5. 6**b, d, f, h). **Table 5. 3** presented the calculated results of all seven tested Permian Carynginia samples. The surface fractal dimension D1, which represents the roughness of micropore surface, ranges in 2.39-2.55. The volume fractal dimension D2, which demonstrates the complexity of meso/macropore volume (Zhou and Kang 2016, Sing 1985), varies in 2.57-2.68 (**Table 5. 3**).

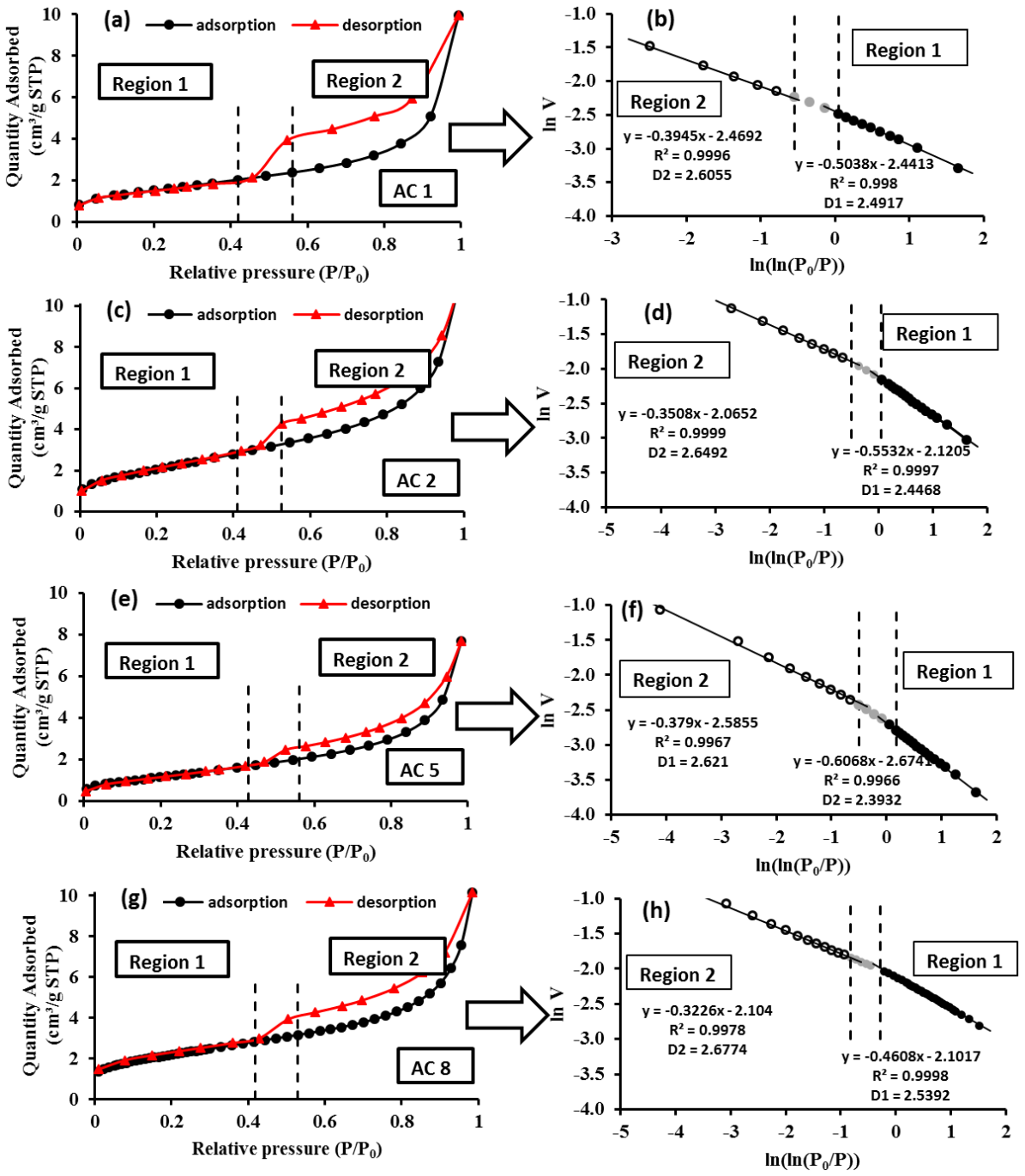

Figure 5. 6 Fractal analysis of Permian Carynginia shale samples, i.e., AC1, AC2, AC5, AC8, based on N_2 adsorption isotherm.

Table 5. 3 Fractal dimensions calculated from FHH model based on N_2 adsorption isotherm.

Name	Formation	Depth (m)	Region 1			Region 2		
			A1	D1	R_1^2	A2	D2	R_2^2

AC1	Carynginia	2780.20	-0.51	2.49	0.9980	-0.39	2.61	0.9996
AC2	Carynginia	2781.70	-0.55	2.45	0.9997	-0.35	2.65	0.9999
AC4	Carynginia	2794.40	-0.53	2.47	0.9913	-0.43	2.57	0.9951
AC5	Carynginia	2806.40	-0.61	2.39	0.9966	-0.38	2.62	0.9967
AC7	Carynginia	2816.70	-0.47	2.53	0.9995	-0.36	2.64	0.9987
AC8	Carynginia	2825.30	-0.46	2.54	0.9998	-0.32	2.68	0.9978
AC9	Carynginia	2831.30	-0.45	2.55	0.9997	-0.32	2.68	0.9992

5.3.3 Correlations of fractal dimensions from NMR and LP-N_2-GA

As shown in **Figure 5. 7**, positive linear relationships are shown in NMR-based D_{cbw} versus D1 (**Figure 5. 7**a; R^2= 0.91) and NMR-based D_{eff} versus D2 (**Figure 5. 7**ab; R^2= 0.81), indicating the intimate connections of CBW with micropore surface fractal and effective porosity with meso/macropore pore volume fractal. This novel observations perform a significant implication for evaluating shale gas storage based on fractal dimension. Section 3.4 further discusses the impact of micropore surface fractal on CBW and the influence of meso-/macropore volume fractal on shale gas storage in potential.

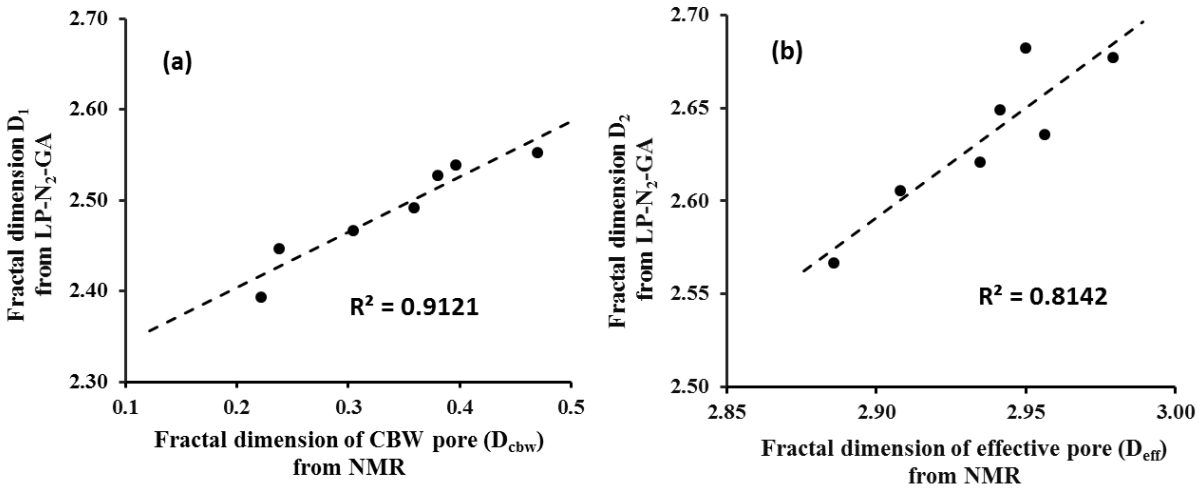

Figure 5. 7 Cross-plot of (a) NMR-based D_{cbw} and LP-N_2-GA-derived D1; (b) NMR-based D_{eff} and LP-N_2-GA-derived D2.

Based on the correlations above, we can explain the variations of D_{imm} and D_{mov} against temperatures in **Figure 5. 4**. D_{imm}, performing as the surface dimension associated with the immobile water under the given temperature, represents the overall roughness of small pore surface on which the immobile water is adsorbed. D_{imm} tends to represent the outline of water aggregates (Tang et al. 2003, Sun et al. 2016) as the immobile water molecules adsorb more than one layer and aggregate as a whole on pore surface (Sing 1985). As shown in **Figure 5. 2**a-e, when temperature rises from 50°C to 80°C, molecular layers of immobile water on pore surface decreases continuously (**Figure 5. 2**a-d), causing the reductions in interpreted D_{imm} value. The smallest layer of immobile water on pore surface occurred at 80°C, exhibiting the flattest surface outline (**Figure 5. 2**e) that corresponds to the lowest D_{imm} value at 80°C. Meanwhile, volume dimension (D_{mov}), which represents the complexity and heterogeneity of pore volume in meso-/macropore range, corresponds to the behaviours of movable pore water. The water aggregates of movable pore water are continuously extracted by heating, inducing the reduction of fractal volume complexity. Moreover, clay conversion from smectite to illite (S-I) has been found between 80°C and 90°C in Permian Carynginia shales (Yuan et al. 2018b), we suspect the anomalous increases in D_{imm} and D_{mov} from 80°C to 90°C (**Figure 5. 4**) are caused by S-I conversion, while further research is required for confirmations.

5.3.4 The impact of pore heterogeneity on hydrocarbon storage capacity

Figure 5. 8a presents the correlation between CBW volume and D_{cbw}. The CBW volume (**Table 5. 4**), which was obtained by the author's previous research (Yuan et al. 2018b), is positively correlated with D_{cbw} (R^2=0.58; **Figure 5. 8**a). Meanwhile, effective porosity calculated by cutting CBW off NMR total porosity (Yuan et al. 2018b) shows a negative linear correlation with D_{cbw} (R^2=0.58; **Figure 5. 8**b). As indicated from these good correlations, the more immobile water layers bound on pore surfaces, the larger fractal roughness would be interpreted in micropore surface, which largely reduces effective porosity in complex shale pore structures. As the fractal behaviour of pore spaces were suggested to be highly related to pore water retention (Kravchenko and Zhang 1998, Bird et al. 2000, Zhang and Weller 2014), it is reasonable to reckon that CBW largely complicates the geometry of pore network and reduces pore connectivity by performing as a potential resistance for effective fluid flows in porous medium. The impact of clays on increasing CBW retention coupled with reducing effective porosity would largely influence shale petrophysical properties. Further, to investigate the influence of meso-/macropore volume complexity (D_{eff}) on potential gas storage

capacity, we established the correlation between D_{eff} and gas storage capacity. As shown in **Figure 5. 9**, D_{eff} and gas storage capacity display a positive linear correlation (R^2= 0.80), indicating a large impact of meso-/macropore volume complexity on shale gas storage in potential.

Table 5. 4 Petrophysical properties of Permian Carynginia shales. Note that the CBW and effective porosity is obtained based on NMR measurement under 80°C pre-treatment (Yuan et al. 2018b). The gas storage capacity data for Permian Carynginia samples were obtained from the previous publication (Labani 2014).

Name	Formation	Depth (m)	D_{cbw}	CBW (%)	Effective porosity (%)	D_{eff}	Gas storage capacity (scf/ton)
AC1	Carynginia	2780.2	0.36	2.62	7.44	2.91	119.17
AC2	Carynginia	2781.7	0.24	2.60	7.44	2.94	130.55
AC4	Carynginia	2794.4	0.30	2.54	8.12	2.88	99.56
AC5	Carynginia	2806.4	0.22	1.64	11.23	2.93	123.89
AC7	Carynginia	2816.7	0.38	3.02	6.87	2.96	N/A
AC8	Carynginia	2825.3	0.40	2.73	5.29	2.98	144.78
AC9	Carynginia	2831.3	0.47	2.95	6.31	2.95	118.21

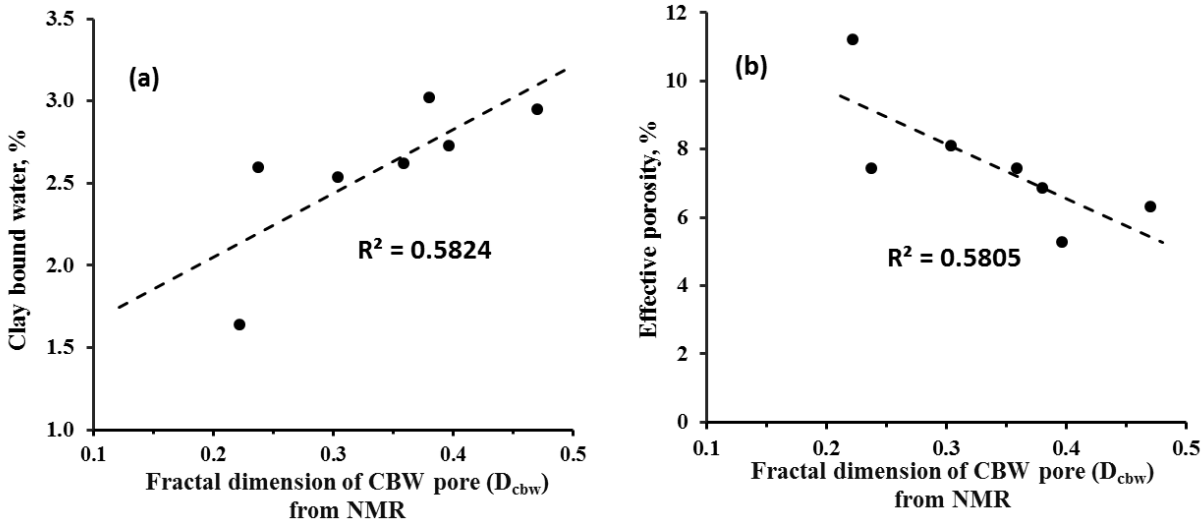

Figure 5. 8 The cross-plot of (a) NMR-based D_{cbw} v.s. the volume of CBW and (b) D_{cbw} v.s. effective porosity under the thermal pre-treatment of 80°C.

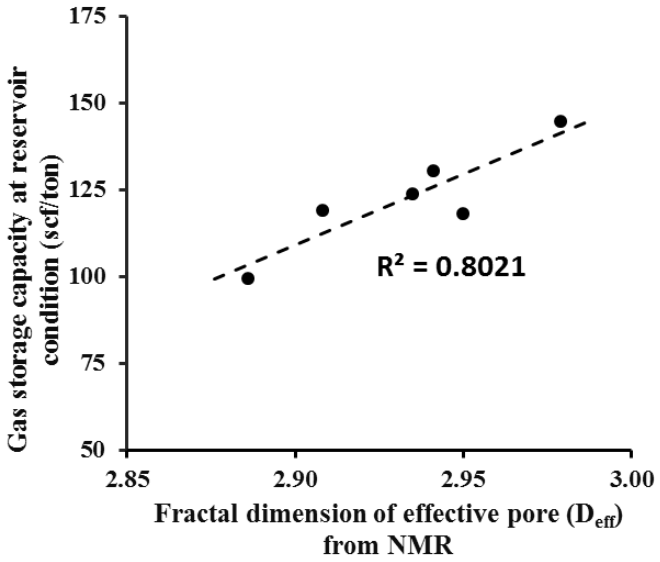

Figure 5. 9 The cross-plot of gas storage capacity v.s. NMR-based D_{eff}. Note that the gas storage capacity in Permian Carynginia shales is obtained from the previous publication (Labani 2014).

5.4. Conclusions

Conclusions can be summarized as follows:

- By comparing the fractal dimensions derived from NMR and LP-N_2-GA experiments, this study identified the fractal dimension of ineffective CBW pores (D_{cbw}) and effective pores (D_{eff}) in tight shale for the first time.

- D_{cbw} is intimate with micropore surface roughness, while D_{eff} is associted with meso-/macropore volume complexity.
- D_{cbw} and D_{eff} were calculated to be 0.22-0.47 and 2.88-2.98, respectively, in Permian Carynginia shales. D_{cbw} generally increases with the increasing CBW volume (1.64-3.02 %), while decreases with the increasing effective porosity (5.29-11.23 %). Higher D_{cbw} indicates more CBW adsorption on clay surfaces and less effective porosity in shales.
- D_{eff} increases with the increasing gas storage capacity (99.56-144.78 scf/ton) in Permian Carynginia shales. Larger D_{eff} indicates a more complicated pore volume with higher potential of shale gas storage.

CHAPTER 6 Impact of composition on pore structure properties in shale

This chapter consists of two published papers in *Energy & Fuels*.

Yuan, Y., Rezaee, R., Al-Khdheeawi, E., Hu, S.-Y., Verrall, M., Zou, J., and Kouqi, L., 2019, Impact of Composition on Pore Structure Properties in Shale: Implications for Micro-/Mesopore Volume and Surface Area Prediction: Energy & Fuel, 33, 9619-9628 (Yuan et al. 2019).

6.1. Introduction

The increasing demand for unconventional resources raises the necessity of shale reservoir investigation. Commercial shale gas production essentially relies on the estimation of gas storage capacity in complex pore structures (Labani et al. 2013, Rezaee 2015). In shale reservoirs, natural gas is stored in forms of free gas and adsorbed gas, which are largely controlled by pore structure parameters, i.e., pore volume, surface area, and pore size distribution (PSD), which are intimately associated with the pore types. The micropores and mesopores, defined as the pores smaller than 2 nm and the pores between 2 and 50 nm, respectively, by International Union of Pure and Applied Chemistry (IUPAC) (Rouquerol et al. 1994), exhibit large specific surface area and adsorption capacity. The micro-/mesopore system is documented to take the main control of shale gas storage (Chalmers et al. 2012, Keller et al. 2011, Zou et al. 2018), and significantly differs in shale formations that are highly heterogeneous in compositions such as organic matter (OM) and inorganic minerals (Curtis et al. 2012).

Black shale is widely acknowledged as the OM-rich sedimentary rocks that develop a majority of OM pores to control the micro-/mesopore volume and the total porosity during OM thermal maturation (Chalmers and Bustin 2007, Ross and Bustin 2009, Kuila et al. 2014b) (Milliken et al. 2013, Mastalerz et al. 2013, Liu et al.), and further influence the hydrocarbon storage and production capacity (Strapoc et al. 2010), the methane adsorption capacity (Zhang et al. 2012, Gasparik et al. 2014), and the mechanical properties (Prasad et al. 2011, Zargari et al. 2013). In OM-poor shales (e.g., Fort Simpson shales, Jurassic shales), pore structure properties exhibit very weak associations with organic matter (Ross and Bustin 2009). However, a comparable amount of gas storage capacity and pore volume (particularly the mesopore volume) could be alternatively provided by clay minerals (Gasparik et al. 2012, Kuila et al. 2014b, Schettler Jr and Parmely 1991, Zou et al. 2019, Ji et al. 2012, Yuan and Rezaee 2019a, Ross and Bustin 2009). As shale formations exhibit a high degree of heterogeneity in

mineralogical and geochemical composition, in most cases, shale pore structures are collectively contributed by mineral components and organic matter (Sondergeld et al. 2010a, Mastalerz et al. 2013, Furmann et al. 2016, Loucks et al. 2009, Loucks et al. 2012, Leu et al. 2016, Holmes et al. 2017). However, the quantification of mineral and OM contribution toward the pore structure properties (micro-/mesopore volume and surface area) are poorly understood. Moreover, it has not been fully clarified that which pore size ranges are dominantly controlled by mineral-related pores and which part is under the main charge of OM pores. Few quantitative studies have been carried out to differentiate the specific pore size range contributed by OM and mineral-related pores. Furthermore, the accurate prediction of micro-/mesopore structure properties is hindered by the lack of simple equations between micro-/mesopore parameters and shale compositions in large variation.

This article investigates the role of mineralogical and OM compositions on micro-/mesopore properties in shales from three different formations. We implemented quantitative analysis to estimate the influence of clay and TOC on micro-/mesopore volume, surface area, and PSD. New equations are established for the prediction of micro-/mesopore properties.

6.2. Materials and Methods

6.2.1. Shale samples

A total of 18 samples from three different formations were studied, taking considerations of the clay and TOC content. Eight samples by the name of 'AC' serials were collected from Permian Carynginia Formation of Perth Basin, Western Australia. Six samples by the name of 'GTh' serials were collected from Ordovician Goldwyer Formation of Canning Basin, Western Australia. Four samples by the name of 'Bak' serials were obtained from Bakken Formation of Williston Basin in North Dakota, USA and southern Saskatchewan, Canada. The detailed geological settings and wellbore backgrounds of the studied samples have been included in the authors' previous publications (Yuan et al. 2018c, Yuan and Rezaee 2019b, Yuan and Rezaee 2019d, Liu et al. 2018c, Yuan et al. 2018a).

6.2.2. X-Ray diffraction (XRD)

Samples were grounded and the mineralogy was analysed via XRD, a Bruker D8 Advance automated powder diffractometer with Bragg-Brentano configuration. A LynxEye sensitive detector and a copper X-ray tube have been employed in the experiment. Rock powders (~5g) were analyzed over an angular range of 7-120° 2θ with a normal step size of 0.015°. The

instrument was complemented with Bruker EVA software for search/match analysis and a comprehensive full pattern data analysis programme, TOPAS.

6.2.3. Rock-Eval pyrolysis

Rock-Eval pyrolysis was undertaken for organic geochemical analysis. Prior to measurements, the crushed shale samples with the weight of 60-80 mg were settled in stainless steel crucibles, with the fritted top and bottom to enable the oxidation channel of N_2 and air through the sample. Rock-Eval pyrolysis was then carried out on Rock-Eval VI® analyser (manufactured by Vinci® Technologies). The detailed procedures and parameters descriptions followed Lafargue et al. (Lafargue et al. 1998). Concisely, two-step-controlled heating progresses were included. Samples were initially pyrolyzed under an inert N_2 environment and the residual carbon is subsequently burnt in an oxidation oven. S1 peak (mg HC/g) was recorded on pyrogram corresponding to the thermos-vaporized free-hydrocarbons during pyrolysis process under inert N_2 atmosphere. S2 peak (mg HC/g) was recorded resulting from the thermal cracking of heavier and long chain hydrocarbons for the remaining hydrocarbon potential. The method was finalized by combustion (oxidation) of the residual fragments recovered after pyrolysis. S3 represents the carbon dioxide amount evolved from breaking carboxyl groups and other oxygen-containing compounds in kerogen, obtained at 300–390 °C.

TOC content, which represents the richness of organic matter, is derived from two fractions: (1) the convertible fraction, which represents the hydrocarbons already generated (S1) and the hydrocarbons potential (S2); (2) the residual fraction that is oxidized dead carbon and does not contain potential to generate hydrocarbons. Kerogen type is determined by plotting the hydrogen index (HI) versus oxygen index (OI) on pseudo van Krevelen diagram (Tissot et al. 1974). HI (S2 × 100/TOC, mg HC/g TOC) is the normalized hydrogen content remaining in source shales, while OI (S3 × 100/TOC, mg CO_2/g TOC) is the normalized oxygen content presenting in kerogen.

6.2.4. Kerogen isolation

To separately investigate the impact of organic matter and clay minerals on pore structure properties, we extracted organic matter from bulk shales. However, our Rock-Eval results indicate that OM from Carynginia and Goldwyer shales is too limited to be properly extracted from the rocks. We thus carried out only kerogen isolation from the Bakken shales, following the chemical approach of acid demineralization procedures: (1) pre-acid preparation; (2) bitumen removal using Soxhlet extraction; (3) carbonates elimination using HCl solution; (4)

silicate exclusion using HF solution; (5) pyrite removal using $CrCl_2$ (Goklen et al. 1984, Liu et al. 2018c, Acholla and Orr 1993).

6.2.5. Low-pressure gas adsorption

Low-pressure (<18.4 psia) gas adsorption (LP-GA) was conducted to characterize pore size distribution (PSD), pore volume and surface area. Prior to measurements, shale fragments were grounded into 100-60 mesh (150-250 μm) and degassed over 8 h for pore surface cleaning. LP-N_2-GA was performed on Micromeritics® TriStar 3020 instrument at the bathing temperature of 77.4 K to access the pores ranging between 2 and 200 nm. N_2 adsorption isotherm was interpreted using density functional theory (DFT) (Seaton and Walton 1989, Lastoskie et al. 1993) and Brunauer-Emmett-Teller (BET) model (Barrett et al. 1951) for the determination of PSD and surface area, respectively.

LP-CO_2-GA was conducted on Micromeritics® TriStar Plus apparatus under 273.1 K for the characterization of micropores ranging from 0.35 to 2 nm. CO_2 adsorption branch was interpreted via nonlocal density functional theory (NLDFT) and Dubinin-Astakhov model (Dubinin and Astakhov 1971) to obtain the PSD (Neimark et al. 2009) and micropore volume, respectively. Note that all interpretations were performed on TriStar II 3020 embedded standard software. The pore size categorization and terminology used in this study follows the standard of IUPAC (Rouquerol et al. 1994).

6.3. Results and discussion

6.3.1. Shale composition

Mineralogical composition of the studied samples is shown in **Figure 6. 1** and **Table 6. 1**. The clay (dominantly illite) and quartz constitute the mineral majority in Carynginia, Goldwyer and Bakken shales. Goldwyer shales are characterized by the highest value of clay content, when compared with Carynginia and Bakken shales (i.e., the clay content of Goldwyer, Carynginia and Bakken ranges in 58-83, 31-50, and 16-28 wt %, respectively, with the mean value of 71.9, 36.6, and 21.4 wt %).

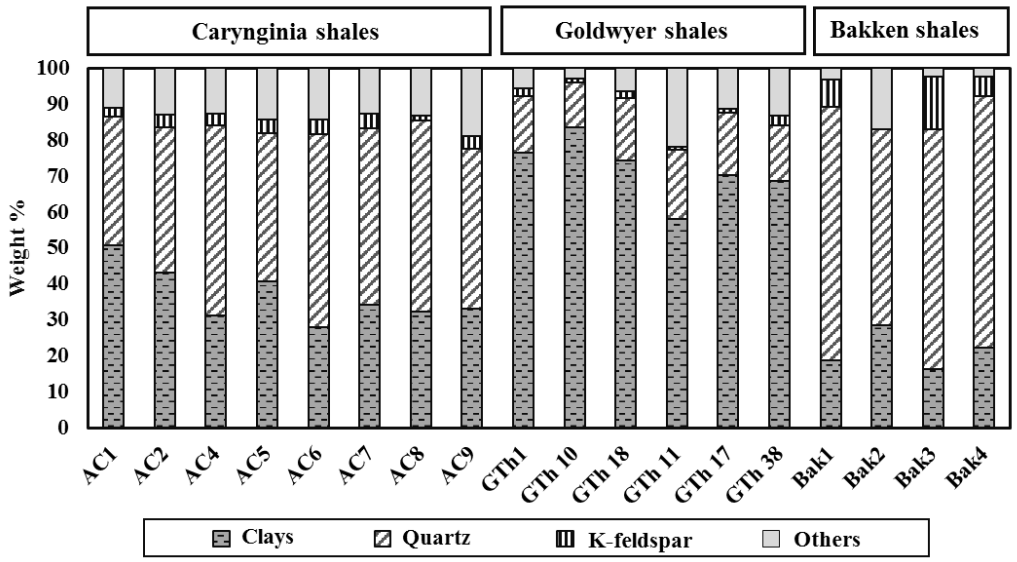

Figure 6. 1 XRD mineralogical composition for Carynginia, Goldwyer and Bakken shales (specific values are shown in appendix **Table 6. 1**).

Table 6. 1 XRD mineralogical composition and geochemial parameters for Carynginia, Goldwyer and Bakken shales. Some of the data have been published in previous studies (Yuan et al. 2018c, Liu et al. 2018c).

Name	Formation	Depth (m)	Quartz (wt %)	Feldspar (wt %)	Clay mineral contents (wt %)				Other minerals (%)	TOC (%)	HI	OI
					Mixed illite, illite/muscovite, trace smectite	Chlorite	Kaolinite	Total clay				
AC1	Carynginia	2780.20	35.60	2.60	39.80	5.80	5.20	50.80	11.00	3.03	64	5
AC2	Carynginia	2781.70	40.30	3.60	33.70	4.90	4.60	43.20	12.90	1.79	36	16
AC4	Carynginia	2794.40	53.00	3.30	27.20	3.10	0.80	31.10	12.60	0.64	39	27
AC5	Carynginia	2806.40	41.30	3.60	34.70	5.20	0.80	40.70	14.40	1.82	63	2
AC6	Carynginia	2812.50	53.80	4.00	24.50	2.90	0.50	27.90	14.30	1.08	48	8
AC7	Carynginia	2816.70	49.20	4.00	28.40	4.80	0.90	34.10	12.70	1.36	55	7
AC8	Carynginia	2825.30	53.20	1.40	27.90	2.70	1.80	32.30	13.10	0.77	69	70
AC9	Carynginia	2831.30	44.50	3.60	27.60	4.30	1.20	33.10	18.80	0.23	64	88
GTh1	Goldwyer	1201.98	15.68	2.23	71.14	3.91	1.53	76.58	5.51	0.30	78	57
GTh 10	Goldwyer	1390.82	12.42	1.24	67.45	14.50	1.54	83.49	2.85	1.26	193	22
GTh 11	Goldwyer	1397.80	19.34	0.72	41.26	13.75	3.02	58.03	21.91	4.28	333	8
GTh 17	Goldwyer	1472.13	17.42	1.02	55.79	10.99	3.43	70.21	11.35	3.91	254	7
GTh 18	Goldwyer	1473.38	17.39	1.78	61.27	5.87	7.14	74.28	6.55	3.20	236	16
GTh 38	Goldwyer	1557.25	15.46	2.71	60.52	4.49	3.69	68.70	13.13	2.68	268	12
Bak1	Bakken	8387.00	70.30	7.70				18.81	3.19	14.19	313	3
Bak2	Bakken	9814.00	54.30	0.00				28.60	17.10	20.17	556	2
Bak3	Bakken	9881.00	66.90	14.40				16.20	2.50	11.07	479	2
Bak4	Bakken	9889.00	70.00	5.50				22.20	2.30	12.22	464	2

The organic geochemical properties are displayed based on Rock-Eval pyrolysis results (**Table 6. 1**). Bakken shales exhibit the highest TOC content, followed by Goldwyer and Carynginia (i.e., the TOC content of Bakken, Goldwyer and Carynginia ranges 11.07-20.17%, 0.98-4.28%, and 0.23-3.03%, respectively). **Figure 6. 2** presents S2 versus TOC content for the evaluation of hydrocarbon generative potential. The sloped dashed lines separate the plot into 5 regions by various HI values (i.e., HI ranges in >700, 350-700, 200-350, 50-200 and <50 mg HC/g TOC), which correspondingly match with 5 different organic matter types. Carynginia, Goldwyer and Bakken shales were classified as Type Ⅲ (gas prone), Type Ⅱ/Ⅲ (oil/gas prone) and Type Ⅱ (oil prone), respectively, consistent with the previous studies(Thomas and Barber 2004, Triche and Bahar 2013, Liu et al. 2018c).

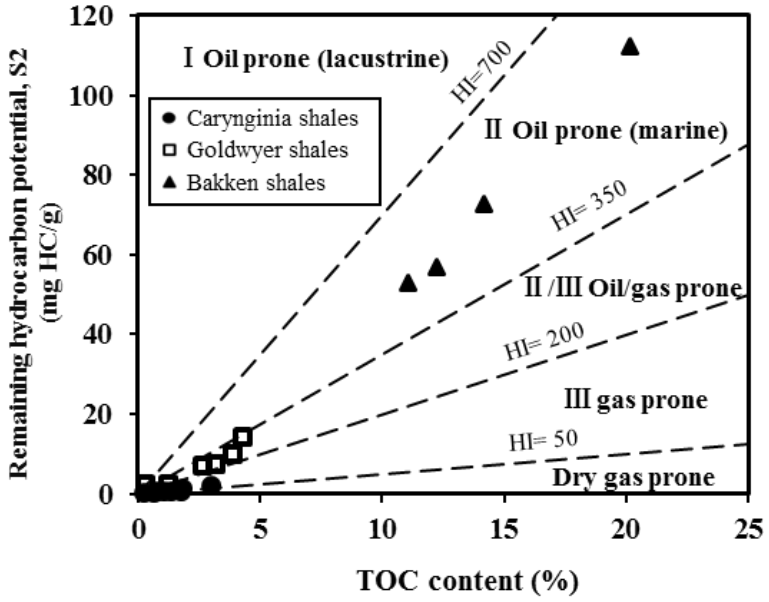

Figure 6. 2 The plot of remaining hydrocarbon potential (S2) versus TOC content. (modified from Langford and Blanc-Valleron (Langford and Blanc-Valleron 1990))

6.3.2. Effect of TOC and clay contents on adsorption isotherm

Figure 6. 3 presents the adsorption isotherms for the micro-/mesopores. Six samples are displayed in **Figure 6. 3**a,b as the representatives for discussion. The other samples, which exhibit similar trends, are demonstrated in **Figure 6. 3**c,d. As shown in **Figure 6. 3**a, the organic-rich Bakken samples (e.g., Bak1, Bak4) yield the highest CO_2 isotherm curves in parallel with the largest adsorption amount, which are subsequently followed by Goldwyer (e.g., GTh 17 and GTh 38) and Carynginia shales (e.g., AC6 and AC9). The micropore

adsorption amount, which exhibits an intimate relationship with TOC content, reduces with the decreasing value of TOC content in tested samples.

Figure 6. 3b provides the N_2 adsorption isotherm for mesopores. The clay-rich Goldwyer (e.g., GTh17 and GTh 38) exhibits the highest adsorptions compared to Carynginia (e.g., AC9 and AC6) and Bakken shales (e.g., Bak4 and Bak1), indicating that there is a close association between the clay content and mesopore adsorptions.

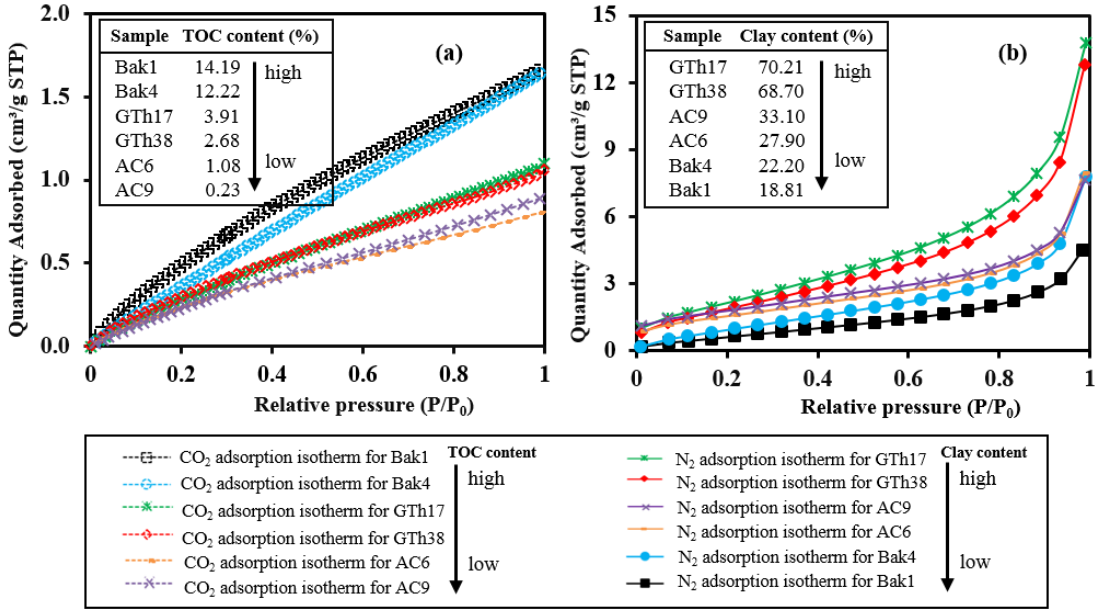

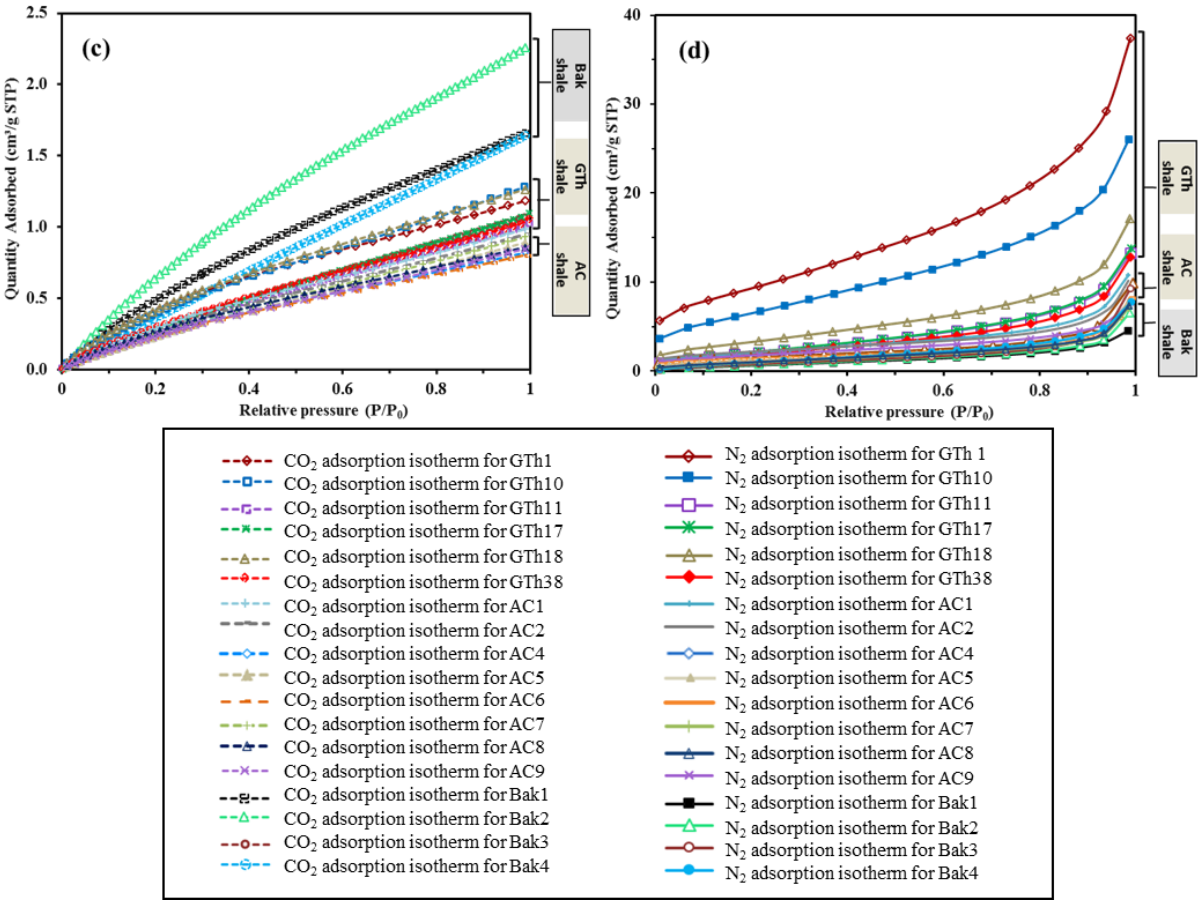

Figure 6. 3 (a,c) Low-pressure CO_2 gas adsorption isotherms and (b,d) low-pressure N_2 gas adsorption isotherms for the studied shale samples.

3.3. Effect of TOC and clay contents on pore size distribution

Figure 6. 4 shows the pore size distribution (PSD) of the studied samples. To separately showcase the pore structures within the isolated kerogens and minerals, the PSDs of Bakken bulk shale are compared with their isolated kerogens, which were normalized by the weight of organic content in bulk shale (i.e., defined as 1 g × TOC).

As the examples shown in **Figure 6. 4**, significant variations are found in the PSD of the mesopores ranging from 2nm to 17nm (mesoPSD$_{2\text{-}17nm}$). The clay-rich Goldwyer (e.g., GTh 17 and GTh 38) exhibits a strikingly larger pore volume proportion in mesoPSD$_{2\text{-}17nm}$ (**Figure 6. 4**a, b) compared to Carynginia and Bakken shale samples (**Figure 6. 4**c-f). Comparing the PSD of the bulk Bakken shales and their isolated kerogens, a tremendous gap is discovered in the mesoPSD$_{2\text{-}17\ nm}$ (**Figure 6. 4**e-h). As clay mineral performs as the main mineral contributor to the pore space in shales, the decrease of the pore volume in mesoPSD$_{2–17nm}$ is supposed to be caused by the demineralization of clays. The microPSD, however, exhibits a high consistency

before and after demineralization (e.g., **Figure 6. 4**e-h), indicating a deficiency of the mineral pores in the micropore size ranges. By contrast, organic matter pores are intimately associated with the micropores, which is consistent with other research studies (King Jr et al. 2015). Further, the PSD differences between bulk shales and isolated kerogens are also identified in the pore size ranges larger than 17 nm ($PSD_{>17nm}$). As shown in **Figure 6. 4**e-h, the $PSD_{>17nm}$ in isolated kerogen (e.g., Bak 1, Bak2, Bak3, and Bak4) displays large remaining section after demineralization, which indicates a collective impact of clay and organic matter on the pore sizes larger than 17 nm. The normalized kerogen of Bak1, however, exclusively exhibits an increased pore volume in $PSD_{>17nm}$ (**Figure 6. 4**e), which could possibly be explained by the fact that that there are some organic matter pores that are initially filled with minerals would be exposed after demineralization, thus leading to the enlarged pore volume in isolated kerogen (Liu et al. 2018c).

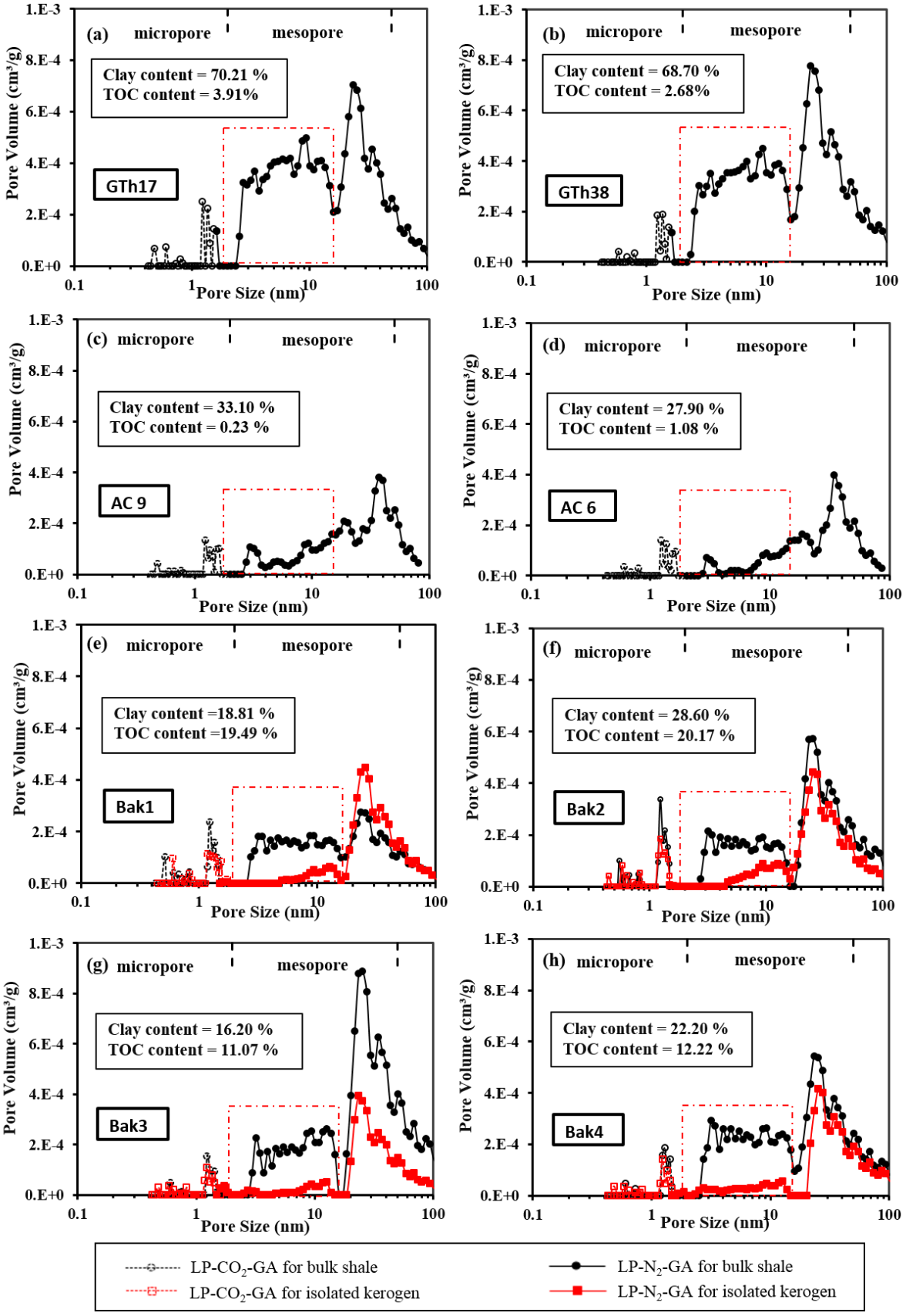

Figure 6. 4 The pore size distribution derived from LP-GA measurement in the tested shale samples.

6.3.4. Effect of TOC and clay contents on pore volume

To study the effect of the TOC and clay contents on pore volume, we measured the pore volume of the microspores and the mesopores ranging from 2 to17 nm for three different formations. The results show that Bakken shales have the highest micropore volume, followed by Goldwyer and Carynginia shales (e.g. the average micropore volume of the Bakken, Goldwyer and Carynginia shales is 0.39, 0.21, and 0.07 $cm^3/100$ g, respectively). However, the highest value of mesopore volume was found in Goldwyer compared to the other two shales (e.g. the average mesopore volumes of Goldwyer, Bakken, and Carynginia shales are 1.17, 0.42, and 0.41 $cm^3/100$ g, respectively).

As shown in **Figure 6. 5**a, a positive linear correlation is found between microspore volume and TOC content in Bakken shales (R^2 = 0.96), while weaker correlations are displayed in Carynginia and Goldwyer. Interestingly, different scenarios are observed between mesopore volume and clay content (**Figure 6. 5**b). Mesopore volume displays strong positive linear relationships with clay contents in Carynginia (R^2 = 0.98) and Goldwyer (R^2 = 0.88), while no correlations are observed in Bakken shales. The cross-plots of the microspore volume versus clay content, and the mesopore volume versus TOC content, which exhibit no obvious correlations for three formations, have not been reckoned for discussion.

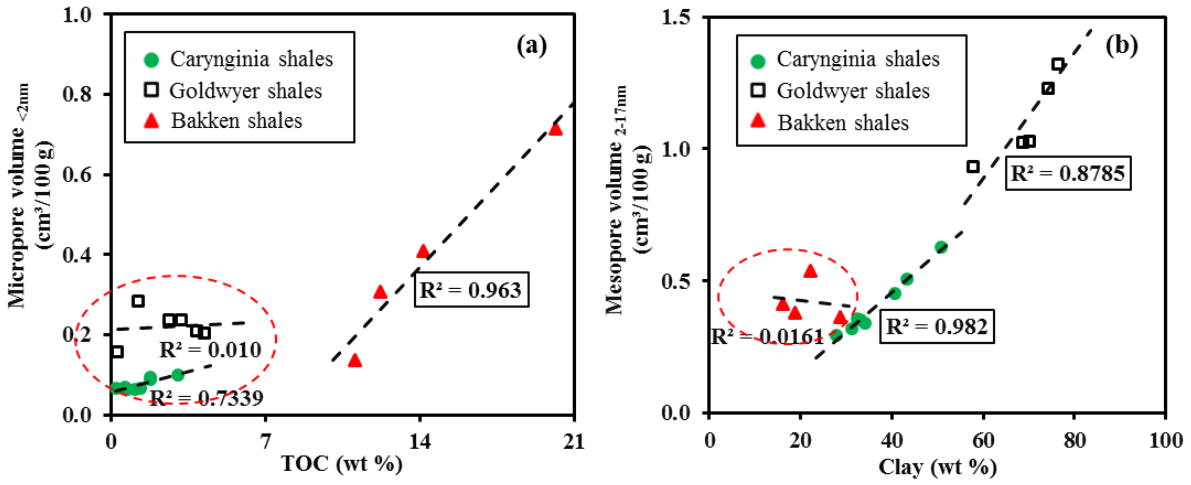

Figure 6. 5 Corretions between (a) microspore volume and TOC content; (b) mesopore volume and clay content for three shale formations.

6.3.5. Effect of TOC and clay contents on surface area

The surface area of microspores and the mesopores$_{2\text{-}17nm}$ have been interpreted for three different formations. The highest micropore surface area values are displayed in Bakken compared to Carynginia and Goldwyer, averaging 2.03, 1.52, and 1.51 m²/g, respectively. The mesopore surface area values, by contrast, are highest in Goldwyer (avg. 12.48 m²/g), which is around three-fold as that in the other two shales (e.g., Carynginia and Bakken average in 4.55 and 3.75 m²/g, respectively).

By correlating micropore surface area and mesopore surface area with the clay and TOC content (**Figure 6. 6**a), we observed strong positive correlations between micropore aurface area and TOC content in Bakken (R^2 = 0.89), while good but weaker correlation coefficients are shown in Goldwyer (R^2 = 0.69) and Carynginia (R^2 = 0.65). Conversely, mesospore surface area is strongly positive correlated with clay contents in Carynginia (R^2 = 0.89) and Goldwyer (R^2 = 0.83), while no obvious correlations are demonstrated in Bakken shales. The cross-plot of micropore surface area versus clay and the mesopore surface area versus TOC for three formations, which display disordered relationships, has not been showcased for discussion.

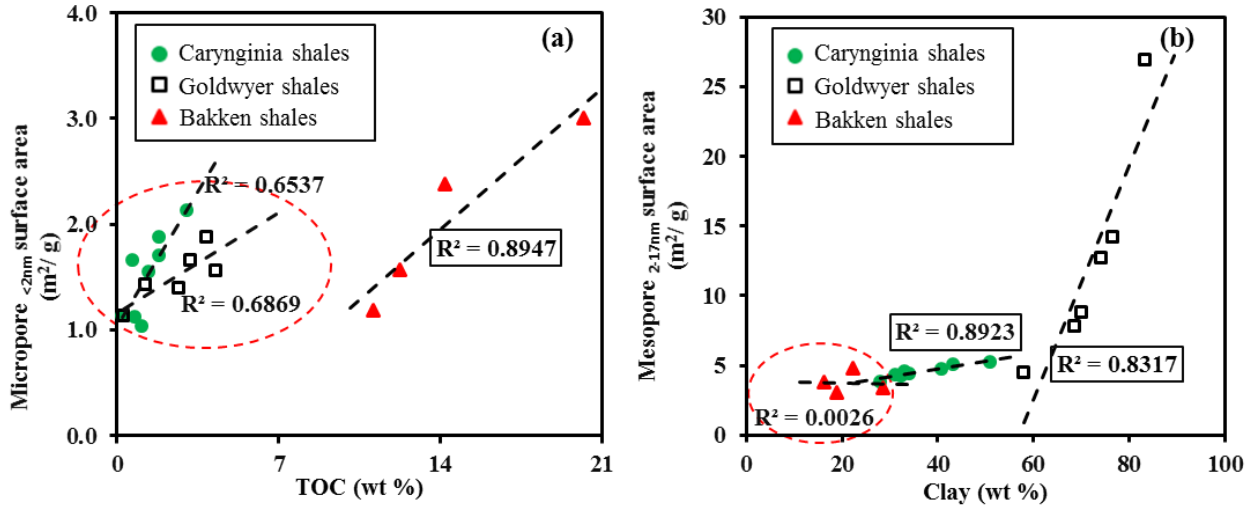

Figure 6. 6 Corretions between (a) microspore surface area and TOC content; (b) mesopore surface area and clay content for three shale formations.

6.3.6. New correlations for predicting microstructural pore parameters

To quantify the effect of clay and TOC contents on the pore structure parameters, here, we have developed four new correlations for predicting the pore structure parameters (i.e. micropore volume, mesopore volume, micropore surface area, and mesopore surface area) as a function of clay and TOC contents. The multiple regression method has been applied to

develop these new correlations using the data collected from three different shale formations. The following correlations represent the best regression analysis obtained:

$$\textit{Micropore volume } (cm^3/100\ g) = -0.11 + 0.004\ V_{clay} + 0.03\ TOC \quad \ldots\ldots (6.1)$$

$$\textit{Mesopore volume } (cm^3/100\ g) = -0.26 + 0.02\ V_{clay} + 0.02\ TOC \quad \ldots. (6.2)$$

$$\textit{Micropore surface area } (m^2/g) = -0.38 + 0.07\ V_{clay} + 0.04\ V_{clay}^2 + 0.002\ TOC^2 \quad \ldots..(6.3)$$

$$\textit{Mesopore surface area } (m^2/g) = -8.12 + 0.36\ V_{clay} + 1.38\ TOC - 0.05\ (V_{clay} \times TOC) \ldots..(6.4)$$

where V_{clay} is clay content (wt %) and TOC is total organic carbon content (wt %). The range of input and output variables are summarized in **Table 6. 1**. To check the accuracy of our established new correlations, the output data for prediction were compared with the experimental results that were used in the establishment of the new equations. The correlation coefficient (R^2) for the new correlations was 0.88 for *Micropore volume* correlation (Eq. 6.1), 0.92 for *Mesopore volume* correlation (Eq. 6.2), 0.73 for *Micropore surface area* correlation (Eq. 6.3) and 0.78 for *Mesopore surface area* correlation (Eq. 6.4). The statistical analysis above reveals high values of the correlation coefficient, indicating the acceptable accuracy of our developed correlations. Furthermore, **Figure 6. 7**, **Figure 6. 8, Figure 6. 9, and Figure 6. 10** cross-plot the experimentally measured pore parameters versus those determined from new correlations (Eqs. 6.1-6.4). The good demonstrated agreements suggest that our proposed correlations are able to predict the microstructural pore parameters in our investigated shale formations with acceptable accuracy.

Table 6. 2 The range of data, which are used for developing the new correlations, based on LP-GA measurements of 14 shale samples.

Parameters	Minimum	Maximum	Mean
Micropore volume ($cm^3/100g$)	0.063	0.714	0.194
Mesopore volume ($cm^3/100g$)	0.294	1.505	0.665
Micropore surface area (m^2/g)	1.126	3.004	1.634
Mesopore surface area (m^2/g)	3.044	26.896	7.025
TOC (wt %)	0.30	12.22	4.67
Clay content (wt %)	16.20	83.49	45.02

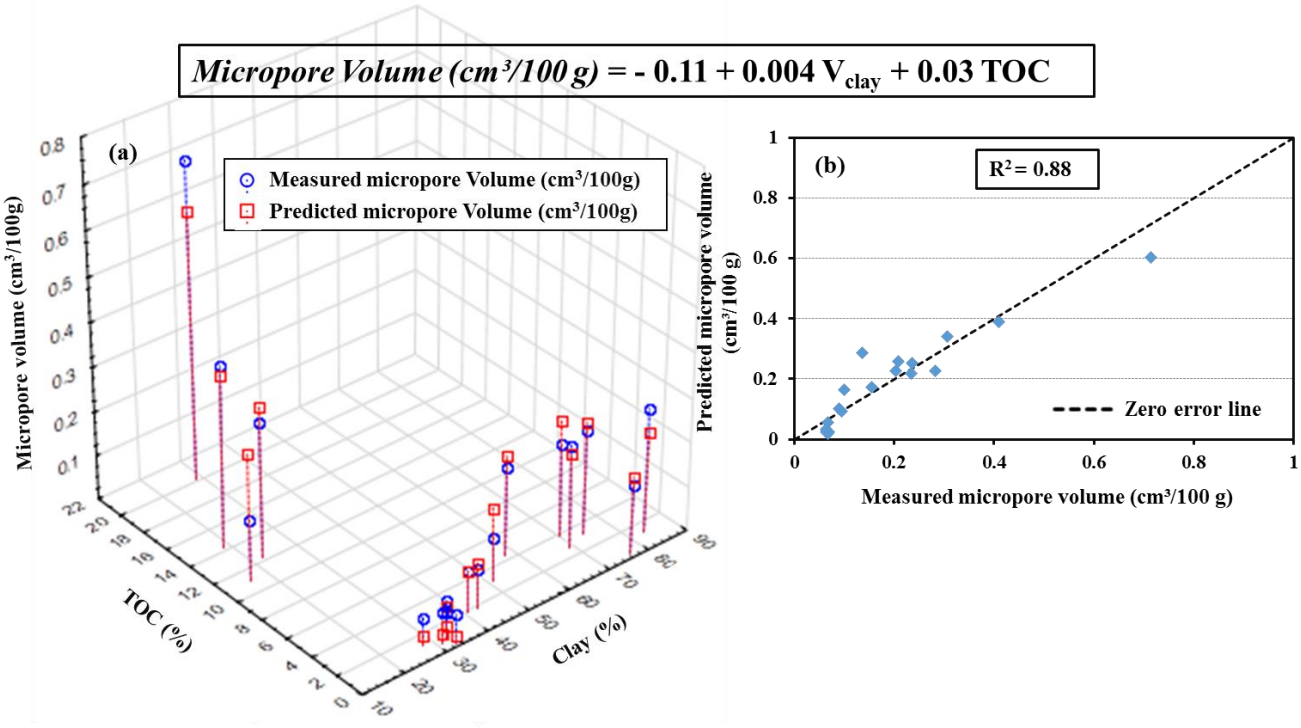

Figure 6. 7 (a) 3D scatter plot showing the relationship between the predicted and measured micropore volume with shale compositions (i.e., clay and TOC content). (b) 2D cross-plot of the measured and predicted micropore volume from the newly developed correlation Eq. 6.1.

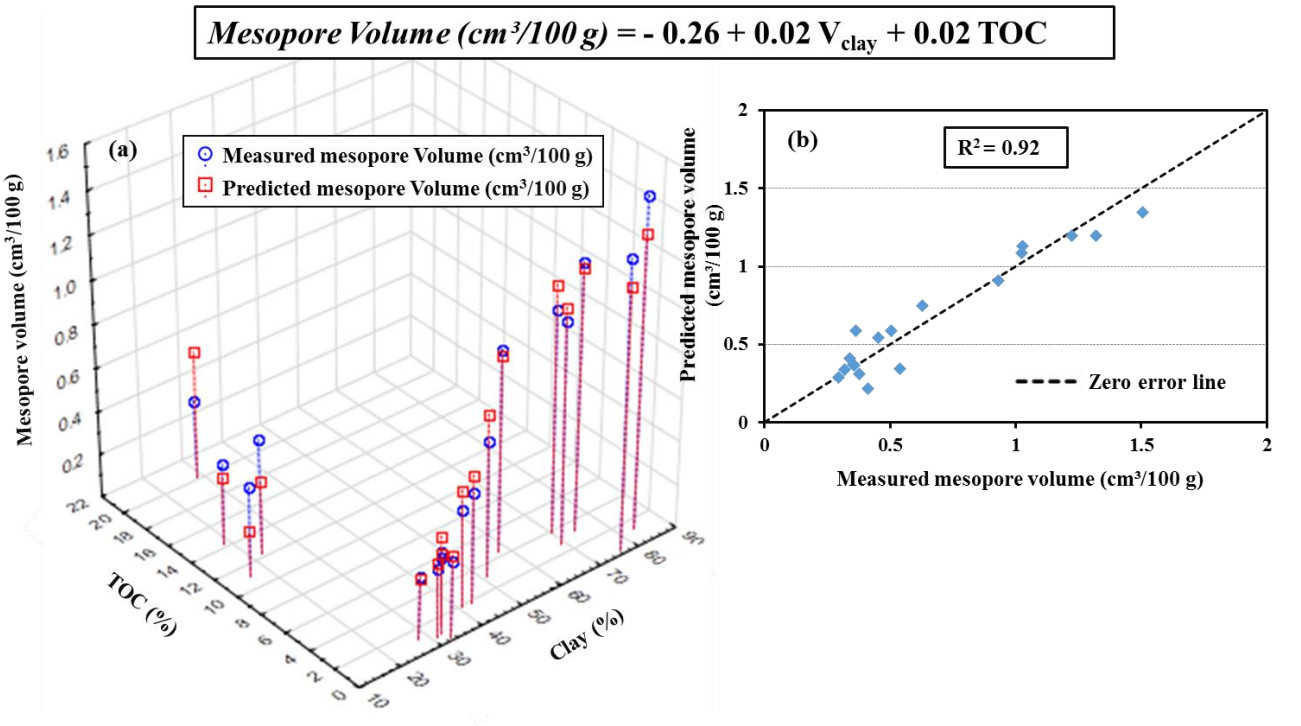

Figure 6. 8 (a) 3D scatter plot showing the relationship between the predicted and measured mesopore volume with shale compositions (i.e., clay and TOC content). (b) 2D cross-plot of the measured and predicted mesopore volume from the newly developed correlation Eq. 6.2.

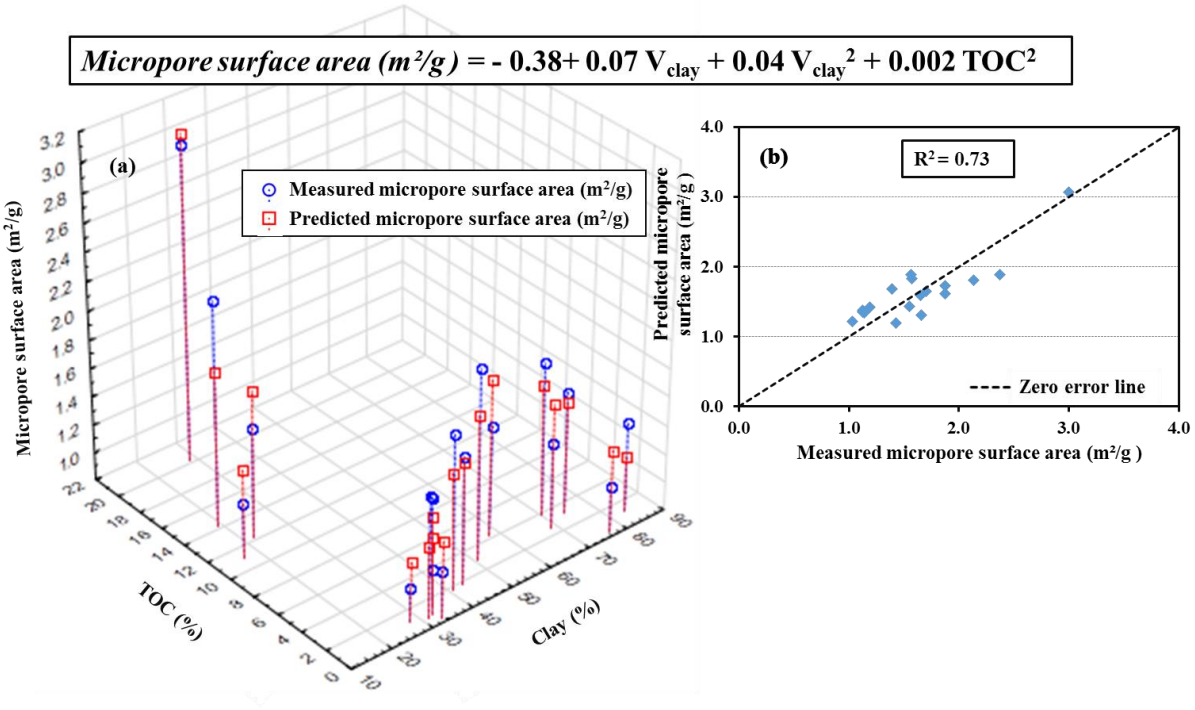

Figure 6. 9 (a) 3D scatter plot showing the relationship between the predicted and measured micropore surface area with shale compositions (i.e., clay and TOC content). (b) 2D cross-plot of the measured and predicted micropore surface area from the newly developed correlation Eq. 6.3.

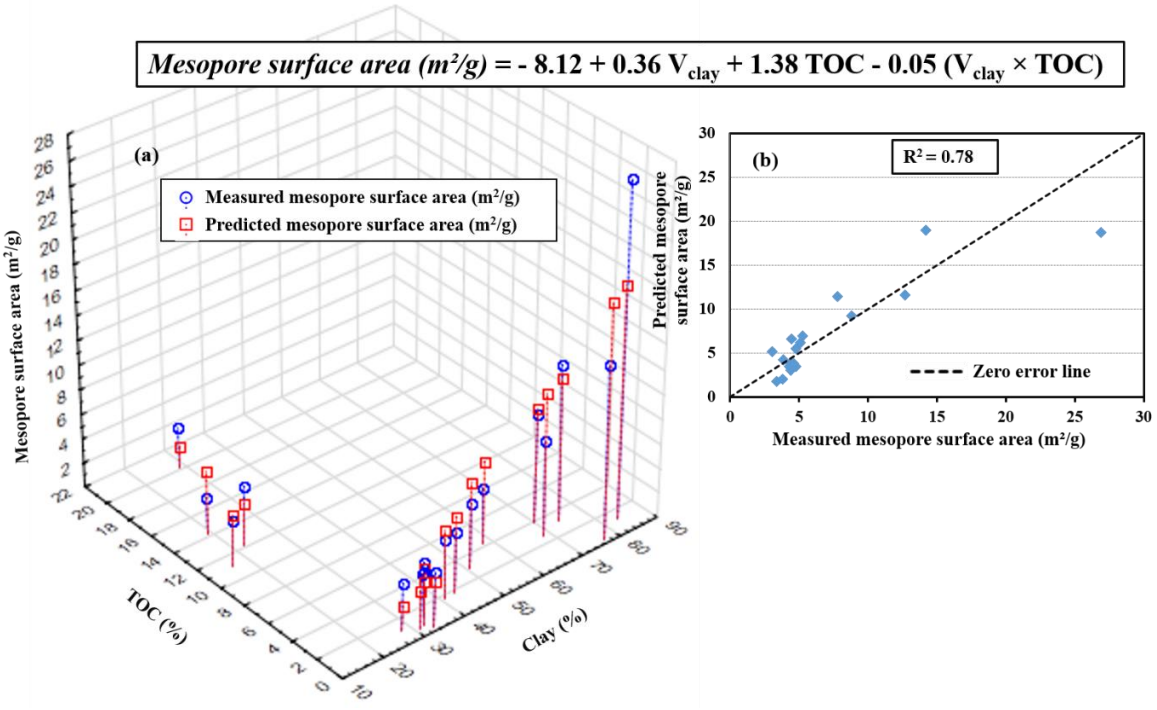

Figure 6. 10 (a) 3D scatter plot showing the relationship between the predicted and measured mesopore surface area with shale compositions (i.e., clay and TOC content). (b) 2D cross-plot of the measured and predicted mesopore surface area from the newly developed correlation Eq. 6.4.

6.4. Conclusions

The micro-/mesopore structure in Carynginia (Western Australia), Goldwyer (Western Australia), and Bakken (both North Dakota, USA and southern Saskatchewan, Canada) formations are jointly influenced by mineralogical and organic geochemical properties. The micropores are more intimately correlated with organic matter pores, whose micropore volume and micropore surface area can be quantified using the newly developed Eq. 6.1 and Eq. 6.3, respectively. The mesopores in 2-17 nm are predominately controlled by clay (dominantly illite) pores, whose mesopore volume and mesopore surface area can be quantified using the newly developed Eq.2 and Eq.4.

CHAPTER 7 Impact of paramagnetic minerals on NMR-converted pore size distributions in Permian Carynginia shales

This chapter is a published paper in *Energy & Fuels*.

Yuan, Y., and R. Rezaee, 2019b, Impact of paramagnetic minerals on NMR-converted pore size distributions in Permian Carynginia shales: Energy & Fuels, 33, 2880-2887. (Yuan and Rezaee 2019d)

7.1. Introduction

Petrophysical analysis is a significant task for hydrocarbon estimation in unconventional shales. The essential shale pore structure properties, i.e., pore size distribution (PSD), porosity, pore volume and specific surface area (SSA), vary significantly from that in conventional reservoirs (Rezaee 2015, Loucks et al. 2012, Mastalerz et al. 2013). The reliable and accurate pore structure interpretations via the combination of techniques are greatly required to evaluate hydrocarbon storage capacity and fluid transportation rate in complex pore networks (Leu et al. 2016, Rezaee et al. 2012). Apart from the image quantifications, e.g., scanning electron microscopy/ transmission electron microscopy (SEM/ TEM) (Milliken et al. 2013, Chalmers et al. 2012, Loucks et al. 2012), and the scattering techniques, e.g., small-angle neutron scattering/ ultrasmall-angle neutron scatting (SANS/ USANS) (Clarkson et al. 2012b, Clarkson et al. 2013, Mastalerz et al. 2012), the use of fluid penetration approaches (e.g., mercury injection capillary pressure (MICP), nuclear magnetic resonance (NMR), and low-pressure gas adsorption (LP-GA) (Rezaee et al. 2012, Nelson 2009, Yuan et al. 2018c, Al Hinai et al. 2014, Chalmers et al. 2012, Fleury and Romero-Sarmiento 2016, Labani et al. 2013, Yuan et al. 2018a, Testamanti 2018)) is also significant in shale pore structure characterization. Consistent interpretations have been revealed between different penetrating techniques in conventional reservoirs. However, discrepancies are presented in shales due to the limited accessibility of working fluids into pore structure that is characterized by nanometer-scaled pore size, the extremely low permeability, the fine-grained tight texture and the impact of abundant clay minerals and clay bound water (Saidian et al. 2016, Topór et al. 2016, Yuan et al. 2018c, Yuan and Rezaee 2019b) .

MICP, which has been effectively applied in pore structure evaluation of sandstones and carbonates, involves large limitations in shale characterizations. Porosity underestimation

would be induced by incomplete mercury intrusion in tight texture (Kuila et al. 2014a), meanwhile, the high-pressure application would most likely compress pore volume in rock framework, break particles and potentially open the closed pores in shale formations (Bustin et al. 2008, Kuila and Prasad 2013). The destructive and uneconomic characteristics involved in MICP largely restrict its application (Yao and Liu 2012). Comparably, NMR, which is acknowledged as a nondestructive technique, is beneficial for obtaining petrophysical pore structure parameters. The NMR-interpreted PSD and total porosity in shale, nevertheless, are largely dependent on the calculated surface relaxivity (SR) values (Volokitin et al. 1999).

The SR value, which was commonly assumed as a constant in industry practice, however, varies tremendously in shales of different mineralogical composition (Saidian et al. 2015, Fleury 2007, Dunn et al. 2002). Surface relaxation, generated from the interaction between hydrogen nuclei and paramagnetic impurities on the surface of solid grains, is intimately associated with magnetic minerals of high magnetic susceptibility (Keating and Knight 2010, Saidian and Prasad 2015) and paramagnetic mineral concentrations and distributions (Keating and Knight 2012, Saidian et al. 2015); and can be largely influenced by the ratio of pore surface area to pore volume (SVR) (Hurlimann et al. 1994). Fe-bearing paramagnetic minerals such as pyrite, siderite, Illite, chlorite, smectite, contain unpaired electrons with randomly oriented spins exhibiting paramagnetic properties (Godefroy et al. 2001). Samples with higher Fe-bearing paramagnetic concentrations were reported to generate faster surface relaxation rate on a fluid-solid interface, thereby displaying higher SR values (Schön 2015) (Keating and Knight 2010) and thus further influencing the converted NMR results in shale petrophysical evaluations. Previous literature have concentrated more on investigating the influencing factors of SR values (Keating and Knight 2010, Keating and Knight 2006, Keating and Knight 2012, Falzone and Keating 2016, Saidian et al. 2015, Saidian and Prasad 2015), while a thorough understanding of how these influencing factors affect NMR pore structure interpretation via divergent SR values remains limited in shale studies.

This study examined the impact of SR on NMR-converted results in Permian Carynginia shales. The SR value is calculated from the logarithmic mean value of the NMR T_2 spectrum ($T_{2,lm}$) and the SVR value from LP-N_2-GA experiments. The converted NMR PSDs are compared with laboratory MICP results for discussions.

7.2. Materials and Methods

7.2.1. Shale Samples

A total of six shale samples were collected from Arrowsmith well in different depths of Permian Carynginia Formation in Northern Perth Basin, Western Australia. Geological settings have been described in the authors previous work (Yuan et al. 2018c). Core plug samples (1.5 in. diameter and 4-5cm length) were cleaned with toluene for NMR measurements. The chip samples around 12g were prepared for MICP test. Others were crushed into 60-mesh-size (<250 μm) fragments for LP-N_2-GA measurements. Mineralogical compositions present abundant quartz and clay contents in our test samples (**Table 7. 1**). Clays are mainly consisted of mixed layers of illite-smectite and illite/ muscovite, while moderate chlorite and minor kaolinite and smectite constitute the rest of the clay proportions. Fe-bearing paramagnetic minerals such as pyrite (FeS_2) and siderite ($FeCO_3$) are summarized to constitute the average of 4 wt % of the total minerals. Geochemical Rock-Eval analysis indicate an overall low TOC content range in Permian Carynginia shales (**Table 7. 2**).

Table 7. 1 XRD mineralogical composition (wt. %) of Permian Carynginia shale, Perth Basin, WA (Yuan et al. 2018c).

Name	Depth (m)	Quartz (wt %)	Pyrite (wt %)	Siderite (wt %)	Total clay (wt %)	Smectite (wt %)	Mixed illite/smectite (wt %)	Illite/ muscovite (wt %)	Chlorite (wt %)	Kaolinite (wt %)	Other minerals (wt %)
AC1	2780.2	35.6	3.3	1.1	50.8	0.9	25.8	13.1	5.8	5.2	9.2
AC2	2781.7	40.3	2.9	1.5	43.2	0.8	22.9	10.0	4.9	4.6	12.1
AC3	2789.9	47.6	2.1	1.4	32.3	0.6	12.5	11.5	3.5	4.2	16.6
AC4	2794.4	53.0	2.1	1.4	31.1	1.6	11.7	13.9	3.1	0.8	12.4
AC5	2806.4	41.3	3.1	1.5	40.7	0.9	14.9	18.9	5.2	0.8	13.4
AC8	2825.3	53.2	2.1	2.0	32.3	1.2	19.0	7.7	2.7	1.8	11.6

Table 7. 2 Geochemical Rock-Eval results for Carynginia shale samples.

Name	Formation	Depth (m)	TOC (wt. %)	T_{max} (°C)	HI	OI	S1 (mg/g)	S2 (mg/g)	S3 (mg/g)
AC1	Carynginia	2780.20	N/A	459	64	5	0.54	1.95	0.16
AC2	Carynginia	2781.70	1.79	459	36	16	0.18	0.64	0.28
AC3	Carynginia	2789.90	1.02	462	53	58	0.20	0.54	0.59
AC4	Carynginia	2794.40	0.64	458	39	27	0.13	0.25	0.17
AC5	Carynginia	2806.40	1.82	460	63	2	0.33	1.15	0.03

AC8	Carynginia	2825.30	0.77	463	69	70	0.34	0.53	0.54

7.2.2. Mercury injection capillary pressure (MICP)

The mercury injection capillary pressure (MICP) tests were carried out on the Micromeritics Autopore IV 9500 porosimeter to acquire the pore throat size distribution of shales. The volume of injected mercury was recorded at each step of the increased external pressures. As pressure gradually increased, small pores became accessible to mercury molecules so that external pressure could subsequently be converted to equivalent pore radius distribution based on the Washburn equation as shown in **Eq. 7.1**:

$$r_i = \frac{-2\sigma \cos\theta}{p_c} \quad \ldots\ldots\ldots\ldots \quad (7.1)$$

where r_i is the pore throat radius, µm; p_c is the injected pressure, MPa; σ is the interfacial surface tension of the working fluid (set to 0.485 J/m^2); and θ is the contact angle between the working fluid and the pore surface (applied 130^o for advancing/ receding contact angle). During the test, the applied external pressure ranged from 0.1 to a maximum of 60000 psia (413.7 MPa), which enabled the penetration of a pore throat size as small as 3.6 nm.

7.2.3. Low-pressure N_2 gas adsorption (LP-N_2-GA)

The LP-N_2-GA test was used to obtain adsorption isotherms, BET specific surface area (SSA), pore volume (PV) and pore size distribution (PSD) for tested samples. Prior to the test, the crushed samples were outgassed over 7 h under vacuum conditions at elevated temperatures to maintain the cleanliness of the adsorbent surfaces. Measurements were performed on Micromeritics® TriStar instrument at the bathing temperature of 77 K. By injecting N_2 into the tested samples, the isotherm curves of the adsorbed N_2 volume as a function of relative pressure (P/P_0) were recorded at a constant temperature (P_0 represents the saturation pressure, P represents the gas vapor pressure). The measured isotherm curves were fitted into classification types per the International Union of Pure and Applied Chemistry (IUPAC) to indicate pore shape geometry such as slit pores and ink-bottle pores (Sing 1985). The Brunauer-Emmett-Teller (BET) theory (Barrett et al. 1951) was applied to derive SSA. The density functional theory (DFT) model (Lastoskie et al. 1993, Seaton and Walton 1989) was performed on the adsorption isotherm branch to acquire PSD.

7.2.4. Low-field NMR (LF-NMR)

The LF-NMR was carried out with the 2 MHz Magritek Rock Core Analyzer on 1.5 in. core plugs, which were fully saturated with 30g/L KCl brine. Saturation was conducted on OpMan

Manual Saturator (version 8.0) from VINCI Technologies (France). The saturation was performed per the following procedures: (1) the low-permeable samples were loaded and vacuumed over 15h for the low-permeable shales; (2) the saturator was filled with 30g/L KCl brine and the samples were saturated by consecutively increasing the saturating pressures. Under each pressure step, the pumped pressure could possibly drop overnight; therefore, the pressure was consistently monitored and pumped up until the stabilized value was reached with no further pressure drop, which eventually reached to the maximum of 2000 psi. NMR experiments were subsequently conducted on the fully-saturated samples using the Carr, Purcell, Meilboom and Gill pulse sequence (Carr and Purcell 1954, Kenyon et al. 1995, Meiboom and Gill 1958), with parameters of 100 μs inter-echo spacing (TE), 10000 ms inter-experiment delay, 10000 number of echoes and a minimum signal to noise ratio (SNR) of 200.

LF-NMR primarily functions by activating the hydrogen proton in the pore fluid under an external magnetic field. The T_2 relaxation time is identified once the magnetic field withdraws and T_2 distribution can be obtained and converted into PSD (Freedman and Heaton 2004, Kenyon et al. 1995). Theoretically, three independent relaxation mechanisms of fluids are included in reservoir rocks: bulk relaxation, diffusion relaxation and surface relaxation; while bulk and diffusion relaxations are negligible for the homogeneous magnetic field with short TE. T_2 relaxation could be simplified as **Eq. 7.2** (Coates et al. 1999, Yao et al. 2010).

$$\frac{1}{T_{2i}} = \rho_2 (\frac{S}{V})_i = \rho_2 \, (\frac{C_s}{r_i}) \quad \ldots\ldots\ldots\ldots \quad (7.2)$$

where T_{2i} is the T_2 relaxation time at experimental point i, ρ_2 is the surface relaxivity, $(\frac{S}{V})_i$ is the pore surface area to pore volume ratio (SVR) determined by LP-N_2-GA; r_i is the pore radius at experimental point i; C_s is a constant value dependent on geometric pore shape. The types of slit, cylindrical and spherical pores correspond to the values of 1, 2, and 3, respectively. Note that the pore shape constant $C_s = 1$ was applied due to the determination of slit pore shape based on N_2 isotherm hysteresis discussion in Results and Discussion Section.

7.3. Results and discussion

7.3.1. MICP pore throat size distribution (PTD)

Figure 7. 1 presents MICP results including pore throat size distributions (PTDs) (**Figure 7. 1**a) and capillary pressure (P_c) curves (**Figure 7. 1**b) of the tested shale samples. As a

nonwetting fluid, mercury was initially forced into pore structure under threshold pressure (P_T). The injected mercury saturation accumulates by the gradual increases in injection pressure. PTDs in Permian Carynginia shales demonstrate a major pore throat size in the range of 4-10 nm; larger macropores or fractures are indicated by signals over 10 μm (**Figure 7. 1**a).

When the MICP-derived petrophysical parameters are compared between the tested samples, variations can be observed. As shown in **Figure 7. 1**a, the PTD in AC1 and AC2 exhibits the narrow-distributed modals with higher peak values; AC3, AC4, AC5 display lower peaks, while the lowest peak is shown in AC8 with the widest PTD range. **Table 7. 3** and **Figure 7. 1**b display the capillary pressure results. The threshold pressure (P_T) is observed to be higher in AC1 (6196 psi) and AC2 (5783 psi), while the lowest P_T value is found in AC8 (680 psi). Lower R_{max} and R_{50} are displayed in AC1 (i.e., 13.5 and 11.4nm, respectively) and AC2 (i.e., 16.6 and 15.3nm, respectively), while AC8 presents the highest values (718.4 and 75.2nm, respectively). A remarkably higher permeability is exhibited in AC8 (238 nD), whereas lower values are demonstrated in AC1 (0.05 nD) and AC2 (3.1 nD).

Notably, higher clay minerals contents are presented in AC1 (50.8 wt %) and AC2 (43.2 wt %) compared to that in AC8 (32.3 wt %). Meanwhile, detrital quartz contents are less involved in AC1 (35.6 wt %) and AC2 (40.3 wt %) than that in AC8 (53.2 wt %). Previous studies revealed that the mineral-associated pore network in shales consists of the intraparticle pores within clay aggregates or detrital grains, and the intergranular pores between detrital quartz grains or crystals/clay platelets (Loucks et al. 2012, Loucks et al. 2010, Liu et al. 2019, Passey et al. 2010). The organic matter pores also play a significant role in pore system development of organic-rich shales (Liu et al. 2018d, Milliken et al. 2013, Kuila et al. 2014b). As indicated in **Table 7. 2**, most of our studied samples exhibit low TOC content, we thus essentially concentrated on the pores that are intimated with mineral assemblages. For shales of higher clay and lower quartz contents (e.g. AC1 and AC2), the uniform but poorly connected pore structures are developed, with major pore sizes locating in a smaller pore size range. By contrast, for shales of lower clay and higher quartz contents (e.g., AC8), the unevenly distributed but well-connected pores are generated with overall larger pore throat sizes, which allows mercury to penetrate into the pore structure more easily.

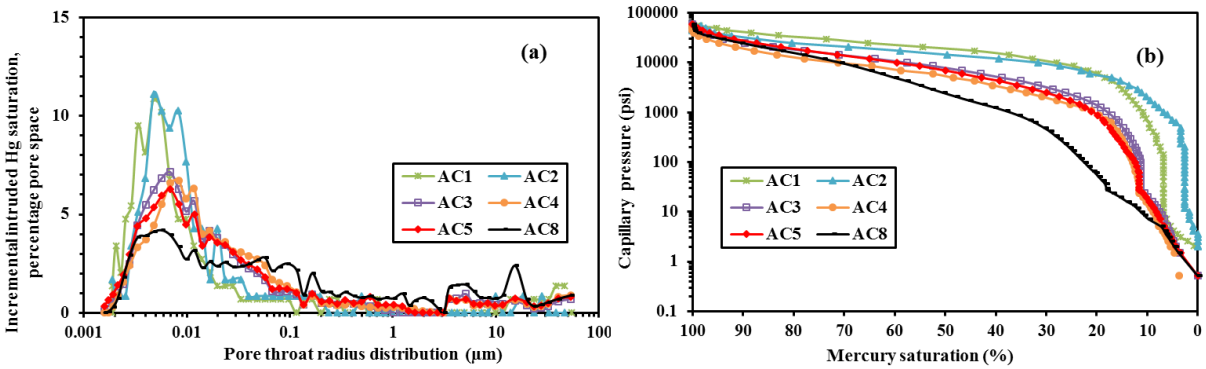

Figure 7. 1 (a) Pore throat size distributions and (b) capillary pressure curves in Permian Carynginia shales measured by MICP.

Table 7. 3 Petrophysical parameter of shale samples based on MICP and gas permeability test [a].

Name	Depth (m)	MICP Φ	K_g (nD)	P_T (psi)	R_{max} (nm)	R_{50} (nm)
AC1	2780.2	3.78	0.05	6196	13.5	11.4
AC2	2781.7	3.05	3.1	5783	16.6	15.3
AC3	2789.9	3.17	144	2377	89.8	23
AC4	2794.4	3.54	53.9	1795	71.8	28.4
AC5	2806.4	3.56	46.6	1701	56.7	26
AC8	2825.3	3.03	238	680	718.4	75.2

[a] Some data are previously published (Al Hinai et al. 2014) .

[b] R_{max} is the threshold pore throat radius for mercury invasion; R_{50} is the pore throat radius (nm) at 50% mercury saturation. MICP Φ is MICP total connected porosity; P_T is threshold pressure; K_g is gas permeability.

7.3.2. Low-pressure N_2 gas adsorption (LP-N_2-GA)

Figure 7. 2 presents the N_2 adsorption/ desorption isotherm curves of the studied samples. The hysteresis loops between adsorption and desorption curves are fitted into the H4 Type per by IUPAC classification, indicating the pore shape geometry as slit type (Sing 1985, Zheng et al. 2018). BET Specific surface area (SSA) ranges from 2.84 to 5.57 m²/g. The surface to volume ratio (SVR) was calculated to range from 86 to 844 μm^{-1} based on N_2 adsorption results (**Table 7.4**).

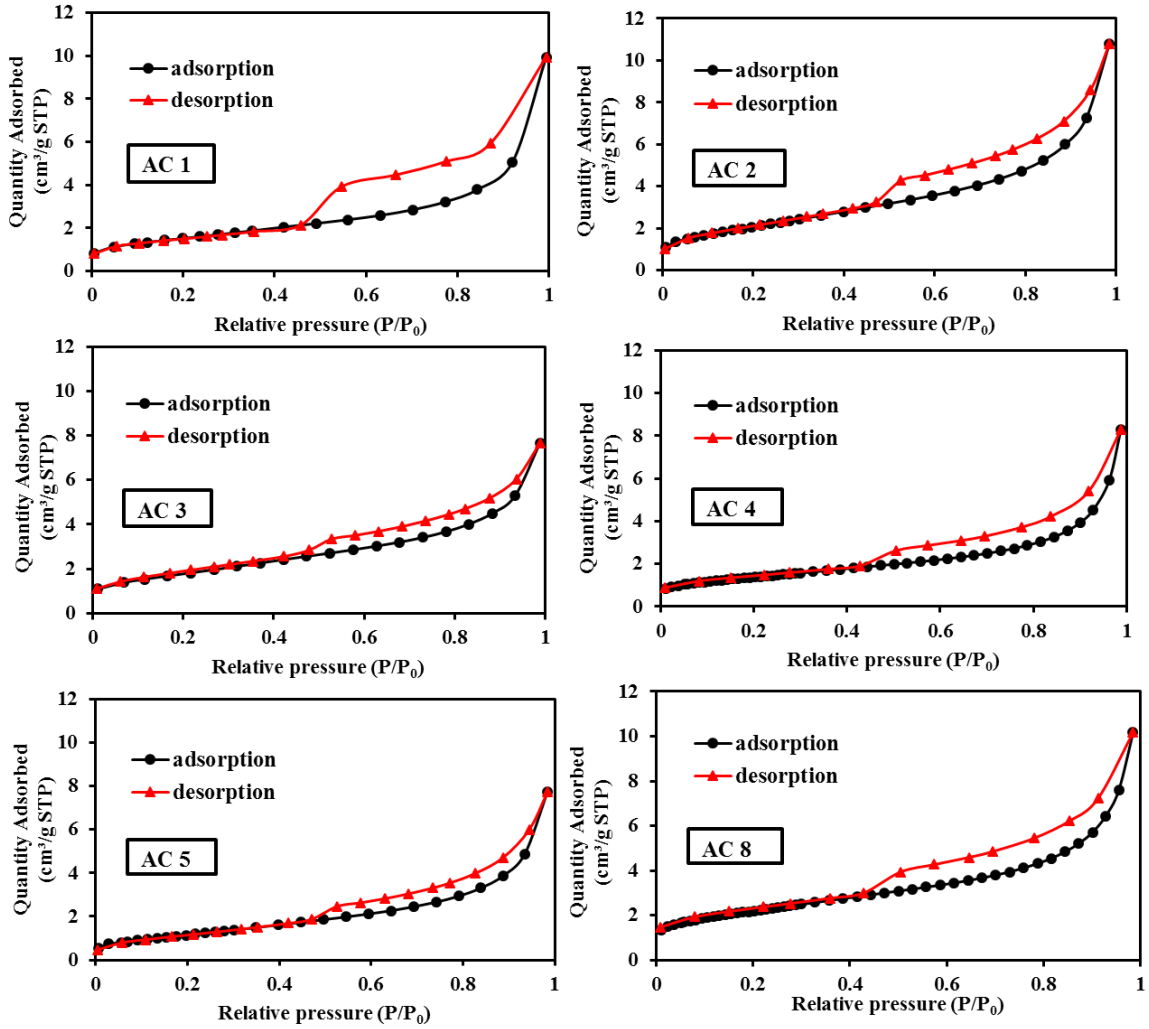

Figure 7. 2 Isotherm curves of Carynginia shales derived from LP-N_2-GA measurement.

7.3.3. LF-NMR: Surface relaxivity (SR) calculation

To obtain reliable SR values (**Eq. 7.3**), the accurate calculation of logarithmic mean T_2 ($T_{2,lm}$) (**Eq. 7.4**) and SVR values are conducted based on the previous studies (Saidian and Prasad 2015, Kleinberg 1996, Fleury 2007, Lucatorto et al. 1999):

$$\frac{1}{T_{2,lm}} = \rho_2\left(\frac{SSA}{PV}\right) \quad \ldots\ldots\ldots\ldots \quad (7.3)$$

$$T_{2,lm} = \exp\left(\frac{\sum_1^i \ln(T_{2i}) * \emptyset_i}{\sum_1^i \emptyset_i}\right) \quad \ldots\ldots\ldots\ldots \quad (7.4)$$

where $T_{2,lm}$ is the logarithmic mean value of T_2 distribution; i represents experimental points; $\emptyset_i$ is the NMR-measured incremental porosity at point i ; and $\frac{SSA}{PV}$ is SVR value.

The calculated SR values and relevant petrophysical parameters from NMR measurements are summarized in **Table 7. 5**. Carynginia SR values range from 0.08 to 0.32 μm/s which vary with mineralogical compositions. Comparably, shales from U.S. middle-Bakken and Three Forks formations present SR values ranging from 0.39 to 2.54 μm/s (Saidian and Prasad 2015), while Lower Silurian Longmaxi shales in China range between 4.26 and 28.22 μm/s (Liu et al. 2018d). The tremendous SR variations among different shales could possibly be influenced by factors that include: (1) the type of magnetic minerals such as paramagnetic minerals (i.e., Fe-bearing chlorite, illite, smectite, pyrite and siderite) and ferromagnetic minerals of high magnetic susceptibility; (2) the content of paramagnetic minerals (or ferromagnetic minerals); (3) the spatial distribution of paramagnetic minerals (or ferromagnetic minerals) (Keating and Knight 2012, Saidian et al. 2015); (4) pore size distributions and specific surface area (Benavides et al. 2017, Saidian et al. 2015); Additionally, organic matter (OM) would incidentally affect SR values by means of: (a) the extra relaxation induced by hetero-nuclear coupling within hydrogen-bearing kerogen structures; (b) the contents and distributions of paramagnetic pyrite that is intimately associated with OM; and (c) OM pore size distribution and specific surface area (Saidian et al. 2015). Furthermore, the NMR experimental settings, e.g., spectrometer frequency, the inter-echo spacing, the waiting time, the elevated temperature, could also significantly result in SR variations (Xu et al. 2015, Chakravarty et al. 2018, Godefroy et al. 2002). In our low-TOC samples, the primary SR influencing factor is considered to be contributed by mineralogical variations, in particular, the concentration of paramagnetic minerals. As shown in Figure 3, SR values exhibit the linear positive correlations with the paramagnetic clay mineral contents ($R^2 = 0.72$) and the pyrite/ siderite contents ($R^2 = 0.81$), consistent with the results demonstrated in previous studies (Saidian and Prasad 2015, Saidian et al. 2015).

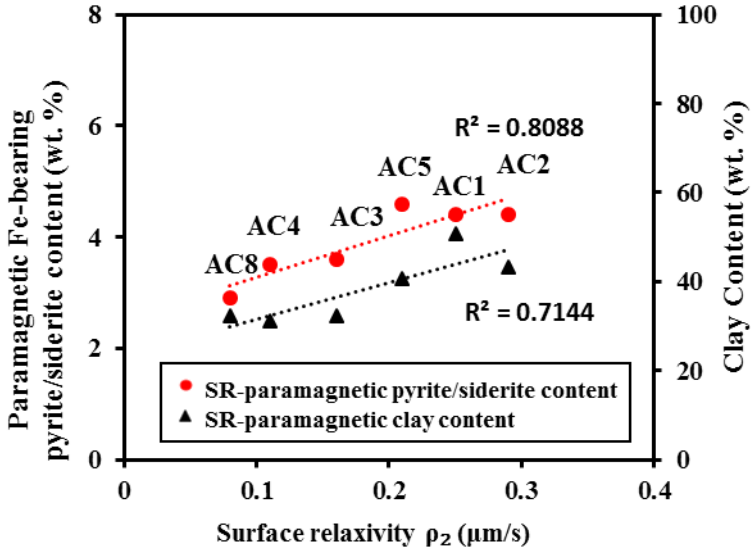

Figure 7. 3 Cross-plot of the calculated surface relaxivity (SR) versus paramagnetic Fe-bearing clay contents and pyrite+siderite contents in Permian Carynginia shales.

Table 7.4 displays high magnetic susceptivity in siderite and pyrite, ranging from 1300 to 11000×10^{-6} and 35 to 5000×10^{-6} SI, respectively [28], and largely enhancing the relaxation of the spins on mineral surface. AC1 and AC2, which involve higher contents of Fe-bearing paramagnetic minerals and higher SSA (5.53 and 5.57 m^2/g, respectively) (**Table 7. 2**), exhibit higher SR values (0.25 and 0.29 μm/s, respectively) (**Table 7. 5**). By contrast, AC8 with relatively low paramagnetic minerals and low SSA (3.79 m^2/g) presents a low SR value of 0.08 μm/s.

Table 7.4 Magnetic and pore structure properties of the test samples and associated mineral components.

Materials	Magnetism	Magnetic susceptivity (×10 $^{-6}$ SI)	Surface relaxivity ρ, (μm/s)	Φ, %	SSA (m^2/g)	SVR (μm^{-1})
AC1 shale sample	–	63 ~ 18,600 [c]	0.25	10.06 [a]	5.53	85.57
AC2 shale sample	–		0.29	10.04 [a]	5.57	663.1
AC3 shale sample	–		0.32	11.05 [a]	5.18	332.0
AC4 shale sample	–		0.11	10.66 [a]	2.84	765.7
AC5 shale sample	–		0.21	12.87 [a]	4.28	844.1
AC8 shale sample	–		0.08	8.02 [a]	3.79	753.1
High-concentration	Paramagnetic	35 ~ 5,000 [b]	1.80 [b]	0.48 [b]	0.21 [b]	0.59 [b]

pyrite mixture						
Low-concentration Pyrite mixture	Paramagnetic		1.20 [b]	0.48 [b]	0.16 [b]	0.50 [b]
High-concentration siderite mixture	Paramagnetic	1300 ~ 11,000 [b]	≥ 26 [b]	0.49 [b]	0.38 [b]	1.05 [b]
Low-concentration siderite mixture	Paramagnetic		≥ 19 [b]	0.49 [b]	0.33 [b]	0.90 [b]
Illite	Paramagnetic	410 [d]	0.9 [e]	–	41 [f]	–
Smectite	Paramagnetic	330 ~ 350 [c]	0.9 [e]		61 [f]	
Chlorite	Paramagnetic	70 ~1550 [g]	0.4 [e]		40 [f]	

a (Yuan et al. 2018c); b (Keating and Knight 2010); c (Hunt et al. 1995); d (Dearing 1994); e (Prammer et al. 1996); f (Macht et al. 2011) g (Tarling and Hrouda 1993).

Table 7. 5 Petrophysical properties of the test samples based on NMR analysis.

Sample	Depth, m	MICP porosity, %	NMR total porosity, %	Surface relaxivity ρ, μm/s
AC1	2780.2	3.78	10.06	0.25
AC2	2781.7	3.05	10.04	0.29
AC3	2789.9	3.17	11.50	0.32
AC4	2794.4	3.54	10.66	0.11
AC5	2806.4	3.56	12.87	0.21
AC8	2825.3	3.03	8.02	0.08

7.3.4. LF-NMR: PSD conversion and comparison

Figure 7. 4a presents the measured NMR T_2 distributions. Incremental T_2 spectra exhibit multi-modal distribution with the main peak at 0.3-1 ms. Small peaks at relaxation time higher than 10 ms mainly correspond to the proportions of larger pores or fractures. NMR T_2 spectra in AC1 and AC2 show narrow ranges in short relaxation times, while AC8 presents a broad range with a continuous distribution in larger relaxation times, consistent with MICP-PTD performance. By converting the NMR T_2 spectrum into PSD via SR (**Eq. 7.2**), as shown in **Figure 7. 4**b, the major pore volumes are displayed in micro/mesopore range (<50 nm). Interestingly, a peak separation is newly generated among the curves after conversion. By comparing the T_2 peaks with the converted-PSD peaks among tested samples, we found that the converted PSD in AC1, AC2, AC5 evidently shifts towards larger pore size range and clearly separate themselves from AC3, AC4, AC8 (**Figure 7. 4**b). As discussed in section 3.3., higher Fe-bearing paramagnetic mineral contents coupled with larger SSA in AC1, AC2, and

AC5 expedite the surface relaxation rate that possibly results in the obvious PSD curves separation in **Figure 7. 4**.

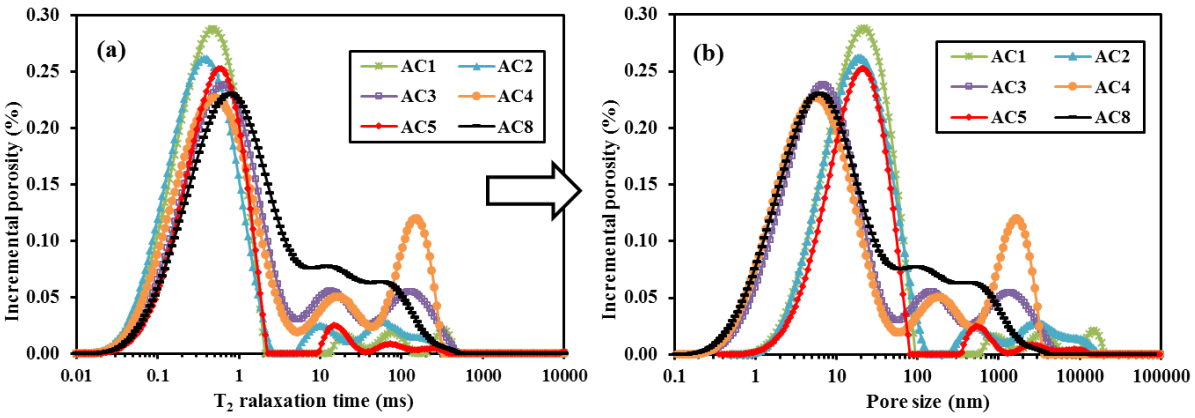

Figure 7. 4 NMR T_2 spectrum and the converted pore size distribution (PSD) of Permian Carynginia shales.

Figure 7. 5 overlapped the NMR-converted PSD and MICP-PTD. Obvious discrepancies are displayed in curve amplitudes and ranges between the two techniques. The MICP peaks approximately center at 5 nm in all the samples; NMR peaks, however, separate between samples under the impact of paramagnetic minerals. As shown in **Table 7. 5**, the MICP porosity ranges from 3.03 to 3.78% with subtle variations between samples; by contrast, NMR porosity ranges from 8.02 to 12.87%, demonstrating overall larger values compared to MICP results.

The discrepancies and inconsistencies in pore interpretations between NMR and MICP are presumed to be synthetically induced by numerous influencing factors. Fundamentally, the variation of mineral compositions, mineral assemblages, and organic matter geochemical properties generates different pore types and pore shape combinations (Clarkson et al. 2013), leading to the deviation between pore body size and pore throat size that primarily contributes to NMR and MICP discrepant interpretations. NMR, which utilizes H_2O as the working fluid with the kinetic molecular diameter of 0.278 nm (Bondi 1964), is essentially controlled by pore-body size distribution, which is intimately associated with SSA (Schön 2015). By contrast, MICP, which employs Hg of kinetic molecular diameter of 0.31 nm (Bondi 1964), associates with the connected pore-throat size and are influenced by capillary pressure, resulting in the limited pore accessibility in pore sizes larger than 3.6 nm. The physical connectivity of pore networks, the molecular dimeter and bond angle of working fluids, and the compatibility

between shale pore network and the applied working fluids synthetically influence the interpretation results (Sondergeld et al. 2010b, Vincent et al. 2011). Moreover, the clay swelling effect, which is introduced in saturation protocol in NMR measurement, is likely to induce pore volume overestimation in clay-rich shales. Unlike MICP accessing interconnected porosities, NMR approaches total porosity including effective porosity and the ineffective porosity occupied by clay bound water (Topór et al. 2016, Yuan et al. 2018c, Saidian et al. 2015, Prammer et al. 1996, Fleury et al. 2013, Straley et al. 1997, Testamanti and Rezaee 2017, Yuan and Rezaee 2019b), indicating the effect of clay bound water in clay rich shales. Additional influencing factors such as the temperature involved in shale sample pre-treatments (Holmes et al. 2017, Yuan et al. 2018c), the different scale of sample sizes in NMR and MICP tests, the NMR settings (discussed in section 3.3), and the high MICP injection pressure (60000 psi), all contribute to the divergences in NMR and MICP interpretations in shale studies.

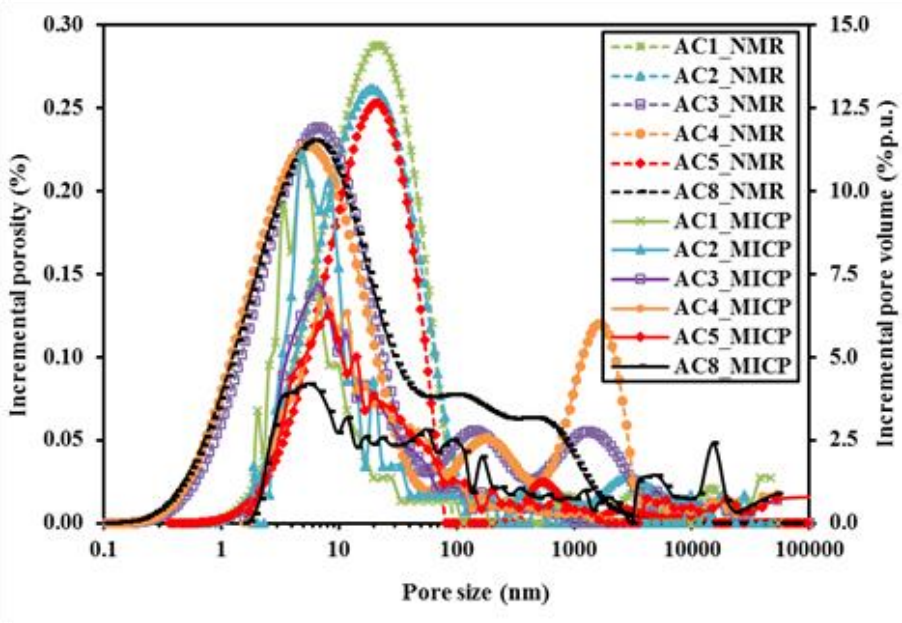

Figure 7. 5 Overlapped NMR-derived PSD and MICP-PTD in Permian Carynginia shales.

7.4. Conclusions

- Our findings indicate that surface relaxivity (SR), which is largely influenced by Fe-bearing paramagnetic minerals, would affect NMR conversions.
- SR in our tested samples ranges from 0.08 to 0.32 μm/s and varies significantly with mineralogical composition.

- Paramagnetic Fe-bearing mineral contents are intimately associated with surface relaxation. Linear correlations are presented between SR values and pyrite/siderite concentrations.
- SR performs as the main cause for the deviation of NMR-converted PSD and P_c curves compared to that in the MICP results.
- The interpretation discrepancies in pore size distribution and porosity between MICP and NMR are synthetically influenced by the internal factors of the samples (e.g., paramagnetic mineral components, geometric pore shape combinations and pore connectivity) and the external factors involved in experiments (i.e., sample pretreatment protocols, experimental working fluids, NMR parameter settings, and high MICP injection pressure settings).

CHAPTER 8 Conclusions and Outlook for Future Work

8.1 Conclusions

This project is carried out to evaluate pore structure properties (porosity, PSD, SSA, pore volume, fractal dimension) in different shales by using various measurements (NMR, LP-N_2/CO_2-GA, MICP, helium porosimetry). Result interpretations demonstrate discrepancies in different methods that are largely influenced by shale compositions. The novel and main findings are summarized as below for a better understanding of shale pore structure and its impact on shale gas storage capacity:

1. Porosity inconsistencies between different methods:

- The major porosity and PSD discrepancies are demonstrated between NMR and the other penetration approaches (e.g., MICP, HE, LP-GA), particularly in clay-rich shales.
- Clay-rich shales generate NMR porosity significantly higher than MICP and helium porosity, while clay-poor shales exhibit a general consistency between NMR, MICP and HE porosity.
- The higher porosity exhibited by NMR over MICP/ helium porosimetry is fundamentally attributed to CBW.
- The advanced low-field NMR technique is beneficial for non-destructive detection of the total porosity, which includes effective porosity and ineffective porosity occupied by CBW. Other penetration approaches such as MICP and helium detect intercommunicated pores, equivalent to effective porosity.
- MICP detects connected pores larger than 3.6 nm, while helium porosimetry enables the access to smaller pores as the NMR probe does. NMR and helium porosimetry is expected to be combined for the implications of CBW estimation.

2. The impact of CBW on effective porosity and quantitative CBW assessment

- Combining NMR with LP-N_2-GA is an effective method to monitor the pore fluid differentiation in shales under the thermal dehydration schemes.
- The cutoff temperature of 80°C (75°C) is able to maximally extract the removable water from the pores, meanwhile, keeps the nanopore structures, the CBW, and clay minerals well-protected.

- Dewatering temperatures below 75°C lead to misinterpretation of nanopore structure due to insufficient water removal on pore surface. Temperatures above 80°C induce clay conversion from smectite to illite.
- NMR T_2 cutoff for CBW can be obtained by using 80℃ as cutoff temperature.
- CBW determined by NMR T2 cut-off method is quantified to range between 1.64% and 3.02% for Permian Carynginia shales with the average clay contents more than 30%.
- Under the impact of CBW, effective porosity of the tested Permian Carynginia shales is quantified to range from 5.29% and 11.23%.

3. The impact of CBW on geometric micro/mesopore fractal properties

- CBW is intimately related to geometric pore structure heterogeneity (fractal dimension), which largely influence gas adsorption behaviors.
- The fractal dimensions derived from NMR and LP-N_2-GA experiments are closely correlated.
- The pore surface fractal dimension associated with CBW ineffective porosity (D_{cbw}) is intimate with micropore surface roughness.
- The pore volume fractal dimension related to effective porosity (D_{eff}) is associated with meso-/macropore volume complexity.
- Pore surface with higher heterogeneity, represented by higher surface dimension, would involve more CBW bound on pore surface. The complex pore structure, represented by a higher pore volume dimension, would make effective pores more heterogeneous for higher potential of gas storage capacity.
- D_{cbw} increases with the increasing CBW and decreases with the increasing effective porosity. Higher D_{cbw} indicates more CBW adsorption on clay surfaces and less effective porosity in shales.
- D_{eff} increases with the increasing gas storage capacity. Larger D_{eff} indicates a more complicated pore volume with higher potential of shale gas storage.

4. The impact of clay and TOC content on micro/mesopore volume and SSA

- Micro/mesopore volume and SSA, which dramatically vary from different shale formations, are jointly controlled by mineralogical and organic geochemical properties.
- Micropores smaller than 2 nm are more intimately correlated with organic matter pores.

- Mesopores in 2-17 nm are predominately controlled by clays (dominantly illite). Meso/macropores larger than 17 nm are contributed by both organic matter and clay mineral pores.
- In different depth of shale formation in high heterogeneity, samples containing higher clay and lower quartz contents tend to develop more uniform PSD, and are likely to be predominated by smaller pores compared to the samples with higher quartz and lower clay contents.
- Goldwyer formation in WA develops more pore volume in the finer-mesopore size range (2-17nm) due to the remarkable abundance of clay minerals (avg. 71.9 %).

5. The impact of paramagnetic minerals on NMR-PSD interpretation

- PSD conversion from NMR T_2 spectrum is largely influenced by surface relaxivity (SR).
- SR values are intimate with paramagnetic Fe-bearing mineral composition in shale, and could largely vary in different depth of the same shale formation due to the heterogeneous and broad range of Fe-bearing mineralogical composition.
- SR values are linearly correlated with clay mineral contents and pyrite/siderite concentrations.
- SR ranges from 0.08 to 0.32 μm/s in Permian Carynginia shales in Perth Basin, WA.

8.2 Outlook for future study

Though a wide range of shale samples with typical compositions was involved for pore structure property investigations, there are undoubtfully limitations that this study did not reach and therefore should be fully addressed for future studies:

1. The porosity of OM-poor Monterey and Carynginia shale samples with a broader range of clay contents was investigated based on NMR, MICP, Helium porosimetry techniques. It is, however, also significant to involve samples with a large variety of TOC content and thermal maturity for further discussion.
2. To study the impact of composition on micro-/mesopore volume and SSA, the isolated kerogens of OM-rich Bakken shales are studied. More information would be provided if the separated mineral sections could also be able to be tested for micro-/mesopore structure assessment.

3. The OM and clay mineral pore networks are suggested to be separately studied by using various approaches such as NMR, MICP, LP-GA, and helium porosimetry to reveal more detailed and novel understandings.
4. The impact of surface relaxivity on NMR converted PSD was conducted based on OM-poor Carynginia shales. However, OM richness and spatial distribution also influence SR value and further affect PSD conversion, which requires more samples for clarification.
5. The study of micro-/mesopore fractal analysis is recommended to be further conducted based on the atomistic nanopore models from the perspective of adsorption energy.

Reference

Acholla, F.V. & Orr, W.L. 1993. Pyrite removal from kerogen without altering organic matter: the chromous chloride method. *Energy & Fuels* **7**, 406-410.

Al Hinai, A., Rezaee, R., Esteban, L. & Labani, M. 2014. Comparisons of pore size distribution: A case from the Western Australian gas shale formations. *Journal of Unconventional Oil and Gas Resources* **8**, 1-13.

Avnir, D., Farin, D. & Pfeifer, P. 1984. Molecular fractal surfaces. *Nature* **308**, 261.

Avnir, D. & Jaroniec, M. 1989. An isotherm equation for adsorption on fractal surfaces of heterogeneous porous materials. *Langmuir* **5**, 1431-1433.

Bahadur, J., Melnichenko, Y., Mastalerz, M., Furmann, A. & Clarkson, C.R. 2014. Hierarchical pore morphology of cretaceous shale: a small-angle neutron scattering and ultrasmall-angle neutron scattering study. *Energy & Fuels* **28**, 6336-6344.

Bahadur, J., Radlinski, A.P., Melnichenko, Y.B., Mastalerz, M. & Schimmelmann, A. 2015. Small-angle and ultrasmall-angle neutron scattering (SANS/USANS) study of New Albany shale: a treatise on microporosity. *Energy & Fuels* **29**, 567-576.

Bahar M., C., P., and Stevens, M. K.,. 2011. North perth basin shale gas resource evaluation. *Department of Mines and Petroleum, Petroleum Division, unpubl*.

Barrett, E.P., Joyner, L.G. & Halenda, P.P. 1951. The determination of pore volume and area distributions in porous substances. I. Computations from nitrogen isotherms. *Journal of the American Chemical society* **73**, 373-380.

Benavides, F., Leiderman, R., Souza, A., Carneiro, G. & Bagueira, R. 2017. Estimating the surface relaxivity as a function of pore size from NMR T2 distributions and micro-tomographic images. *Computers & Geosciences* **106**, 200-208.

Bird, N., Perrier, E. & Rieu, M. 2000. The water retention function for a model of soil structure with pore and solid fractal distributions. *European Journal of Soil Science* **51**, 55-63.

Bondi, A. 1964. van der Waals volumes and radii. *The Journal of physical chemistry* **68**, 441-451.

Bowker, K.A. 2007. Barnett Shale gas production, Fort Worth Basin: issues and discussion. *Aapg Bulletin* **91**, 523-533.

Bu, H., Ju, Y., Tan, J., Wang, G. & Li, X. 2015. Fractal characteristics of pores in non-marine shales from the Huainan coalfield, eastern China. *Journal of Natural Gas Science and Engineering* **24**, 166-177.

Busch, A., Schweinar, K., Kampman, N., Coorn, A., Pipich, V., Feoktystov, A., Leu, L., Amann-Hildenbrand, A. & Bertier, P. Year. Shale Porosity-What Can We Learn from Different Methods? Conference Shale Porosity-What Can We Learn from Different Methods?

Bustin, R.M., Bustin, A.M., Cui, A., Ross, D. & Pathi, V.M. Year. Impact of shale properties on pore structure and storage characteristics. Conference Impact of shale properties on pore structure and storage characteristics.

Caineng, Z., Zhi, Y., Songqi, P., Yanyan, C., Senhu, L., Jinliang, H., Songtao, W., Dazhong, D., Shufang, W. & Feng, L. 2016. Shale gas formation and occurrence in China: an overview of the current status and future potential. *Acta Geologica Sinica - English Edition* **90**, 1249-1283.

Carr, H.Y. & Purcell, E.M. 1954. Effects of Diffusion on Free Precession in Nuclear Magnetic Resonance Experiments. *Physical Review* **94**, 630-638.

Chakravarty, A., Tinni, A., Rai, C.S. & Sondergeld, C.H. Year. NMR Considerations in Shales at Elevated Temperature. Conference NMR Considerations in Shales at Elevated Temperature, 2296-2306.

Chalmers, G.R. & Bustin, R.M. 2007. The organic matter distribution and methane capacity of the Lower Cretaceous strata of Northeastern British Columbia, Canada. *International Journal of Coal Geology* **70**, 223-239.

Chalmers, G.R., Bustin, R.M. & Power, I.M. 2012. Characterization of gas shale pore systems by porosimetry, pycnometry, surface area, and field emission scanning electron microscopy/transmission electron microscopy image analyses: Examples from the Barnett, Woodford, Haynesville, Marcellus, and Doig units. *Aapg Bulletin* **96**, 1099-1119.

Chang, D., Vinegar, H.J., Morriss, C. & Straley, C. Year. Effective porosity, producible fluid and permeability in carbonates from NMR logging. Conference Effective porosity, producible fluid and permeability in carbonates from NMR logging.

Clarkson, C.R., Freeman, M., He, L., Agamalian, M., Melnichenko, Y., Mastalerz, M., Bustin, R., Radliński, A. & Blach, T.P. 2012b. Characterization of tight gas reservoir pore structure using USANS/SANS and gas adsorption analysis. *Fuel* **95**, 371-385.

Clarkson, C.R., Solano, N., Bustin, R.M., Bustin, A.M.M., Chalmers, G.R.L., He, L., Melnichenko, Y.B., Radliński, A.P. & Blach, T.P. 2013. Pore structure characterization of North American shale gas reservoirs using USANS/SANS, gas adsorption, and mercury intrusion. *Fuel* **103**, 606-616.

Clavier, C., Coates, G. & Dumanoir, J. 1984. Theoretical and experimental bases for the dual-water model for interpretation of shaly sands. *Society of Petroleum Engineers Journal* **24**, 153-168.

Coates, G.R., Galford, J., Mardon, D. & Marschall, D. 1998. A new characterization of bulk-volume irreducible using magnetic resonance. *The Log Analyst* **39**.

Coates, G.R., Xiao, L. & Prammer, M.G. 1999. *NMR logging: principles and applications.* Gulf Professional Publishing.

Curtis, J.B. 2002. Fractured shale-gas systems. *Aapg Bulletin* **86**, 1921-1938.

Curtis, M.E., Cardott, B.J., Sondergeld, C.H. & Rai, C.S. 2012. Development of organic porosity in the Woodford Shale with increasing thermal maturity. *International Journal of Coal Geology* **103**, 26-31.

Dearing, J. 1994. Environmental magnetic susceptibility. *Using the Bartington MS2 system. Kenilworth, Chi Publ*.

Departments of Mines and Petroleum, W. 2015. Petroleum Prospectivity of Western Australia's Sedimentary Basins-Perth Basin.

Dubinin, M. & Astakhov, V. 1971. Description of adsorption equilibria of vapors on zeolites over wide ranges of temperature and pressure. ACS Publications.

Dunn, K.-J., Bergman, D.J. & LaTorraca, G.A. 2002. *Nuclear magnetic resonance: Petrophysical and logging applications.* Elsevier, ISBN 0080537790.

Easley, T.G., Sigal, R. & Rai, C. Year. Thermogravimetric analysis of Barnett shale samples. Conference Thermogravimetric analysis of Barnett shale samples.

Falzone, S. & Keating, K. 2016. A laboratory study to determine the effect of pore size, surface relaxivity, and saturation on NMR T2 relaxation measurements. *Near Surface Geophysics* **14**, 57-69.

Figini-Albisetti, A., Velasco, L.F., Parra, J.B. & Ania, C.O. 2010. Effect of outgassing temperature on the performance of porous materials. *Applied Surface Science* **256**, 5182-5186.

Fleury, M. Year. NMR surface relaxivity determination using NMR apparent diffusion curves and BET measurements. Conference NMR surface relaxivity determination using NMR apparent diffusion curves and BET measurements, 10-12.

Fleury, M., Kohler, E., Norrant, F., Gautier, S., M'Hamdi, J. & Barré, L. 2013. Characterization and quantification of water in smectites with low-field NMR. *The Journal of Physical Chemistry C* **117**, 4551-4560.

Fleury, M. & Romero-Sarmiento, M. 2016. Characterization of shales using T1–T2 NMR maps. *Journal of Petroleum Science and Engineering* **137**, 55-62.

Folk, R.L. 1980. *Petrology of sedimentary rocks.* Hemphill Publishing Company, ISBN 0914696149.

Freed, R.L. & Peacor, D.R. 1989. Variability in temperature of the smectite/illite reaction in Gulf Coast sediments. *Clay Minerals* **24**, 171-180.

Freedman, R. 2006. Advances in NMR logging. *Journal of Petroleum Technology* **58**, 60-66.

Freedman, R. & Heaton, N. 2004. Fluid characterization using nuclear magnetic resonance logging. *Petrophysics* **45**.

Furmann, A., Mastalerz, M., Bish, D., Schimmelmann, A. & Pedersen, P.K. 2016. Porosity and pore size distribution in mudrocks from the Belle Fourche and Second White Specks Formations in Alberta, Canada. *Aapg Bulletin* **100**, 1265-1288.

Gasparik, M., Bertier, P., Gensterblum, Y., Ghanizadeh, A., Krooss, B.M. & Littke, R. 2014. Geological controls on the methane storage capacity in organic-rich shales. *International Journal of Coal Geology* **123**, 34-51.

Gasparik, M., Ghanizadeh, A., Bertier, P., Gensterblum, Y., Bouw, S. & Krooss, B.M. 2012. High-pressure methane sorption isotherms of black shales from the Netherlands. *Energy & Fuels* **26**, 4995-5004.

Geatches, D., McCarty, D. & Wilcox, J. 2014. Ab initio investigations of dioctahedral interlayer-deficient mica: Modeling particles of illite found within gas shale. ISBN 1945-3027.

Geatches, D.L. & Wilcox, J. 2014. Ab initio investigations of dioctahedral interlayer-deficient mica: modelling 1 M polymorphs of illite found within gas shale. *European Journal of Mineralogy*.

Godefroy, S., Fleury, M., Deflandre, F. & Korb, J.-P. 2002. Temperature effect on NMR surface relaxation in rocks for well logging applications. *The Journal of Physical Chemistry B* **106**, 11183-11190.

Godefroy, S., Korb, J.-P., Fleury, M. & Bryant, R. 2001. Surface nuclear magnetic relaxation and dynamics of water and oil in macroporous media. *Physical Review E* **64**, 021605.

Goklen, K.E., Stoecker, T.J. & Baddour, R.F. 1984. A method for the isolation of kerogen from green river oil shale. *Industrial & engineering chemistry product research and development* **23**, 308-311.

Gregg, S.J., Sing, K.S.W. & Salzberg, H. 1967. Adsorption surface area and porosity. *Journal of The Electrochemical Society* **114**, 279C-279C.

Handwerger, D.A., Keller, J. & Vaughn, K. Year. Improved petrophysical core measurements on tight shale reservoirs using retort and crushed samples. Conference Improved petrophysical core measurements on tight shale reservoirs using retort and crushed samples.

Heller, R. & Zoback, M. 2014. Adsorption of methane and carbon dioxide on gas shale and pure mineral samples. *Journal of Unconventional Oil and Gas Resources* **8**, 14-24.

Holditch, S.A. 2003. The increasing role of unconventional reservoirs in the future of the oil and gas business. *Journal of Petroleum Technology* **55**, 34-79.

Holmes, R., Rupp, E.C., Vishal, V. & Wilcox, J. 2017. Selection of shale preparation protocol and outgas procedures for applications in low-pressure analysis. *Energy & Fuels*.

Hook, J.R. 2003. An introduction to porosity. *Petrophysics* **44**.

Hossain, Z., Grattoni, C.A., Solymar, M. & Fabricius, I.L. 2011. Petrophysical properties of greensand as predicted from NMR measurements. *Petroleum Geoscience* **17**, 111-125.

Hower, J., Eslinger, E.V., Hower, M.E. & Perry, E.A. 1976. Mechanism of burial metamorphism of argillaceous sediment: 1. Mineralogical and chemical evidence. *Geological Society of America Bulletin* **87**, 725-737.

Hunt, C.P., Moskowitz, B.M. & Banerjee, S.K. 1995. Magnetic properties of rocks and minerals. *Rock physics & phase relations* **3**, 189-204.

Hurlimann, M., Helmer, K.G., Latour, L. & Sotak, C.H. 1994. Restricted diffusion in sedimentary rocks. Determination of surface-area-to-volume ratio and surface relaxivity. *Journal of Magnetic Resonance, Series A* **111**, 169-178.

Jaroniec, M. 1995. Evaluation of the fractal dimension from a single adsorption isotherm. *Langmuir* **11**, 2316-2317.

Jarvie, D.M., Hill, R.J., Ruble, T.E. & Pollastro, R.M. 2007. Unconventional shale-gas systems: The Mississippian Barnett Shale of north-central Texas as one model for thermogenic shale-gas assessment. *Aapg Bulletin* **91**, 475-499.

Javadpour, F. 2009. Nanopores and apparent permeability of gas flow in mudrocks (shales and siltstone). *Journal of Canadian Petroleum Technology* **48**, 16-21.

Ji, L., Zhang, T., Milliken, K.L., Qu, J. & Zhang, X. 2012. Experimental investigation of main controls to methane adsorption in clay-rich rocks. *Applied Geochemistry* **27**, 2533-2545.

Jia, B., Tsau, J.-S. & Barati, R. 2018. Different flow behaviors of low-pressure and high-pressure carbon dioxide in shales. *SPE Journal* **23**, 1,452-1,468.

Josh, M., Esteban, L., Piane, C.D., Sarout, J., Dewhurst, D.N. & Clennell, M.B. 2012. Laboratory characterisation of shale properties. *Journal of Petroleum Science & Engineering* **s 88–89**, 107–124.

Katsube, T., Scromeda, N. & Williamson, M. 1992. Effective porosity of tight shales from the venture gas field, offshore Nova Scotia. *Geological Survey of Canada, Paper*, 111-119.

Katz, A. & Thompson, A. 1985. Fractal sandstone pores: implications for conductivity and pore formation. *Physical Review Letters* **54**, 1325.

Katz, D.L.V. 1959. *Handbook of natural gas engineering.* McGraw-Hill.

Keating, K. & Knight, R. 2006. A laboratory study to determine the effect of iron oxides on proton NMR measurements. *Geophysics* **72**, E27-E32.

Keating, K. & Knight, R. 2010. A laboratory study of the effect of Fe (II)-bearing minerals on nuclear magnetic resonance (NMR) relaxation measurements. *Geophysics* **75**, F71-F82.

Keating, K. & Knight, R. 2012. The effect of spatial variation in surface relaxivity on nuclear magnetic resonance relaxation ratesSpatially variable surface relaxivity. *Geophysics* **77**, E365-E377.

Keller, L.M., Holzer, L., Wepf, R. & Gasser, P. 2011. 3D geometry and topology of pore pathways in Opalinus clay: Implications for mass transport. *Applied Clay Science* **52**, 85-95.

Kenyon, B., Kleinberg, R., Straley, C., Gubelin, G. & Morriss, C. 1995. Nuclear magnetic resonance imaging—technology for the 21st century. *Oilfield Review* **7**, 19-33.

Kenyon, W. 1992. Nuclear magnetic resonance as a petrophysical measurement. *The International journal of radiation applications and instrumentation. Part E. Nuclear geophysics* **6**, 153-171.

Khalili, N.R., Pan, M. & Sandı, G. 2000. Determination of fractal dimensions of solid carbons from gas and liquid phase adsorption isotherms. *Carbon* **38**, 573-588.

King Jr, H.E., Eberle, A.P., Walters, C.C., Kliewer, C.E., Ertas, D. & Huynh, C. 2015. Pore architecture and connectivity in gas shale. *Energy & Fuels* **29**, 1375-1390.

Kleinberg, R. 1996. Utility of NMR T2 distributions, connection with capillary pressure, clay effect, and determination of the surface relaxivity parameter ρ2. *Magnetic resonance imaging* **14**, 761-767.

Knapp, L.J., Nanjo, T., Uchida, S., Haeri-Ardakani, O. & Sanei, H. Year. Investigating Influences on Organic Matter Porosity and Pore Morphology in Duvernay Formation Organic-Rich Mudstones. Conference Investigating Influences on Organic Matter Porosity and Pore Morphology in Duvernay Formation Organic-Rich Mudstones.

Kravchenko, A. & Zhang, R. 1998. Estimating the soil water retention from particle-size distributions: A fractal approach. *Soil science* **163**, 171-179.

Krooss, B.v., Van Bergen, F., Gensterblum, Y., Siemons, N., Pagnier, H. & David, P. 2002. High-pressure methane and carbon dioxide adsorption on dry and moisture-equilibrated Pennsylvanian coals. *International Journal of Coal Geology* **51**, 69-92.

Kuila, U. 2013. Measurement and interpretation of porosity and pore-size distribution in mudrocks: The hole story of shales. Colorado School of Mines. Arthur Lakes Library.

Kuila, U., Mccarty, D.K., Derkowski, A., Fischer, T.B. & Prasad, M. 2014a. Total porosity measurement in gas shales by the water immersion porosimetry (WIP) method. *Fuel* **117**, 1115-1129.

Kuila, U., McCarty, D.K., Derkowski, A., Fischer, T.B., Topór, T. & Prasad, M. 2014b. Nano-scale texture and porosity of organic matter and clay minerals in organic-rich mudrocks. *Fuel* **135**, 359-373.

Kuila, U. & Prasad, M. 2013. Specific surface area and pore-size distribution in clays and shales. *Geophysical Prospecting* **61**, 341-362.

Labani, M.M. 2014. An investigation into the interrelationship between petrophysical properties of potential gas shale reservoirs from Western Australia. Curtin University.

Labani, M.M., Rezaee, R., Saeedi, A. & Hinai, A.A. 2013. Evaluation of pore size spectrum of gas shale reservoirs using low pressure nitrogen adsorption, gas expansion and mercury porosimetry: A case study from the Perth and Canning Basins, Western Australia. *Journal of Petroleum Science & Engineering* **112**, 7-16.

Lafargue, E., Marquis, F. & Pillot, D. 1998. Rock-Eval 6 applications in hydrocarbon exploration, production, and soil contamination studies. *Revue de l'institut français du pétrole* **53**, 421-437.

Langford, F. & Blanc-Valleron, M.-M. 1990. Interpreting Rock-Eval pyrolysis data using graphs of pyrolizable hydrocarbons vs. total organic carbon (1). *Aapg Bulletin* **74**, 799-804.

Lastoskie, C., Gubbins, K.E. & Quirke, N. 1993. Pore size distribution analysis of microporous carbons: a density functional theory approach. *The Journal of physical chemistry* **97**, 4786-4796.

Leu, L., Georgiadis, A., Blunt, M.J., Busch, A., Bertier, P., Schweinar, K., Liebi, M., Menzel, A. & Ott, H. 2016. Multiscale Description of Shale Pore Systems by Scanning SAXS and WAXS Microscopy. *Energy & Fuels* **30**, 10282-10297.

Li, J., Li, X., Wang, X., Li, Y., Wu, K., Shi, J., Yang, L., Feng, D., Zhang, T. & Yu, P. 2016. Water distribution characteristic and effect on methane adsorption capacity in shale clay. *International Journal of Coal Geology* **159**, 135-154.

Liu, B., Wang, H., Fu, X., Bai, Y., Bai, L., Jia, M. & He, B. 2019. Lithofacies and depositional setting of a highly prospective lacustrine shale oil succession from the Upper Cretaceous Qingshankou Formation in the Gulong sag, northern Songliao Basin, northeast China. *Aapg Bulletin* **103**, 405-432.

Liu, K. & Ostadhassan, M. 2017. Multi-scale fractal analysis of pores in shale rocks. *Journal of Applied Geophysics* **140**, 1-10.

Liu, K., Ostadhassan, M., Hackley, P., Gentzis , T., Zou, J., Yuan, Y., Carvajal-Ortiz, H., Rezaee, R. & Bubach, B. Experimental study on the impact of thermal maturity on shale microstructures using hydrous pyrolysis.

Liu, K., Ostadhassan, M. & Kong, L. 2018a. Fractal and multifractal characteristics of pore throats in the Bakken Shale. *Transport in porous media*, 1-20.

Liu, K., Ostadhassan, M., Zhou, J., Gentzis, T. & Rezaee, R. 2017. Nanoscale pore structure characterization of the Bakken shale in the USA. *Fuel* **209**, 567-578.

Liu, K., Ostadhassan, M., Zou, J., Gentzis, T., Rezaee, R., Bubach, B. & Carvajal-Ortiz, H. 2018b. Multifractal analysis of gas adsorption isotherms for pore structure characterization of the Bakken Shale. *Fuel* **219**, 296-311.

Liu, K., Ostadhassan, M., Zou, J., Gentzis, T., Rezaee, R., Bubach, B. & Carvajal-Ortiz, H. 2018c. Nanopore structures of isolated kerogen and bulk shale in Bakken Formation. *Fuel* **226**, 441-453.

Liu, Y., Yao, Y., Liu, D., Zheng, S., Sun, G. & Chang, Y. 2018d. Shale pore size classification: An NMR fluid typing method. *Marine and Petroleum Geology*.

Loucks, R.G., Reed, R.M., Ruppel, S.C. & Hammes, U. 2010. Preliminary classification of matrix pores in mudrocks.

Loucks, R.G., Reed, R.M., Ruppel, S.C. & Hammes, U. 2012. Spectrum of pore types and networks in mudrocks and a descriptive classification for matrix-related mudrock pores. *Aapg Bulletin* **96**, 1071-1098.

Loucks, R.G., Reed, R.M., Ruppel, S.C. & Jarvie, D.M. 2009. Morphology, genesis, and distribution of nanometer-scale pores in siliceous mudstones of the Mississippian Barnett Shale. *Journal of Sedimentary Research* **79**, 848-861.

Loucks, R.G. & Ruppel, S.C. 2007. Mississippian Barnett Shale: Lithofacies and depositional setting of a deep-water shale-gas succession in the Fort Worth Basin, Texas. *Aapg Bulletin* **91**, 579-601.

Lucatorto, T., De Graef, M. & Wong, P.-Z. 1999. *Methods of the Physics of Porous Media.* Academic Press, ISBN 0080524737.

Luffel, D. & Guidry, F. 1992. New core analysis methods for measuring reservoir rock properties of Devonian shale. *Journal of Petroleum Technology* **44**, 1,184-1,190.

Macht, F., Eusterhues, K., Pronk, G.J. & Totsche, K.U. 2011. Specific surface area of clay minerals: comparison between atomic force microscopy measurements and bulk-gas (N_2) and-liquid (EGME) adsorption methods. *Applied Clay Science* **53**, 20-26.

Mahamud, M.M. & Novo, M.F. 2008. The use of fractal analysis in the textural characterization of coals. *Fuel* **87**, 222-231.

Mandelbrot, B.B. 1983. *The fractal geometry of nature.* WH freeman New York.

Mandelbrot, B.B., Passoja, D.E. & Paullay, A.J. 1984. Fractal character of fracture surfaces of metals. *Nature* **308**, 721.

Mastalerz, M., He, L., Melnichenko, Y.B. & Rupp, J.A. 2012. Porosity of coal and shale: Insights from gas adsorption and SANS/USANS techniques. *Energy & Fuels* **26**, 5109-5120.

Mastalerz, M., Schimmelmann, A., Drobniak, A. & Chen, Y. 2013. Porosity of Devonian and Mississippian New Albany Shale across a maturation gradient: Insights from organic petrology, gas adsorption, and mercury intrusion. *Aapg Bulletin* **97**, 1621-1643.

Mastalerz, M., Wei, L., Drobniak, A., Schimmelmann, A. & Schieber, J. 2018. Responses of specific surface area and micro-and mesopore characteristics of shale and coal to heating at elevated hydrostatic and lithostatic pressures. *International Journal of Coal Geology* **197**, 20-30.

McGlade, C., Speirs, J. & Sorrell, S. 2013. Unconventional gas–a review of regional and global resource estimates. *Energy* **55**, 571-584.

Meiboom, S. & Gill, D. 1958. Modified spin‐echo method for measuring nuclear relaxation times. *Review of scientific instruments* **29**, 688-691.

Melnichenko, Y., Radlinski, A., Mastalerz, M., Cheng, G. & Rupp, J. 2009. Characterization of the CO2 fluid adsorption in coal as a function of pressure using neutron scattering techniques (SANS and USANS). *International Journal of Coal Geology* **77**, 69-79.

Milliken, K.L., Rudnicki, M., Awwiller, D.N. & Zhang, T. 2013. Organic matter–hosted pore system, Marcellus formation (Devonian), Pennsylvania. *Aapg Bulletin* **97**, 177-200.

Neimark, A.V., Lin, Y., Ravikovitch, P.I. & Thommes, M. 2009. Quenched solid density functional theory and pore size analysis of micro-mesoporous carbons. *Carbon* **47**, 1617-1628.

Nelson, P.H. 2009. Pore-throat sizes in sandstones, tight sandstones, and shales. *Aapg Bulletin* **93**, 329-340.

Ouyang, Z., Liu, D., Cai, Y. & Yao, Y. 2016. Fractal analysis on heterogeneity of pore–fractures in middle–high rank coals with NMR. *Energy & Fuels* **30**, 5449-5458.

Passey, Q.R., Bohacs, K., Esch, W.L., Klimentidis, R. & Sinha, S. Year. From oil-prone source rock to gas-producing shale reservoir-geologic and petrophysical characterization of unconventional shale gas reservoirs. Conference From oil-prone source rock to gas-producing shale reservoir-geologic and petrophysical characterization of unconventional shale gas reservoirs.

Pfeifer, P. 1984. Fractal dimension as working tool for surface-roughness problems. *Applications of Surface Science* **18**, 146-164.

Prammer, M., Drack, E., Bouton, J. & Gardner, J. 1996. Measurements of clay-bound water and total porosity by magnetic resonance logging. *The Log Analyst* **37**.

Prasad, M., Mba, K.C., Sadler, T. & Batzle, M.L. 2011. Maturity and impedance analysis of organic-rich shales. *Spe Reservoir Evaluation & Engineering* **14**, 533-543.

Radlinski, A., Mastalerz, M., Hinde, A., Hainbuchner, M., Rauch, H., Baron, M., Lin, J., Fan, L. & Thiyagarajan, P. 2004. Application of SAXS and SANS in evaluation of porosity, pore size distribution and surface area of coal. *International Journal of Coal Geology* **59**, 245-271.

Radlinski, A.P. 2006. Small-angle neutron scattering and the microstructure of rocks. *Reviews in Mineralogy and geochemistry* **63**, 363-397.

Rezaee, R. 2015. *Fundamentals of gas shale reservoirs.* John Wiley & Sons, ISBN 1118645790.

Rezaee, R., Saeedi, A. & Clennell, B. 2012. Tight gas sands permeability estimation from mercury injection capillary pressure and nuclear magnetic resonance data. *Journal of Petroleum Science and Engineering* **88**, 92-99.

Rivera, S. 2014. Ultrasonic and low field nuclear magnetic resonance study of lower Monterey formation: San Joaquin Basin. Colorado School of Mines. Arthur Lakes Library.

Rivera, S. & Prasad, M. Year. Effect of Mineralogy on NMR, Sonic, and Resitivity: A Case Study of the Monterey Formation. Conference Effect of Mineralogy on NMR, Sonic, and Resitivity: A Case Study of the Monterey Formation, 68-87.

Ross, D.J. & Bustin, R.M. 2008. Characterizing the shale gas resource potential of Devonian–Mississippian strata in the Western Canada sedimentary basin: Application of an integrated formation evaluation. *Aapg Bulletin* **92**, 87-125.

Ross, D.J. & Bustin, R.M. 2009. The importance of shale composition and pore structure upon gas storage potential of shale gas reservoirs. *Marine and Petroleum Geology* **26**, 916-927.

Rouquerol, J., Avnir, D., Fairbridge, C., Everett, D., Haynes, J., Pernicone, N., Ramsay, J., Sing, K. & Unger, K. 1994. Recommendations for the characterization of porous solids (Technical Report). *Pure and Applied Chemistry* **66**, 1739-1758.

Rylander, E., Singer, P., Jiang, T., Lewis, R., Sinclair, S. & Mclin, R.H. Year. NMR T_2 distributions in the Eagle Ford shale: reflections on pore size. Conference NMR T_2 distributions in the Eagle Ford shale: reflections on pore size.

Sahouli, B., Blacher, S. & Brouers, F. 1997. Applicability of the fractal FHH equation. *Langmuir* **13**, 4391-4394.

Saidian, M. 2015. Effect of rock composition and texture on pore size distributions in shales: Applications in low field nuclear magnetic resonance. Colorado School of Mines. Arthur Lakes Library.

Saidian, M., Godinez, L.J., Rivera, S. & Prasad, M. Year. Porosity and pore size distribution in mudrocks: a comparative study for Haynesville, Niobrara, monterey, and Eastern European Silurian formations. Conference Porosity and pore size distribution in mudrocks: a comparative study for Haynesville, Niobrara, monterey, and Eastern European Silurian formations, 1226-1243.

Saidian, M., Kuila, U., Prasad, M., Barraza, S.R., Godinez, L.J. & Alcantar-Lopez, L. 2016. A Comparison of Measurement Techniques for Porosity and Pore Size Distribution in Shales (Mudrocks): A Case Study of Haynesville, Eastern European Silurian, Niobrara, and Monterey Formations.

Saidian, M., Livo, K. & Prasad, M. 2015. Effect of paramagnetic mineral content and distribution on surface relaxivity in organic-rich Niobrara and Haynesville shales. In: *SEG Technical Program Expanded Abstracts 2015*, pp. 2671-2676. Society of Exploration Geophysicists, ISBN 1949-4645.

Saidian, M. & Prasad, M. 2015. Effect of mineralogy on nuclear magnetic resonance surface relaxivity: A case study of Middle Bakken and Three Forks formations. *Fuel* **161**, 197-206.

Schettler Jr, P. & Parmely, C. Year. Contributions to total storage capacity in Devonian shales. Conference Contributions to total storage capacity in Devonian shales.

Schön, J.H. 2015. *Physical properties of rocks: Fundamentals and principles of petrophysics.* Elsevier, ISBN 0081004230.

Seaton, N. & Walton, J. 1989. A new analysis method for the determination of the pore size distribution of porous carbons from nitrogen adsorption measurements. *Carbon* **27**, 853-861.

Shao, X., Pang, X., Li, H. & Zhang, X. 2017. Fractal analysis of pore network in tight gas sandstones using nmr method: a case study from the Ordos basin, China. *Energy & Fuels* **31**, 10358-10368.

Sigal, R.F. 2013. Mercury capillary pressure measurements on Barnett core. *Spe Reservoir Evaluation & Engineering* **16**, 432-442.

Sigal, R.F. 2015. Pore-size distributions for organic-shale-reservoir rocks from nuclear-magnetic-resonance spectra combined with adsorption measurements. *SPE Journal* **20**, 824-830.

Sing, K.S. 1985. Reporting physisorption data for gas/solid systems with special reference to the determination of surface area and porosity (Recommendations 1984). *Pure and Applied Chemistry* **57**, 603-619.

Sondergeld, C.H., Ambrose, R.J., Rai, C.S. & Moncrieff, J. Year. Micro-structural studies of gas shales. Conference Micro-structural studies of gas shales.

Sondergeld, C.H., Newsham, K.E., Comisky, J.T., Rice, M.C. & Rai, C.S. Year. Petrophysical considerations in evaluating and producing shale gas resources. Conference Petrophysical considerations in evaluating and producing shale gas resources.

Spears, R.W., Dudus, D., Foulds, A., Passey, Q., Esch, W.L. & Sinha, S. Year. Shale gas core analysis: Strategies for normalizing between laboratories and a clear need for standard materials. Conference Shale gas core analysis: Strategies for normalizing between laboratories and a clear need for standard materials.

Stallmach, F., Vogt, C., Kärger, J., Helbig, K. & Jacobs, F. 2002. Fractal geometry of surface areas of sand grains probed by pulsed field gradient NMR. *Physical Review Letters* **88**, 105505.

Stokes, W.L. & Varnes, D.J. 1955. *Glossary of selected geologic terms with special reference to their use in engineering.* Colorado Scientific Society.

Straley, C., Rossini, D., Vinegar, H., Tutunjian, P. & Morriss, C. 1997. Core analysis by low-field NMR. *The Log Analyst* **38**.

Strapoc, D., Mastalerz, M., Schimmelmann, A., Drobniak, A. & Hasenmueller, N.R. 2010. Geochemical constraints on the origin and volume of gas in the New Albany Shale (Devonian–Mississippian), eastern Illinois Basin. *Aapg Bulletin* **94**, 1713-1740.

Sun, M., Yu, B., Hu, Q., Chen, S., Xia, W. & Ye, R. 2016. Nanoscale pore characteristics of the Lower Cambrian Niutitang Formation Shale: a case study from Well Yuke# 1 in the Southeast of Chongqing, China. *International Journal of Coal Geology* **154**, 16-29.

Suuberg, E.M., Deevi, S.C. & Yun, Y. 1995. Elastic behaviour of coals studied by mercury porosimetry. *Fuel* **74**, 1522-1530.

Tan, M., Mao, K., Song, X., Yang, X. & Xu, J. 2015. NMR petrophysical interpretation method of gas shale based on core NMR experiment. *Journal of Petroleum Science and Engineering* **136**, 100-111.

Tang, P., Chew, N.Y., Chan, H.-K. & Raper, J.A. 2003. Limitation of Determination of Surface Fractal Dimension Using N2 Adsorption Isotherms and Modified Frenkel− Halsey− Hill Theory. *Langmuir* **19**, 2632-2638.

Tarling, D. & Hrouda, F. 1993. *Magnetic anisotropy of rocks.* Springer Science & Business Media, ISBN 0412498804.

Tatlıer, M. & Erdem-Şenatalar, A. 1999. Method to evaluate the fractal dimensions of solid adsorbents. *The Journal of Physical Chemistry B* **103**, 4360-4365.

Testamanti, M.N. 2018. Assessment of Fluid Transport Mechanisms in Shale Gas Reservoirs. Curtin University.

Testamanti, M.N. & Rezaee, R. 2017. Determination of NMR T_2 cutoff for clay bound water in shales: A case study of Carynginia Formation, Perth Basin, Western Australia. *Journal of Petroleum Science and Engineering* **149**, 497-503.

Thomas, B. & Barber, C. 2004. A re-evaluation of the hydrocarbon habitat of the northern Perth Basin. *The APPEA Journal* **44**, 59-92.

Thomas, C. 2014. The tectonic framework of the Perth Basin: Current understanding. *Geological Survey of Western Australia, Record* **14**, 36.

Tinni, A., Sondergeld, C. & Rai, C. Year. Investigation of 2 MHz NMR Measurements Sensitivity to Moveable, Bound and Structural Water in Shales. Conference Investigation of 2 MHz NMR Measurements Sensitivity to Moveable, Bound and Structural Water in Shales.

Tissot, B., Durand, B., Espitalie, J. & Combaz, A. 1974. Influence of nature and diagenesis of organic matter in formation of petroleum. *Aapg Bulletin* **58**, 499-506.

Topór, T., Derkowski, A., Kuila, U., Fischer, T.B. & McCarty, D.K. 2016. Dual liquid porosimetry: A porosity measurement technique for oil-and gas-bearing shales. *Fuel* **183**, 537-549.

Triche, N. & Bahar, M. Year. Shale gas volumetrics of unconventional resource plays in the Canning Basin, Western Australia. SPE 167078. Conference Shale gas volumetrics of unconventional resource plays in the Canning Basin, Western Australia. SPE 167078, 11-13.

U.S. Energy Information Administration, E. 2015. Energy information administration. *Department of Energy* **92010**, 1-15.

Vincent, B., Fleury, M., Santerre, Y. & Brigaud, B. 2011. NMR relaxation of neritic carbonates: An integrated petrophysical and petrographical approach. *Journal of Applied Geophysics* **74**, 38-58.

Volokitin, Y., Looyestijn, W., Slijkerman, W. & Hofman, J. Year. A practical approach to obtain 1st drainage capillary pressure curves from NMR core and log data. Conference A practical approach to obtain 1st drainage capillary pressure curves from NMR core and log data, 1-4.

Wang, F. & Guo, S. 2019. Influential factors and model of shale pore evolution: A case study of a continental shale from the Ordos Basin. *Marine and Petroleum Geology* **102**, 271-282.

Wang, G. & Ju, Y. 2015. Organic shale micropore and mesopore structure characterization by ultra-low pressure N 2 physisorption: Experimental procedure and interpretation model. *Journal of Natural Gas Science and Engineering* **27**, 452-465.

Washburn, E.W. 1921. Note on a method of determining the distribution of pore sizes in a porous material. *Proceedings of the National Academy of Sciences* **7**, 115-116.

Xiao, L., Li, J., Mao, Z., Lu, J., Yu, H., Guo, H. & Li, G. 2018. A method to determine nuclear magnetic resonance (NMR) T 2 cutoff based on normal distribution simulation in tight sandstone reservoirs. *Fuel* **225**, 472-482.

Xu, H., Tang, D., Zhao, J. & Li, S. 2015. A precise measurement method for shale porosity with low-field nuclear magnetic resonance: A case study of the Carboniferous–Permian strata in the Linxing area, eastern Ordos Basin, China. *Fuel* **143**, 47-54.

Yang, F., Ning, Z. & Liu, H. 2014. Fractal characteristics of shales from a shale gas reservoir in the Sichuan Basin, China. *Fuel* **115**, 378-384.

Yao, Y. & Liu, D. 2012. Comparison of low-field NMR and mercury intrusion porosimetry in characterizing pore size distributions of coals. *Fuel* **95**, 152-158.

Yao, Y., Liu, D., Che, Y., Tang, D., Tang, S. & Huang, W. 2010. Petrophysical characterization of coals by low-field nuclear magnetic resonance (NMR). *Fuel* **89**, 1371-1380.

Yao, Y., Liu, D., Tang, D., Tang, S. & Huang, W. 2008. Fractal characterization of adsorption-pores of coals from North China: an investigation on CH4 adsorption capacity of coals. *International Journal of Coal Geology* **73**, 27-42.

Yu, B. & Cheng, P. 2002. A fractal permeability model for bi-dispersed porous media. *International Journal of Heat and Mass Transfer* **45**, 2983-2993.

Yu, B. & Li, J. 2001. Some fractal characters of porous media. *Fractals* **9**, 365-372.

Yu, H., Wang, Z., Rezaee, R., Su, Y., Tan, W., Yuan, Y., Zhang, Y., Xiao, L. & Liu, X. Year. Applications of Nuclear Magnetic Resonance (NMR) Logs in Shale Gas Reservoirs for Pore Size Distribution Evaluation. Conference Applications of Nuclear Magnetic Resonance (NMR) Logs in Shale Gas Reservoirs for Pore Size Distribution Evaluation.

Yu, H., Wang, Z., Rezaee, R., Zhang, Y., Han, T., Arif, M. & Johnson, L. 2018. Porosity estimation in kerogen-bearing shale gas reservoirs. *Journal of Natural Gas Science and Engineering*.

Yuan, Y. & Rezaee, R. 2019a. Comparative Porosity and Pore Structure Assessment in Shales: Measurement Techniques, Influencing Factors and Implications for Reservoir Characterization. *Energies* **12**, 2094.

Yuan, Y. & Rezaee, R. 2019b. Fractal analysis of the pore structure for clay bound water and potential gas storage in shales based on NMR and N2 gas adsorption. *Journal of Petroleum Science and Engineering* **177**, 756-765.

Yuan, Y. & Rezaee, R. 2019c. Impact of paramagnetic minerals on NMR-converted pore size distributions in Permian Carynginia shales. *Energy & Fuels* **33**, 2880-2887.

Yuan, Y., Rezaee, R., Al-Khdheeawi, E.A., Hu, S.-Y., Verrall, M., Zou, J. & Liu, K. 2019. Impact of Composition on Pore Structure Properties in Shale: Implications for Micro-/Mesopore Volume and Surface Area Prediction. *Energy & Fuels* **33**, 9619-9628.

Yuan, Y., Rezaee, R., Tongcheng, H., Verrall, M., Si-Yu, H. & Jie, Z. Year. Pore Characterization and Fluid Distribution Assessment of Gas Shale. In Proceedings of the 80th EAGE Conference and Exhibition 2018, Unconventional Resources I (EAGE-SPE), Copenhagen, Denmark, 11 June 2018.

Yuan, Y., Rezaee, R., Verrall, M., Hu, S.-Y., Zou, J. & Testmanti, N. 2018. Pore characterization and clay bound water assessment in shale with a combination of NMR and low-pressure nitrogen gas adsorption. *International Journal of Coal Geology* **194**, 11-21.

Zargari, S., Prasad, M., Mba, K.C. & Mattson, E.D. 2013. Organic maturity, elastic properties, and textural characteristics of self resourcing reservoirs. *Geophysics*.

Zhang, T., Ellis, G.S., Ruppel, S.C., Milliken, K. & Yang, R. 2012. Effect of organic-matter type and thermal maturity on methane adsorption in shale-gas systems. *Organic Geochemistry* **47**, 120-131.

Zhang, Y., Lebedev, M., Al-Yaseri, A., Yu, H., Xu, X. & Iglauer, S. 2018. Characterization of nanoscale rockmechanical properties and microstructures of a Chinese sub-bituminous coal. *Journal of Natural Gas Science and Engineering* **52**, 106-116.

Zhang, Z. & Weller, A. 2014. Fractal dimension of pore-space geometry of an Eocene sandstone formation. *Geophysics* **79**, D377-D387.

Zheng, S., Yao, Y., Liu, D., Cai, Y. & Liu, Y. 2018. Characterizations of full-scale pore size distribution, porosity and permeability of coals: A novel methodology by nuclear magnetic resonance and fractal analysis theory. *International Journal of Coal Geology* **196**, 148-158.

Zhou, L. & Kang, Z. 2016. Fractal characterization of pores in shales using NMR: A case study from the Lower Cambrian Niutitang Formation in the Middle Yangtze Platform, Southwest China. *Journal of Natural Gas Science and Engineering* **35**, 860-872.

Zhou, S., Liu, D., Cai, Y. & Yao, Y. 2016. Fractal characterization of pore–fracture in low-rank coals using a low-field NMR relaxation method. *Fuel* **181**, 218-226.

Zolfaghari, A. & Dehghanpour, H. Year. Pore size distribution from water adsorption isotherm. Conference Pore size distribution from water adsorption isotherm.

Zou, J., Rezaee, R. & Yuan, Y. 2018. Investigation on the adsorption kinetics and diffusion of methane in shale samples. *Journal of Petroleum Science and Engineering* **171**, 951-958.

Zou, J., Rezaee, R., Yuan, Y., Liu, K., Xie, Q. & You, L. 2019. Distribution of adsorbed water in shale: An experimental study on isolated kerogen and bulk shale samples. *Journal of Petroleum Science and Engineering*, 106858.

Appendix A: Attribution of Authorship

Paper "**Pore characterization and clay-bound water assessment in shale with a combination of NMR and low-pressure nitrogen gas adsorption**" International Journal of Coal Geology, 2018, 194: 11-21.

Authors and full affiliations: Yujie Yuan [a,*], Reza Rezaee [a], Michael Verrall [b], Si-Yu Hu [c], Jie Zou [a], Nadia Testmanti [a]

[a] *WASM: Minerals, Energy and Chemical Engineering, Curtin University, Perth, Australia*

[b] *Earth Sciences and Resource Engineering, CSIRO, 26 Dick Perry Avenue, Kensington, WA 6151, Australia*

[c] *Mineral Resources, CSIRO, 26 Dick Perry Avenue, Kensington, WA 6151, Australia*

	Conception and design	Acquisition of data and method	Data conditioning and manipulation	Analysis and statistical method	Interpretation and discussion	Final approval
Dr. Reza Rezaee						✔
I acknowledge that these represent my contribution to the above research output. Signature: [redacted]						
Mr. Michael Verrall		✔				✔
I acknowledge that these represent my contribution to the above research output. Signature: [redacted]						
Dr. Siyu Hu		✔				✔
I acknowledge that these represent my contribution to the above research output. Signature: [redacted]						
Dr. Jie Zou						✔
I acknowledge that these represent my contribution to the above research output. Signature: [redacted]						
Dr. Nadia Testamanti						✔
I acknowledge that these represent my contribution to the above research output. Signature: [redacted]						

Paper "**Fractal analysis of the pore structure for clay bound water and potential gas storage in shales based on NMR and N_2 gas adsorption**" Journal of Petroleum Science and Engineering, 2019, 177: 756-765.

Authors and full affiliations: Yujie Yuan [*], Reza Rezaee
Western Australian School of Mines: Minerals, Energy and Chemical Engineering, Curtin University

	Conception and design	Acquisition of data and method	Data conditioning and manipulation	Analysis and statistical method	Interpretation and discussion	Final approval
Dr. Reza Rezaee						✔

I acknowledge that these represent my contribution to the above research output.

Signature: [redacted]

Paper "**Impact of paramagnetic minerals on NMR-converted pore size distributions in Permian Carynginia shales**" Energy & Fuels, 2019, 33(4): 2880-2887.

Authors and full affiliations: Yujie Yuan[*], Reza Rezaee
Western Australian School of Mines: Minerals, Energy and Chemical Engineering, Curtin University

	Conception and design	Acquisition of data and method	Data conditioning and manipulation	Analysis and statistical method	Interpretation and discussion	Final approval
Dr. Reza Rezaee						✔

I acknowledge that these represent my contribution to the above research output.

Signature: [redacted]

Paper "**Comparative Porosity and Pore Structure Assessment in Shales: Measurement Techniques, Influencing Factors and Implications for Reservoir Characterization**" Energies, 2019, 12(11): 2094.

Authors and full affiliations: Yujie Yuan[*], Reza Rezaee
WASM: Minerals, Energy and Chemical Engineering, Curtin University

	Conception and design	Acquisition of data and method	Data conditioning and manipulation	Analysis and statistical method	Interpretation and discussion	Final approval
Dr. Reza Rezaee						✔

I acknowledge that these represent my contribution to the above research output.

Signature: [redacted]

Paper "**Impact of Composition on Pore Structure Properties in Shale: Implications for Micro-/Mesopore Volume and Surface Area Prediction**" Energy & Fuels, 2019, v. 33, 9619-9628.

Authors and full affiliations: Yujie Yuan [a,*], Reza Rezaee [a], Emad A. Al-Khdheeawi [a,e], Si-Yu Hu [b], Michael Verrall [c], Jie Zou [a], Kouqi Liu [d]

[a] *Western Australian School of Mines: Minerals, Energy and Chemical Engineering, Curtin University*

[b] *CSIRO Mineral Recourses, Kensington, Western Australia, 6151, Australia*

[c] *CSIRO Earth Science and Resource Engineering, Kensington, Western Australia, 6151, Australia*

[d] *Department of Petroleum Engineering, University of North Dakota, Grand Forks, ND 58202, USA*

[e] *Petroleum Technology Department, University of Technology, Baghdad, Iraq*

	Conception and design	Acquisition of data and method	Data conditioning and manipulation	Analysis and statistical method	Interpretation and discussion	Final approval
Dr. Reza Rezaee						✔
I acknowledge that these represent my contribution to the above research output. Signature: [redacted]						
Dr. Emad A. Al-Khdheeawi				✔		✔
I acknowledge that these represent my contribution to the above research output. Signature: [redacted]						
Dr. Si-Yu Hu						✔
I acknowledge that these represent my contribution to the above research output. Signature: [redacted]						
Mr. Michael Verrall						✔
I acknowledge that these represent my contribution to the above research output. Signature: [redacted]						
Dr. Jie Zou		✔				✔
I acknowledge that these represent my contribution to the above research output. Signature: [redacted]						

Dr. Kouqi Liu						✔

I acknowledge that these represent my contribution to the above research output.

Signature: 

Appendix B: Copyright Permission

The following contents are the permission obtained from the copyright owners, i.e., Elsevier and American Chemical Society (ACS) Publishers, to use my own published journal articles reproduced in the thesis (from Chapter 4 to Chapter 7).

Article: "Pore characterization and clay bound water assessment in shale with a combination of NMR and low-pressure nitrogen gas adsorption" in *International Journal of Coal Geology*.

Article: “ Fractal analysis of the pore structure for clay bound water and potential gas storage in shales based on NMR and N2 gas adsorption” in *Journal of Petroleum Science and Engineering*.

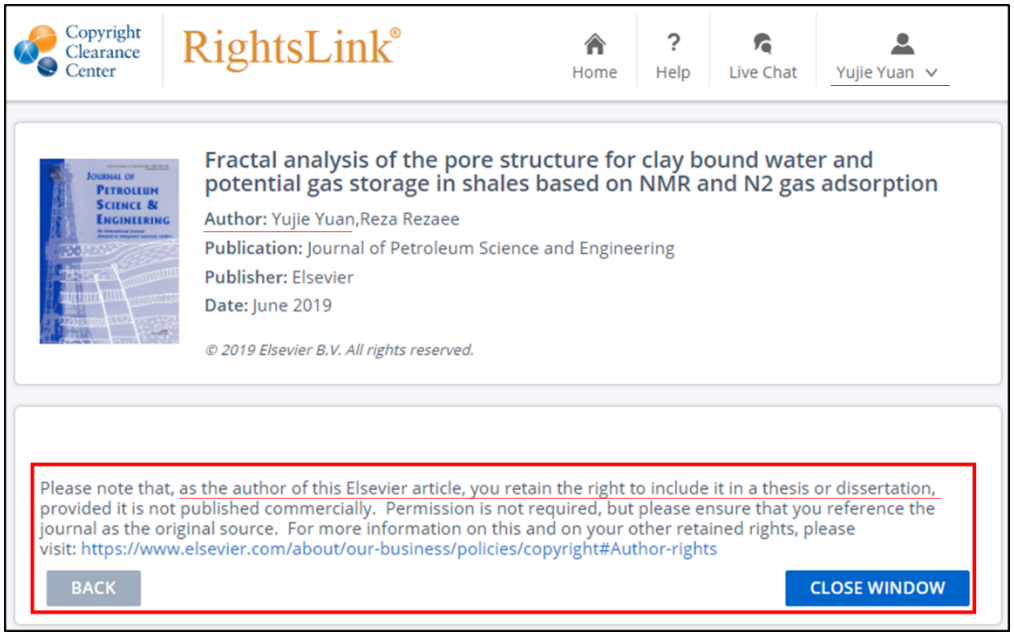

Article: “Impact of Composition on Pore Structure Properties in Shale: Implications for Micro-/Mesopore Volume and Surface Area Prediction” in *Energy & Fuels*.

Article: “Impact of paramagnetic minerals on NMR-converted pore size distributions in Permian Carynginia shales” in *Energy & Fuels.*

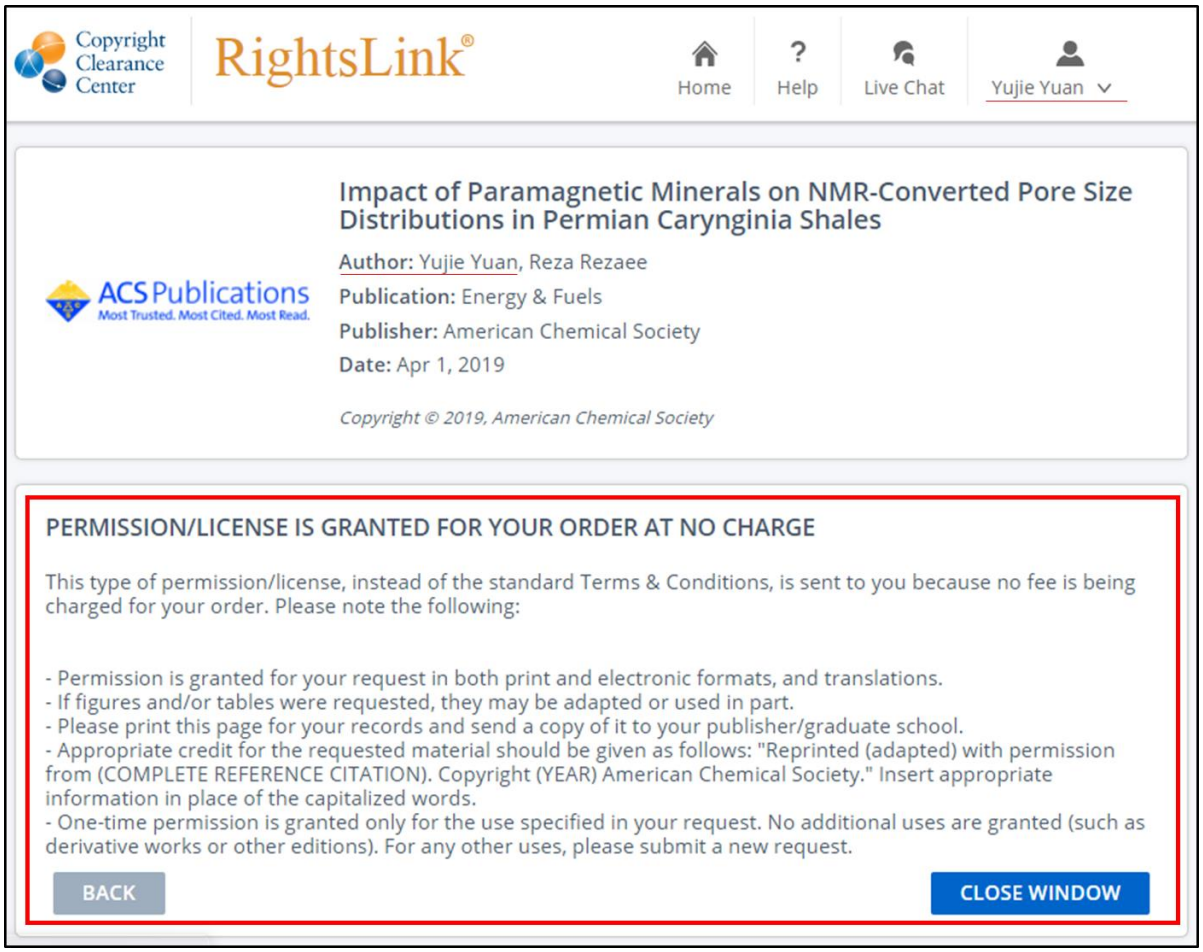

Appendix C: Photos of Goldwyer and Carynginia samples

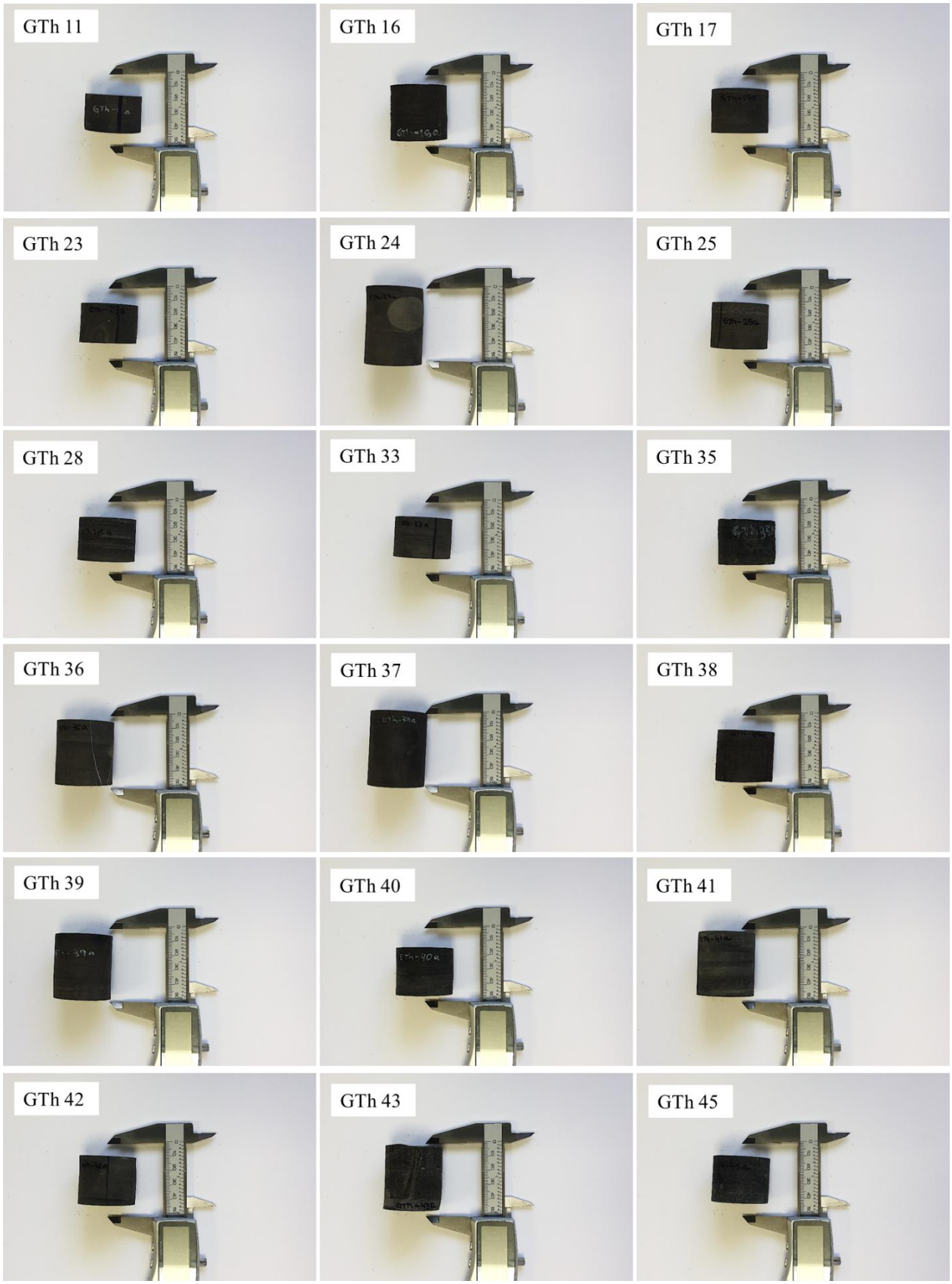

As-received core samples in Ordovician Goldwyer Formation from Canning Basin, WA.

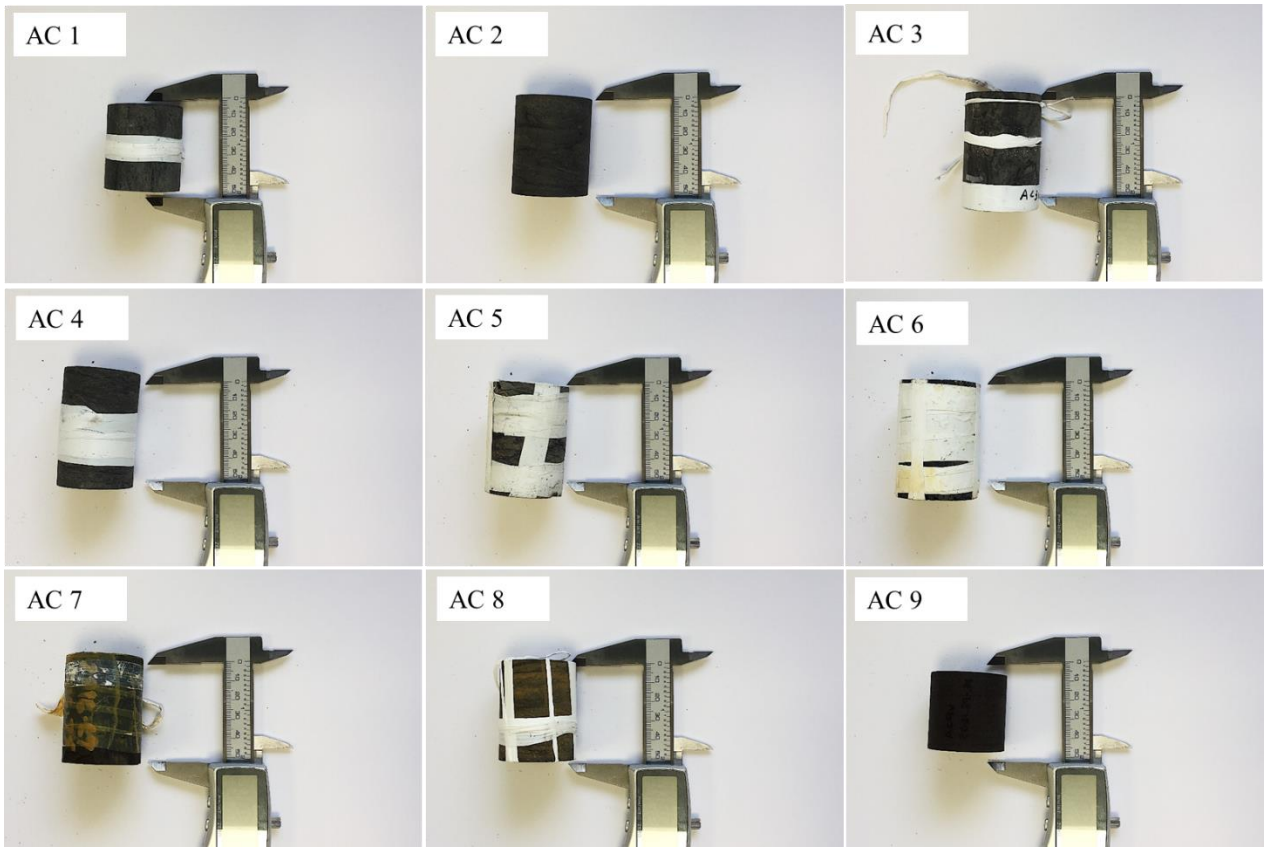

Core samples (after treatment) in Permian Carynginia Formation from Perth Basin, WA.